

ICACT-TACT JOURNAL

Transactions on Advanced Communications Technology



Volume 2 Issue 6, Nov 2013, ISSN: 2288-0003

Editor-in-Chief

Prof. Thomas Byeongnam YOON, PhD.



**Global IT
Research Institute**

Journal Editorial Board

■ Editor-in-Chief

Prof. Thomas Byeongnam YOON, PhD.

Founding Editor-in-Chief

ICTACT Transactions on the Advanced Communications Technology (TACT)

■ Editors

Prof. Jun-Chul Chun, Kyonggi University, Korea

Dr. JongWon Kim, GIST (Gwangju Institute of Science & Technology), Korea

Dr. Xi Chen, State Grid Corporation of China, China

Prof. Arash Dana, Islamic Azad university , Central Tehran Branch, Iran

Dr. Pasquale Pace, University of Calabria - DEIS - Italy, Italy

Dr. Mitch Haspel, Stochastikos Solutions R&D, Israel

Prof. Shintaro Uno, Aichi University of Technology, Japan

Dr. Tony Tsang, Hong Kong Polytechnic University, Hong Kong

Prof. Kwang-Hoon Kim, Kyonggi University, Korea

Prof. Rosilah Hassan, Universiti Kebangsaan Malaysia(UKM), Malaysia

Dr. Sung Moon Shin, ETRI, Korea

Dr. Takahiro Matsumoto, Yamaguchi University, Japan

Dr. Christian Esteve Rothenberg, CPqD - R&D Center for. Telecommunications, Brazil

Prof. Lakshmi Prasad Saikia, Assam down town University, India

Prof. Moo Wan Kim, Tokyo University of Information Sciences, Japan

Prof. Yong-Hee Jeon, Catholic Univ. of Daegu, Korea

Dr. E.A.Mary Anita, Prathyusha Institute of Technology and Management, India

Dr. Chun-Hsin Wang, Chung Hua University, Taiwan

Prof. Wilaiporn Lee, King Mongkut's University of Technology North, Thailand

Dr. Zhi-Qiang Yao, XiangTan University, China

Prof. Bin Shen, Chongqing Univ. of Posts and Telecommunications (CQUPT), China

Prof. Vishal Bharti, Dronacharya College of Engineering, India

Dr. Marsono, Muhammad Nadzir , Universiti Teknologi Malaysia, Malaysia

Mr. Muhammad Yasir Malik, Samsung Electronics, Korea

Prof. Yeonseung Ryu, Myongji University, Korea

Dr. Kyuchang Kang, ETRI, Korea

Prof. Plamena Zlateva, BAS(Bulgarian Academy of Sciences), Bulgaria

Dr. Pasi Ojala, University of Oulu, Finland

Prof. CheonShik Kim, Sejong University, Korea

Dr. Anna bruno, University of Salento, Italy

Prof. Jesuk Ko, Gwangju University, Korea

Dr. Saba Mahmood, Air University Islamabad Pakistan, Pakistan

Prof. Zhiming Cai, Macao University of Science and Technology, Macau

Prof. Man Soo Han, Mokpo National Univ., Korea

Mr. Jose Gutierrez, Aalborg University, Denmark

Dr. Youssef SAID, Tunisie Telecom, Tunisia
Dr. Noor Zaman, King Faisal University, Al Ahsa Hofuf, Saudi Arabia
Dr. Srinivas Mantha, SASTRA University, Thanjavur, India
Dr. Shahriar Mohammadi, KNTU University, Iran
Prof. Beonsku An, Hongik University, Korea
Dr. Guanbo Zheng, University of Houston, USA
Prof. Sangho Choe, The Catholic University of Korea, Korea
Dr. Gyanendra Prasad Joshi, Yeungnam University, Korea
Dr. Tae-Gyu Lee, Korea Institute of Industrial Technology(KITECH), Korea
Prof. Ilkyeun Ra, University of Colorado Denver, USA
Dr. Yong Sun, Beijing University of Posts and Telecommunications, China
Dr. Yulei Wu, Chinese Academy of Sciences, China
Mr. Anup Thapa, Chosun University, Korea
Dr. Vo Nguyen Quoc Bao, Posts and Telecommunications Institute of Technology, Vietnam
Dr. Harish Kumar, Bhagwant Institute of Technology, India
Dr. Jin REN, North China University of Technology, China
Dr. Joseph Kandath, Electronics & Commn Engg, India
Dr. Mohamed M. A. Moustafa, Arab Information Union (AIU), Egypt
Dr. Mostafa Zaman Chowdhury, Kookmin University, Korea
Prof. Francis C.M. Lau, Hong Kong Polytechnic University, Hong Kong
Prof. Ju Bin Song, Kyung Hee University, Korea
Prof. KyungHi Chang, Inha University, Korea
Prof. Sherif Welsen Shaker, Kuang-Chi Institute of Advanced Technology, China
Prof. Seung-Hoon Hwang, Dongguk University, Korea
Prof. Dal-Hwan Yoon, Semyung University, Korea
Prof. Chongyang ZHANG, Shanghai Jiao Tong University, China
Dr. H K Lau, The Open University of Hong Kong, Hong Kong
Prof. Ying-Ren Chien, Department of Electrical Engineering, National Ilan University, Taiwan
Prof. Mai Yi-Ting, Hsiuping University of Science and Technology, Taiwan
Dr. Sang-Hwan Ryu, Korea Railroad Research Institute, Korea
Dr. Yung-Chien Shih, MediaTek Inc., Taiwan
Dr. Kuan Hoong Poo, Multimedia University, Malaysia
Dr. Michael Leung, CEng MIET SMIEEE, Hong Kong
Dr. Abu sahman Bin mohd Supa'at, Universiti Teknologi Malaysia, Malaysia
Prof. Amit Kumar Garg, Deenbandhu Chhotu Ram University of Science & Technology, India
Dr. Jens Myrup Pedersen, Aalborg University, Denmark
Dr. Augustine Ikechi Ukaegbu, KAIST, Korea
Dr. Jamshid Sangirov, KAIST, Korea
Prof. Ahmed Dooguy KORA, Ecole Sup. Multinationale des Telecommunications, Senegal
Dr. Se-Jin Oh, Korea Astronomy & Space Science Institute, Korea
Dr. Rajendra Prasad Mahajan, RGPV Bhopal, India
Dr. Woo-Jin Byun, ETRI, Korea
Dr. Mohammed M. Kadhum, School of Computing, Goodwin Hall, Queen's University, Canada
Prof. Seong Gon Choi, Chungbuk National University, Korea
Prof. Yao-Chung Chang, National Taitung University, Taiwan
Dr. Abdallah Handoura, Engineering school of Gabes - Tunisia, Tunisia
Dr. Gopal Chandra Manna, BSNL, India

Dr. Il Kwon Cho, National Information Society Agency, Korea
Prof. Jiann-Liang Chen, National Taiwan University of Science and Technology, Taiwan
Prof. Ruay-Shiung Chang, National Dong Hwa University, Taiwan
Dr. Vasaka Visoottiviseth, Mahidol University, Thailand
Prof. Dae-Ki Kang, Dongseo University, Korea
Dr. Yong-Sik Choi, Research Institute, IDLE co., Ltd, Korea
Dr. Xuena Peng, Northeastern University, China
Dr. Ming-Shen Jian, National Formosa University, Taiwan
Dr. Soobin Lee, KAIST Institute for IT Convergence, Korea
Prof. Yongpan Liu, Tsinghua University, China
Prof. Chih-Lin HU, National Central University, Taiwan
Prof. Chen-Shie Ho, Oriental Institute of Technology, Taiwan
Dr. Hyoung-Jun Kim, ETRI, Korea
Prof. Bernard Cousin, IRISA/Universite de Rennes 1, France
Prof. Eun-young Lee, Dongduk Woman s University, Korea
Dr. Porkumaran K, NGP institute of technology India, India
Dr. Feng CHENG, Hasso Plattner Institute at University of Potsdam, Germany
Prof. El-Sayed M. El-Alfy, King Fahd University of Petroleum and Minerals, Saudi Arabia
Prof. Lin You, Hangzhou Dianzi Univ, China
Mr. Nicolai Kuntze, Fraunhofer Institute for Secure Information Technology, Germany
Dr. Min-Hong Yun, ETRI, Korea
Dr. Seong Joon Lee, Korea Electrotechnology Research Institute, Korea
Dr. Kwihoon Kim, ETRI, Korea
Dr. Jin Woo HONG, Electronics and Telecommunications Research Inst., Korea
Dr. Heeseok Choi, KISTI(Korea Institute of Science and Technology Information), Korea
Dr. Somkiat Kitjongthawonkul, Australian Catholic University, St Patrick's Campus, Australia
Dr. Dae Won Kim, ETRI, Korea
Dr. Ho-Jin CHOI, KAIST(Univ), Korea
Dr. Su-Cheng HAW, Multimedia University, Faculty of Information Technology, Malaysia
Dr. Myoung-Jin Kim, Soongsil University, Korea
Dr. Gyu Myoung Lee, Institut Mines-Telecom, Telecom SudParis, France
Dr. Dongkyun Kim, KISTI(Korea Institute of Science and Technology Information), Korea
Prof. Yoonhee Kim, Sookmyung Women s University, Korea
Prof. Li-Der Chou, National Central University, Taiwan
Prof. Young Woong Ko, Hallym University, Korea
Prof. Dimiter G. Velev, UNWE(University of National and World Economy), Bulgaria
Dr. Tadasuke Minagawa, Meiji University, Japan
Prof. Jun-Kyun Choi, KAIST (Univ.), Korea
Dr. Brownson ObaridoaObele, Hyundai Mobis Multimedia R&D Lab , Korea
Prof. Anisha Lal, VIT university, India
Dr. kyeong kang, University of technology sydney, faculty of engineering and IT , Australia
Prof. Chwen-Yea Lin, Tatung Institute of Commerce and Technology, Taiwan
Dr. Ting Peng, Chang'an University, China
Prof. ChaeSoo Kim, Donga University in Korea, Korea
Prof. kirankumar M. joshi, m.s.uni.of baroda, India
Dr. Chin-Feng Lin, National Taiwan Ocean University, Taiwan
Dr. Chang-shin Chung, TTA(Telecommunications Technology Association), Korea

Dr. Che-Sheng Chiu, Chunghwa Telecom Laboratories, Taiwan
Dr. Chirawat Kotchasarn, RMUTT, Thailand
Dr. Fateme Khalili, K.N.Toosi. University of Technology, Iran
Dr. Izzeldin Ibrahim Mohamed Abdelaziz, Universiti Teknologi Malaysia , Malaysia
Dr. Kamrul Hasan Talukder, Khulna University, Bangladesh
Prof. HwaSung Kim, Kwangwoon University, Korea
Prof. Jongsub Moon, CIST, Korea University, Korea
Prof. Juinn-Horng Deng, Yuan Ze University, Taiwan
Dr. Yen-Wen Lin, National Taichung University, Taiwan
Prof. Junhui Zhao, Beijing Jiaotong University, China
Dr. JaeGwan Kim, SamsungThales co, Korea
Prof. Davar PISHVA, Ph.D., Asia Pacific University, Japan
Ms. Hela Mliki, National School of Engineers of Sfax, Tunisia
Prof. Amirmansour Nabavinejad, Ph.D., Sepahan Institute of Higher Education, Iran

Editor Guide

■ Introduction for Editor or Reviewer

All the editor group members are to be assigned as a evaluator(editor or reviewer) to submitted journal papers at the discretion of the Editor-in-Chief. It will be informed by eMail with a Member Login ID and Password.

Once logged the Website via the Member Login menu in left as a evaluator, you can find out the paper assigned to you. You can evaluate it there. All the results of the evaluation are supposed to be shown in the Author Homepage in the real time manner. You can also enter the Author Homepage assigned to you by the Paper ID and the author's eMail address shown in your Evaluation Webpage. In the Author Homepage, you can communicate each other efficiently under the peer review policy. Please don't miss it!

All the editor group members are supposed to be candidates of a part of the editorial board, depending on their contribution which comes from history of ICACT TACT as an active evaluator. Because the main contribution comes from sincere paper reviewing role.

■ Role of the Editor

The editor's primary responsibilities are to conduct the peer review process, and check the final camera-ready manuscripts for any technical, grammatical or typographical errors.

As a member of the editorial board of the publication, the editor is responsible for ensuring that the publication maintains the highest quality while adhering to the publication policies and procedures of the ICACT TACT(Transactions on the Advanced Communications Technology).

For each paper that the editor-in-chief gets assigned, the Secretariat of ICACT Journal will send the editor an eMail requesting the review process of the paper.

The editor is responsible to make a decision on an "accept", "reject", or "revision" to the Editor-in-Chief via the Evaluation Webpage that can be shown in the Author Homepage also.

■ Deadlines for Regular Review

Editor-in-Chief will assign a evaluation group(a Editor and 2 reviewers) in a week upon receiving a completed Journal paper submission. Evaluators are given 2 weeks to review the paper. Editors are given a week to submit a recommendation to the Editor-in-Chief via the evaluation Webpage, once all or enough of the reviews have come in. In revision case, authors have a maximum of a month to submit their revised manuscripts. The deadlines for the regular review process are as follows:

Evaluation Procedure	Deadline
Selection of Evaluation Group	1 week
Review processing	2 weeks
Editor's recommendation	1 week
Final Decision Noticing	1 week

■ Making Decisions on Manuscript

Editor will make a decision on the disposition of the manuscript, based on remarks of the reviewers. The editor's recommendation must be well justified and explained in detail. In cases where the revision is requested, these should be clearly indicated and explained. The editor must then promptly convey this decision to the author. The author may contact the editor if instructions regarding amendments to the manuscript are unclear. All these actions could be done via the evaluation system in this Website. The guidelines of decisions for publication are as follows:

Decision	Description
Accept	An accept decision means that an editor is accepting the paper with no further modifications. The paper will not be seen again by the editor or by the reviewers.
Reject	The manuscript is not suitable for the ICACT TACT publication.
Revision	The paper is conditionally accepted with some requirements. A revision means that the paper should go back to the original reviewers for a second round of reviews. We strongly discourage editors from making a decision based on their own review of the manuscript if a revision had been previously required.

■ Role of the Reviewer

Reviewer Webpage:

Once logged in the Member Login menu in left, you can find out papers assigned to you. You can also login the Author Homepage assigned to you with the paper ID and author's eMail address. In there you can communicate each other via a Communication Channel Box.

Quick Review Required:

You are given 2 weeks for the first round of review and 1 week for the second round of review. You must agree that time is so important for the rapidly changing IT technologies and applications trend. Please respect the deadline. Authors undoubtedly appreciate your quick review.

Anonymity:

Do not identify yourself or your organization within the review text.

Review:

Reviewer will perform the paper review based on the main criteria provided below. Please provide detailed public comments for each criterion, also available to the author.

- How this manuscript advances this field of research and/or contributes something new to the literature?
- Relevance of this manuscript to the readers of TACT?
- Is the manuscript technically sound?
- Is the paper clearly written and well organized?
- Are all figures and tables appropriately provided and are their resolution good quality?
- Does the introduction state the objectives of the manuscript encouraging the reader to read on?
- Are the references relevant and complete?

Supply missing references:

Please supply any information that you think will be useful to the author in revision for enhancing quality of the paper or for convincing him/her of the mistakes.

Review Comments:

If you find any already known results related to the manuscript, please give references to earlier papers which contain these or similar results. If the reasoning is incorrect or ambiguous, please indicate specifically where and why. If you would like to suggest that the paper be rewritten, give specific suggestions regarding which parts of the paper should be deleted, added or modified, and please indicate how.

Journal Procedure

Dear Author,

➤ **You can see all your paper information & progress.**

➤ **Step 1. Journal Full Paper Submission**

Using the Submit button, submit your journal paper through ICACT Website, then you will get new paper ID of your journal, and send your journal Paper ID to the Secretariat@icact.org for the review and editorial processing. Once you got your Journal paper ID, never submit again! Journal Paper/CRF Template

➤ **Step 2. Full Paper Review**

Using the evaluation system in the ICACT Website, the editor, reviewer and author can communicate each other for the good quality publication. It may take about 1 month.

➤ **Step 3. Acceptance Notification**

It officially informs acceptance, revision, or reject of submitted full paper after the full paper review process.

Status	Action
Acceptance	Go to next Step.
Revision	Re-submit Full Paper within 1 month after Revision Notification.
Reject	Drop everything.

➤ **Step 4. Payment Registration**

So far it's free of charge in case of the journal promotion paper from the registered ICACT conference paper! But you have to regist it, because you need your Journal Paper Registration ID for submission of the final CRF manuscripts in the next step's process. Once you get your Registration ID, send it to Secretariat@icact.org for further process.

➤ **Step 5. Camera Ready Form (CRF) Manuscripts Submission**

After you have received the confirmation notice from secretariat of ICACT, and then you are allowed to submit the final CRF manuscripts in PDF file form, the full paper and the Copyright Transfer Agreement. Journal Paper Template, Copyright Form Template, BioAbstract Template,

Journal Submission Guide

All the Out-Standing ICACT conference papers have been invited to this "ICACT Transactions on the Advanced Communications Technology" Journal, and also welcome all the authors whose conference paper has been accepted by the ICACT Technical Program Committee, if you could extend new contents at least 30% more than pure content of your conference paper. Journal paper must be followed to ensure full compliance with the IEEE Journal Template Form attached on this page.

➤ How to submit your Journal paper and check the progress?

Step 1. Submit	Using the Submit button, submit your journal paper through ICACT Website, then you will get new paper ID of your journal, and send your journal Paper ID to the Secretariat@icact.org for the review and editorial processing. Once you got your Journal paper ID, never submit again! Using the Update button, you can change any information of journal paper related or upload new full journal paper.
Step 2. Confirm	Secretariat is supposed to confirm all the necessary conditions of your journal paper to make it ready to review. In case of promotion from the conference paper to Journal paper, send us all the .DOC(or Latex) files of your ICACT conference paper and journal paper to evaluate the difference of the pure contents in between at least 30% more to avoid the self replication violation under scrutiny. The pure content does not include any reference list, acknowledgement, Appendix and author biography information.
Step 3. Review	Upon completing the confirmation, it gets started the review process thru the Editor & Reviewer Guideline. Whenever you visit the Author Homepage, you can check the progress status of your paper there from start to end like this, " Confirm OK! -> Gets started the review process -> ...", in the Review Status column. Please don't miss it!

Volume 2, Issue 6

- 1 Gain and Bandwidth Improvements for Distributed Raman Amplifier in UW-WDM Communication Systems 329

Fathy M. Mustafa *, Ashraf A. M. Khalaf **, F. A. Elgeldawy **
**Bani-suef University, Egypt, ** ElMinia University, Egypt*
- 2 Optimum Stealthy Aircraft Detection Using a Multistatic Radar 337

Hassan El-Kamchouchy, Khaled Saada, Alaa El-Din Sayed Hafez
Alexandria University, Alexandria, Egypt
- 3 Dynamic Physical Impairment-Aware Routing and Wavelength Assignment in 10/40/100 Gbps Mixed Line Rate Optical Networks 343

Filippos BALASIS, Xin WANG, Sugang XU, and Yoshiaki TANAKA
Waseda University, Japan
- 4 Intelligent Packaging and Intelligent Medicine Box for Medication Management towards the Internet-of-Things 352

Zhibo Pang*, Junzhe Tian**, Qiang Chen**
**ABB AB, Västerås, Sweden, ** Royal Institute of Technology (KTH), Stockholm, Sweden*
- 5 Introducing Dual Regularization Parameters into Regularized Channel Inversion (RCI)-Based Vector Perturbation for Modulo Loss Reduction 361

Yafei Hou, Satoshi Tsukamoto, Kazuto Yano, Masahiro Uno, Kiyoshi Kobayashi
ATR Wave Engineering Laboratories, Kyoto, Japan

Gain and Bandwidth Improvements for Distributed Raman Amplifier in UW-WDM Communication Systems

Fathy M. Mustafa *, Ashraf A. M. Khalaf **, F. A. Elgeldawy **

* *Electronics and Communications Engineering Department, Bani-suef University, Egypt*

** *Electronics and Communications Engineering Department, ElMinia University, Egypt*

fmmg80@yahoo.com, ashkhalaf@yahoo.com, f.elgeldawi@yahoo.com

Abstract—Fiber Raman amplifiers in ultra wideband wavelength division multiplexing (UW-WDM) systems have recently received much more attention because of their greatly extended bandwidth and distributed amplification with the installed fiber as gain medium. It has been shown that the bandwidth of the amplifier can be further increased and gain spectrum can be tailored by using pumping with multiple wavelengths. In this paper, the distributed multi-pumping Raman amplifier has been studied and analyzed by testing two designed model of amplifier to obtain the gain of maximum flatness and bandwidth. Also we have investigated the effects of many parameters on the gain and bandwidth of Raman amplifier such as: pumping wavelength, offset wavelength, the relative refractive index difference and the number and location of the cascaded units used in the amplifier model design. The models is analyzed where six and eight Raman pumping of special pumping power and pumping wavelengths are lunched in the forward direction where each model is analyzed by two different way. The gain is computed over the spectral optical wavelengths ($1.45\mu\text{m} \leq \lambda \text{ signal} \leq 1.65\mu\text{m}$). The differential gain of each unit of the amplifier is obtained according to the straight line-exponential model of a small maximum constant gain of 7.4×10^{-14} m/W over an optical wavelength interval of 16 nm

Keyword—Distributed Raman amplifier, Raman gain, Raman Bandwidth, Ultra wideband-wavelength division multiplexing (UW-WDM).

I. INTRODUCTION

OPTICAL amplifiers have played a critical role in the telecommunication revolution that has begun two decades ago. Raman amplification has enabled a dramatic increase in the distance and capacity of light wave systems [1]-[3].

Manuscript received January 5, 2013. This work is sponsored by the Dept. of Electric Eng., Minia University, it is a part of Ph.D study of the 1st author under supervision of the 2nd and 3rd authors.

F. M. Mustafa is a research assistant in electronics and communications department at Bani-suef university, Egypt. He joined the PhD program in Minia university in 2011 (fmmg80@yahoo.com).

A. A.M. Khalaf is with the electronics and communications engineering department, ElMinia university, Egypt. He was a Ph.D student in Graduate School of Natural Science and Technology, Kanazawa university, Japan from 1996 to 2000. He is a corresponding author of this paper (Phone: +20 86 2355261, Fax: +20 86 2346674, ashkhalaf@yahoo.com)

F. A. El-Geldawy is a professor with electrical engineering department, faculty of engineering, ElMinia, Egypt (e-mail: f.elgeldawi@yahoo.com).

There are mainly three reasons for the interest in Raman amplifier. First its capability to provide distributed amplification second is the possibility to provide gain at any wavelength by selecting appropriate pump wavelengths, and the third is the fact that the amplification bandwidth may be broadened simply by adding more pump wavelengths. An important feature of the Raman amplification process is that amplification is achievable at any wavelength by choosing the pump wavelength in accordance with the signal wavelength [4].

The term distributed amplification refers to the method of cancellation of the intrinsic fiber loss. The loss in distributed amplifiers is counter balanced at every point along the transmission fiber in an ideal distributed amplifier [4].

In the mid-nineties, high-power pump lasers became available and in the years following, several system experiments demonstrated the benefits of distributed Raman amplification including repeater-less undersea experiments, high-capacity terrestrial as well as submarine systems transmission experiments, shorter span single-channel systems including 320 Gbit/s pseudo linear transmissions, and in soliton systems [4].

distributed Raman amplifiers improved noise performance because of amplification at any wavelength controlled simply by selecting the appropriate pump wavelength, extended bandwidth achieved by using multiple pumps when compared to amplification using erbium-doped fiber amplifiers (EDFAs), and finally control of the spectral shape of the gain and the noise figure, which may be adjusted by combining and controlling the wavelength and power among multiple pumps [4], [6].

Raman amplifiers pumped at multiple wavelengths draw significant attention in high-speed long-haul WDM transmission, for example, because of their wideband flat-gain profile (100nm with 12 channel-WDM pumping) and superior signal-to-noise ratio (SNR) performance. However, they require numbers of high power pump lasers to achieve high-gain and high bandwidth which makes it very expensive at the initial deployment stage where the WDM bandwidth is not in full use. While modular band-by-band and high upgrade like EDFA-based WDM systems reduces system introduction cost very much, in which either C or L-band EDFAs can be added later when a new bandwidth becomes needed. However, such modular addition of amplifiers is not possible for a DRA in which a transmission fiber is shared as common-gain medium. Neglecting

nonlinear pump interaction or saturation WDM-pumped Raman amplifier gain can be approximated as the linear superposition of Raman gains induced by each pump laser [7].

Currently, RFAs are the only silica-fiber based technology that can extend the amplification bandwidth to the S band while providing performance and reliability comparable with those of EDFAs. However, the noise figure remains high compared to that of the C and L bands [8]. In this paper, the distributed multi-pumping Raman amplifier has been studied and analysed by using N cascaded Raman amplifier units, N pumping signals are injected in a parallel processing at different pumping powers and wavelengths. The designed model of amplifier are considered to obtain the gain of maximum flatness and wider bandwidth. Also we have investigated the effects of many parameters on the gain and bandwidth of Raman amplifier such as: pumping wavelength, offset wavelength, the relative refractive index difference and the number and location of the cascaded units used in the amplifier model design. The gain is computed over the spectral optical wavelengths ($1.45\mu\text{m} \leq \lambda \text{ signal} \leq 1.65\mu\text{m}$). The differential gain of each unit of the amplifier is obtained according to the straight line-exponential model of a maximum gain constant of $7.4 \times 10^{-14} \text{ m/W}$ over an optical wavelength interval of 16 nm. Computer simulations are carried out using the Matlab software package.

II. MATHEMATICAL MODEL

Figure 1 shows an N-Raman amplifier in a cascade form of special pumping powers $Pr_1, Pr_2, Pr_3, Pr_4, \dots, Pr_N$ and corresponding pumping wavelengths $\lambda_{r1}, \lambda_{r2}, \lambda_{r3}, \lambda_{r4}, \dots, \lambda_{rN}$.

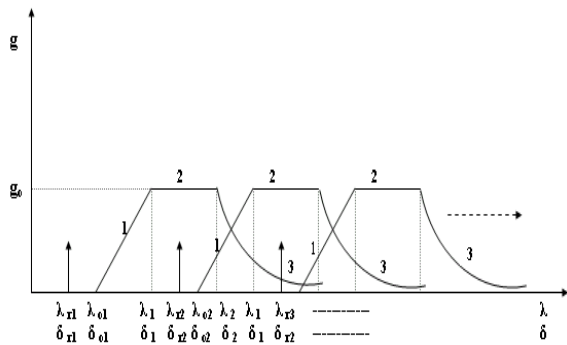


Figure 1. The gain, g , of multi-pump Raman amplifier versus wavelength, λ

The map of δ - g or λ - g is as shown in Figure 1, where δ is the Raman shift and g is the Raman differential gain coefficient; both were cast based on [9-13] as:

$$\delta = \frac{\lambda_s - \lambda_r}{\lambda_s \lambda_r} \times 10^4, \text{ cm}^{-1} \quad (1)$$

The general equations representing the Raman gain in the three regions are $g_{1,i}$, $g_{2,i}$ and $g_{3,i}$ respectively [13]. Where, i denotes the order of amplifier unit in cascade.

$$g_{1,i} = g_o \frac{\delta - \delta_{o,i}}{440} \quad (2)$$

Where, "i" is the number of cascaded units, λ_r is Raman pumping wavelength and $\lambda_o \geq 1.35\mu\text{m}$. The symbol $\delta_{o,i}$ is the Raman shift that indicates the position of each i^{th} amplifier unit.

$$\delta_{o,i} \leq \delta \leq \delta_{1,i}, \quad 0 \leq \delta - \delta_{o,i} \leq 440 \quad (3)$$

With

$$\delta_{o,i} = \frac{\lambda_{o,i} - \lambda_{r,i}}{\lambda_{o,i} \lambda_{r,i}} \times 10^4, \text{ cm}^{-1} \quad (4)$$

With $1 \text{ cm}^{-1} = 30 \text{ GHz}$ [11], where $\lambda_{o,i}$ indicates the offset wavelength and $\lambda_{r,i}$ indicates the pumping wavelength of each amplifier. These wavelengths are then used to indicate $\delta_{o,i}$ for each amplifier.

$$g_{2,i} = g_o, \quad \delta_{1,i} \leq \delta \leq \delta_{2,i} \quad (5)$$

Where, $g_o = 7.4 \times 10^{-14} \text{ m/W}$ is the differential Raman gain constant (of pure SiO₂ at $\lambda = 1.34 \mu\text{m}$), and

$$\delta_{1,i} = \frac{\lambda_{1,i} - \lambda_{r,i}}{\lambda_{1,i} \lambda_{r,i}} \times 10^4, \text{ cm}^{-1} \quad (6)$$

$$\delta_{2,i} = \frac{\lambda_{2,i} - \lambda_{r,i}}{\lambda_{2,i} \lambda_{r,i}} \times 10^4, \text{ cm}^{-1} \quad (7)$$

And

$$g_{3,i} = g_o e^{-0.025(\delta - \delta_{2,i})}, \quad \delta \geq \delta_{2,i} \quad (8)$$

$$\Delta\lambda = \lambda_2 - \lambda_1 = 16 \text{ nm} \quad (\text{fixed value for all units})$$

$$\lambda_1 = \frac{\lambda_{o1}}{1 - 0.044\lambda_{o1}} \times 10^4, \mu\text{m} \quad (9)$$

By changing the position $\delta_{o,i}$, the total bandwidth and the flatness of the amplifier are changed.

We are interested in obtaining a large bandwidth with a wider flat gain by changing $\delta_{o,i}$ or $\lambda_{o,i}$. In this case, we can use either of two cases: $\delta_o = \delta_r$ (i.e. $\lambda_o = \lambda_r$) or $\delta_o > \delta_r$ (i.e. $\lambda_o > \lambda_r$), where λ_r is Raman pump wavelength and λ_o is the offset wavelength.

Raman differential gain constant, g , and the effective core area, A , are defined as [9]:

$$g = 1.34 \times 10^{-6} \times g_o \frac{1 + 80\Delta}{\lambda_r}, \quad \text{and} \quad \Delta = \frac{n_1 - n_2}{n_1} \quad (10)$$

Where Δ is the refractive index difference, n_1 is the refractive index of the core, and n_2 is the refractive index of the clad.

$$A = \frac{\pi}{2} (W_s^2 + W_r^2), \quad (11)$$

And

$$W = \frac{0.21\lambda}{\sqrt{\Delta}} \quad (12)$$

Where, W_s and W_r are the mode field radii of two light waves coupled with each other with $W=W_s$ at $\lambda=\lambda_s$ and $W=W_r$ at $\lambda=\lambda_r$.

Neglecting the cross coupling among the signal channels, one has the differential equation governing the signal propagation for N-channels Raman pumping [9]:

$$\frac{ds_i}{dz} + \sigma_{si}s_i = \left(\sum_{i=1}^{i=N} \sum_{j=1}^{j=M} \frac{g_{ij}}{A_{ij}} P_{Rj} \right) s_i, \quad (13)$$

Where, $i = 1, 2, 3, \dots, N$, M is the number of pumps, S_i is signal power and P_{Rj} is the j^{th} unit pumping power.

Assume the R.H.S of equation (13) equals g_{ti} , as:

$$g_{ti} = \left(\sum_{i=1}^{i=N} \sum_{j=1}^{j=M} \frac{g_{ij}}{A_{ij}} P_{Rj} \right), \quad (14)$$

The total (overall) gain coefficient, g_{ti} in m^{-1} represents the total gain coefficient of the i^{th} signal due to the N-pumping cascaded units. It is clear that g_{ti} is a function of a set of variables such as: signal wavelength; fiber core radius; Raman wavelength; relative refractive index difference; and Raman pumping power. The overall gain, g_{ti} can be written in the form:

$$g_{ti} = \left(\sum_{i=1}^{i=N} \sum_{j=1}^{j=M} g_{di} P_{Rj} \right), \quad (15)$$

Where, the total differential gain, g_{di} , is:

$$g_{di} = \left(\sum_{i=1}^{i=N} \sum_{j=1}^{j=M} g_{ij} \right), mW^{-1} \quad (16)$$

And by Defining a total gain coefficient per watt (m/w), g_{ci} , as:

$$g_{ci} = \left(\sum_{i=1}^{i=N} \sum_{j=1}^{j=M} \frac{g_{dij}}{A_{ij}} \right), m^{-1}W^{-1} \quad (17)$$

Then, we have three gain coefficients: g_{di} , g_{ci} and g_{ti} , are functions of the propagation distance.

III. MODEL EXAMPLES AND CASES

In this paper, we investigated two model examples of cascaded Raman amplifier, these examples are the 6th order and 8th order Raman amplifier, respectively. Both of these examples design are obtained by using the following equation:

$$\lambda_1 = \frac{\lambda_o}{1 - 0.044\lambda_o} \times 10^4, \mu\text{m} \quad (18)$$

TABLE 1.MODEL 1: NUMBER OF AMPLIFIERS = 6

λ_r	λ_o	λ_1	λ_2	Pr(W)
1.4	1.432	1.528294799	1.544294799	0.20
1.42	1.452	1.548294799	1.564294799	0.15
1.44	1.472	1.568294799	1.584294799	0.15
1.467	1.499	1.595294799	1.611294799	0.20
1.48	1.512	1.608294799	1.624294799	0.15
1.5	1.52	1.616294799	1.632294799	0.15

TABLE 2.MODEL 2: NUMBER OF AMPLIFIERS = 8

λ_r	λ_o	λ_1	λ_2	$P_p(W)$
1.4	1.4443	1.540830404	1.556830404	0.14
1.405	1.448	1.545830404	1.561830404	0.12
1.425	1.471	1.568830404	1.584830404	0.14
1.43	1.477	1.574830404	1.590830404	0.10
1.45	1.499	1.596830404	1.612830404	0.14
1.455	1.505	1.602830404	1.618830404	0.12
1.475	1.528	1.625830404	1.641830404	0.11
1.48	1.534	1.631830404	1.647830404	0.13

Firstly, we choose the offset wavelength of the first unit of the cascaded units consisting the overall Raman amplifier; we choose λ_o from the wave length range (from 1.45 μm – to- 1.65 μm). Then, we calculate λ_1 using Eq.(18). After that, we assume the identical Raman units of individual bandwidth of $\lambda_2 - \lambda_1 = 16$ nm. This is done for each amplifier unit.

Finally, we obtain the two design examples, which are the 6th order and 8th order Raman amplifier as shown in TABLE 1 and TABLE 2, respectively. Note that $\lambda_1 - \lambda_o = 0.096294798$, and $\lambda_2 - \lambda_1 = 16$ nm.

We consider two cases for the pumping wavelength λ_r , these two cases are considered for each model example.

A. Case A : $\lambda_r \neq \lambda_o$

B. Case B : $\lambda_r = \lambda_o$

For each case we execute a simulation program to find and demonstrate the figures of the three gain coefficients of the Raman amplifier: g_{di} , g_{ci} and g_{ti} .

There are many parameters affecting the gain coefficients such as: effective core area, relative refractive index difference, pumping wavelengths and pumping powers. So these parameters must be taken into account for any design.

IV. SIMULATION RESULTS AND DISCUSSIONS

The bandwidth for distributed multi-pumping Raman amplifier is investigated with aim of obtaining maximum flat-gain amplifier with as wider bandwidth as possible. Bandwidth; $\Delta\lambda_r$, can be evidently broadened by means of

increasing the number of pumps (amplifier units) and by adjusting the position of these cascaded units.

As we said in Sec. III, we have investigated the distributed multi-pumping Raman amplifier by two model examples that are 6th order and 8th order amplifier. Each model example have been tested under two cases. That are : $\lambda_r \neq \lambda_o$ case and $\lambda_r = \lambda_o$.

A. Results of Model 1:

For The 6th order Raman, the three gain coefficients g_{di} , g_{ci} and g_{ti} , are obtained through simulation results and depicted in the corresponding figures.

A. Model 1: Case A : $\lambda_r \neq \lambda_o$

In this case we put the pumping wavelengths of the amplifier units not equal to the offset wavelengths.

The design structure of the 6th order Raman amplifier is obtained as shown in TABLE 1.

The following results will be demonstrated as:

1) Differential gain:

Figure 2 displays the differential Raman gain versus wavelength, λ , at different values of the relative refractive index difference (Δ). If the relative index difference increases, Raman gain will increase.

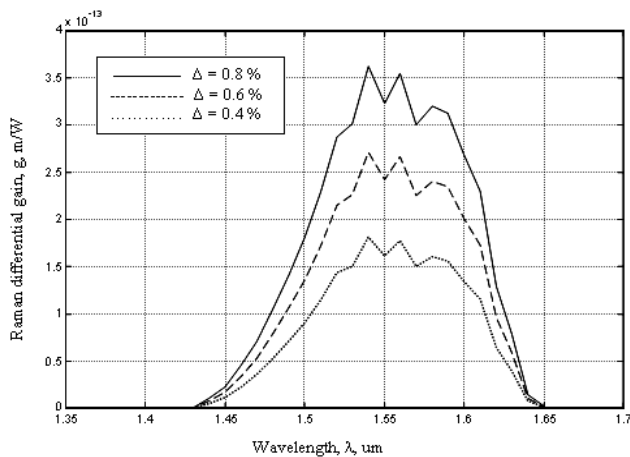


Figure 2. Differential gain versus the wavelength λ at different Δ and $\lambda_r \neq \lambda_o$

We note that Raman gain starts to increase from the first pumping wavelength to reach its peak value at 1.54 μm , then it decreases exponentially tending to zero at 1.65 μm . Since the optical amplifiers and optical signals are operated in the range of 1.45 μm to 1.65 μm . In this case we obtained, the overall bandwidth of the cascaded amplifier =110nm, (from λ_{1t} =1.5 μm to λ_{2t} =1.61 μm).

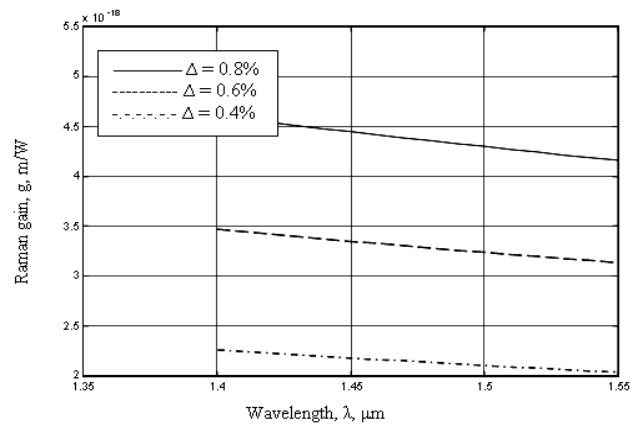


Figure 3. Raman gain variation with different values of Δ

Figure 3 depicts the relation between Raman gain and pumping wavelength. This figure is plotted at different values of relative index difference, where pumping wavelengths for optical signals in the range from 1.4 to 1.55 μm , this range is suitable for Raman amplifier to avoid noise and losses.

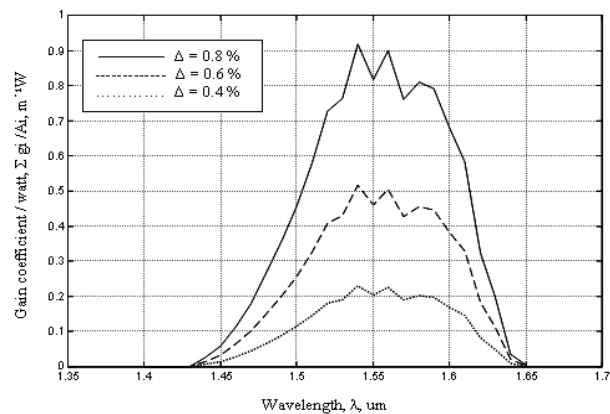


Figure 4. The gain per unit watt at different values of wavelength λ

Figure 4 shows the gain coefficient per unit watt, at different values of relative refractive index difference.

We note that gain coefficient/unit watt starts to increase from the first pumping wavelength to reach its peak value at 1.56 μm , then it decreases exponentially tending to zero at 1.65 μm . In this case we obtained, a total bandwidth (overall bandwidth) =110nm, (from λ_{1t} =1.5 μm to λ_{2t} =1.61 μm).

Depending on these results, we noticed that there are many parameters affecting the gain coefficient per unit watt such as: effective core area, relative refractive index difference, pumping wavelengths and pumping powers. So these parameters must be taken into account for any design.

2) The total gain coefficient:

Figure 5 displays the variation of the total gain coefficient with wavelength. In this case, a bandwidth of 110 nm is obtained. Similarly, we note the peak value of the gain is at 1.54 μm , and the gain tended to zero at 1.65 μm .

It is found that, when pumping powers increase the total gain increases, so Raman amplifier is preferred to be used with high pumping powers.

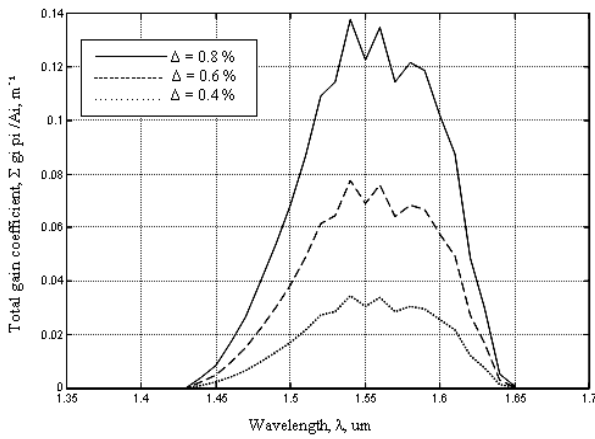


Figure 5. Variation of total gain coefficient with wavelength.

B. Model 1: Case B : $\lambda_r = \lambda_o$

In this case we put the pumping wavelengths equal to the offset wavelengths of the corresponding units. The following results will be demonstrated as:

1) Differential gain:

Figure 6 displays the differential Raman gain, g , with wavelength, λ , at different values of the relative refractive index difference.

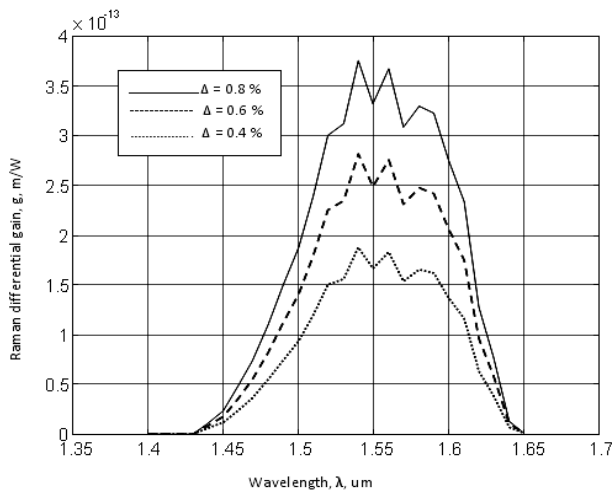


Figure 6. Differential gain versus the wavelength λ at different Δ and $\lambda_r = \lambda_o$

If relative index difference increases, Raman gains increases.

We note that Raman gain starts to increase from the first pumping wavelength to reach to peak value at 1.54 μ m, then the gain decreases exponentially tended to zero at 1.65 μ m. In this case we obtained, an overall bandwidth =120nm, (λ_{1t} =1.49 μ m and λ_{2t} =1.61 μ m).

2) The gain coefficient per unit watt:

The gain coefficient/unit watt, against wavelength is shown in Fig. 7 at different values of relative refractive index difference.

We note that the gain coefficient/unit watt starts to increase from the first pumping wavelength to reach its peak value at 1.56 μ m, then the gain decreases exponentially tended to zero at 1.65 μ m.

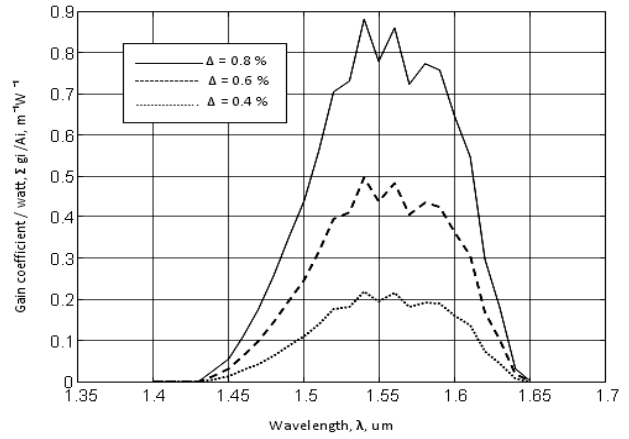


Figure 7. Gain coefficient per unit watt against wavelength.

3) The total gain coefficient:

Figure 8 displays the variation of the total gain coefficient with wavelength. In this case, a bandwidth of 120nm is obtained. Similarly, we note the total gain coefficient has its peak value at 1.54 μ m, and its zero value at 1.65 μ m.

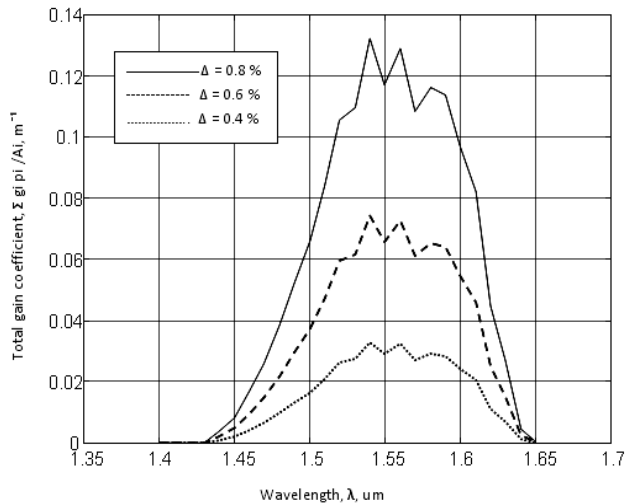


Figure 8. Variation of total gain coefficient with wavelength.

B. Results of Model 2:

For The 8th order Raman, the three gain coefficients : g_{di} , g_{ci} and g_{ti} , are obtained through simulation results and depicted in the corresponding figures.

A. Results of Model 2: Case A : $\lambda_r \neq \lambda_o$

In this case we put the pumping wavelengths of the amplifier units not equal the offset wavelengths. The design structure of the 8th order Raman amplifier is obtained as shown in TABLE 2.

1) Differential gain:

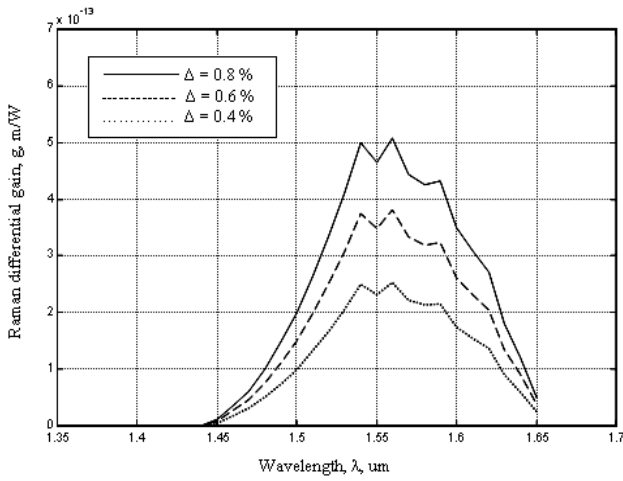


Figure 9. Differential gain versus the wavelength λ at different $\lambda_r \neq \lambda_o$

Figure 9 displays the differential Raman gain, g m/w, with wavelength, λ , at different values of the relative refractive index difference (Δ). If the relative index difference increases, Raman gain will increase. We note that Raman gain starts to increase from the first pumping wavelength to reach to peak value at $1.56\mu\text{m}$, then the gain it starts to decrease exponentially tending to zero at $1.65\mu\text{m}$. Because of optical amplifiers and optical signals are operated in range $1.45\mu\text{m}$ to $1.65\mu\text{m}$. In this case we obtained, total bandwidth = 120nm , where $\lambda_{1t} = 1.5\mu\text{m}$, and $\lambda_{2t} = 1.62\mu\text{m}$.

2) *The gain coefficient per unit watt:*

Figure 10 shows the gain coefficient/unit watt, $\sum g_i / A_i, \text{m}^{-1} \text{W}^{-1}$ at different values of relative refractive index difference.

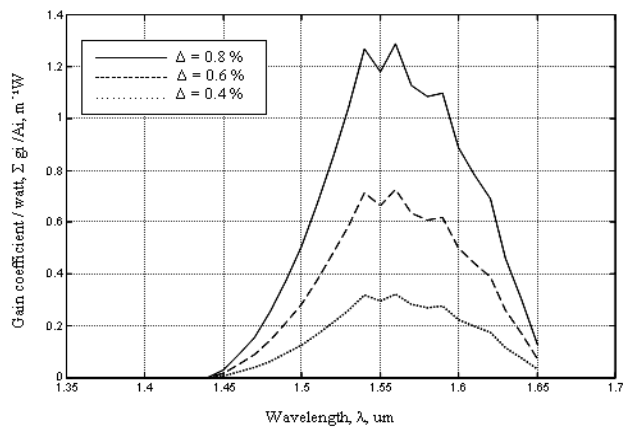


Figure 10. The gain per unit watt at different values of Δ

We note that gain coefficient/unit watt starts to increase from the first pumping wavelength to reach to peak value at $1.56\mu\text{m}$, then the gain decreases exponentially tended to zero at $1.65\mu\text{m}$. Depending on these results, we can say that there are many parameters affect the gain coefficient per unit watt such as: effective core area, relative refractive index difference, pumping wavelengths and pumping powers. So these parameters must be taken into account for any design.

In this case we obtained, total (overall) bandwidth = 120nm , where $\lambda_{1t} = 1.5\mu\text{m}$ and $\lambda_{2t} = 1.62\mu\text{m}$.

3) *The total gain coefficient:*

Figure 11 displays the variation of the total gain coefficient with wavelength. In this case, a bandwidth of 120 nm is obtained. Similarly, we note the total gain coefficient starts to increase from the first pumping wavelength to reach to peak value at $1.56 \mu\text{m}$. The gain decreases exponentially until it reaches to zero at $1.65\mu\text{m}$. Gain in this case is affected by pumping powers, effective core area and the relative index difference.

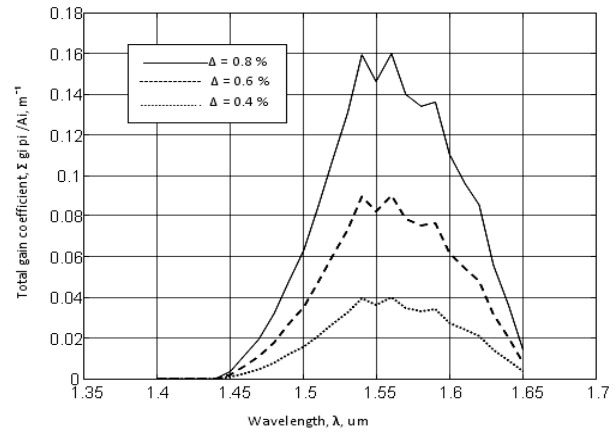


Figure 11. Variation of total gain coefficient with wavelength.

It is found that, when pumping powers increase the total gain increases, so Raman amplifiers is preferred to be used with high pumping powers.

B. *Model 2 :Case B: $\lambda_r = \lambda_o$*

In this case we put the pumping wavelengths equal to the offset wavelengths of the corresponding units.

1) *Differential gain:*

Figure 12 displays the differential Raman gain, g , with wavelength, λ , at different values of the relative refractive index difference. If relative index difference increases, Raman gains increases.

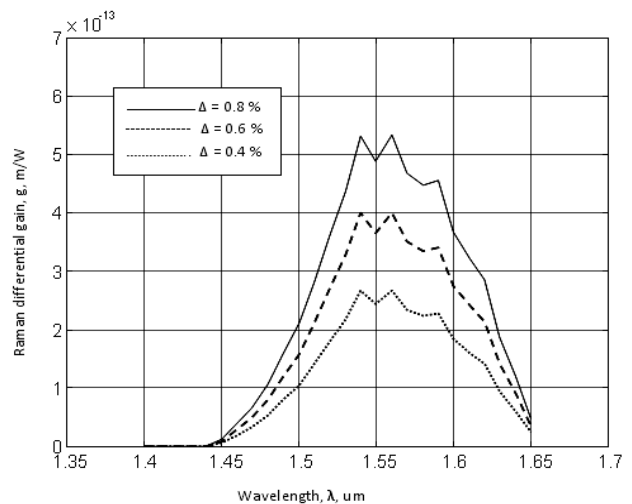


Figure 12. Differential gain versus the wavelength λ at different $\lambda_r = \lambda_o$

We note that Raman gain starts to increase from the first pumping wavelength to reach the peak value at 1.56μm, then it decreases exponentially tended to zero at 1.65μm. Because of optical amplifiers and optical signals are operated in the range 1.45μm to 1.65μm. In this case we obtained, total bandwidth =120nm, where λ_{1t} =1.5μm (for all amplifier units) and λ_{2t} =1.62μm (for all amplifier units).

2) The gain coefficient per unit watt:

The gain coefficient/unit watt, Σ gi / Ai, m⁻¹ W⁻¹ against wavelength is shown in Fig. 13 at different values of relative refractive index difference.

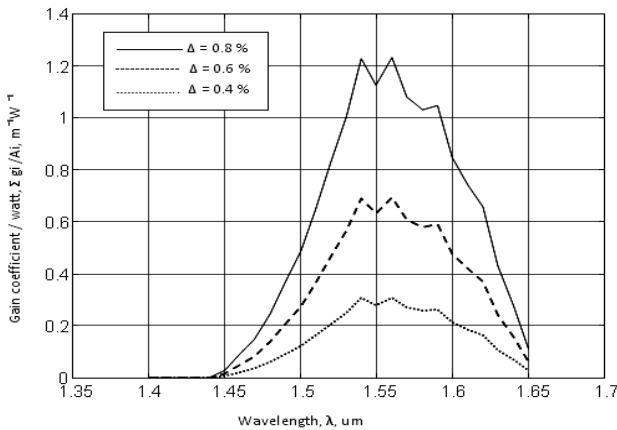


Figure 13. Gain coefficient per unit watt against wavelength.

We note that the peak value at 1.56μm, and the zero value at 1.65μm. Depending on these results, we can say that there are many parameters affect the gain coefficient per unit watt such as: effective core area, relative refractive index difference, pumping wavelengths and pumping powers.

3) The total gain coefficient:

Figure 14 displays the variation of the total gain coefficient with wavelength. In this case, a bandwidth of 120nm is obtained. By similar we note the total gain coefficient is start to increase from the first pumping wavelength to reach to peak value at 1.56μm, the gain is start to decrease exponentially tended to zero at 1.65μm. Gain in this case is affected by pumping powers, effective core area and relative index difference. It is found that, when pumping powers increase the total gain increases, so Raman amplifiers is preferred to be used with high pumping powers.

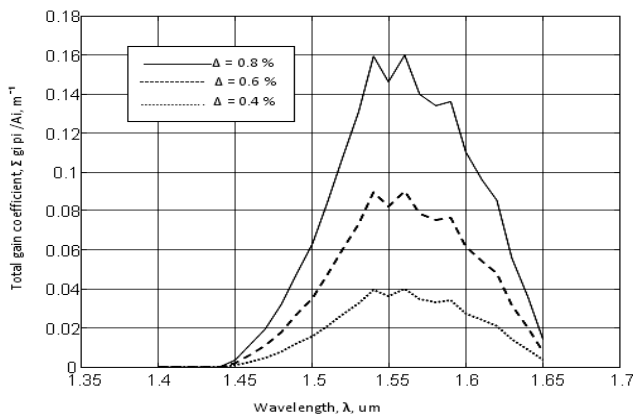


Figure 14. Variation of total gain coefficient with wavelength.

TABLE 3. COMPARISON BETWEEN TWO MODEL

Model 1 number of amplifier N=6			Model 1 number of amplifier N=6		
Case A			Case B		
g_{max}	$\Delta \%$	BW nm	g_{max}	$\Delta \%$	BW nm
3.6239×10^7 ₁₃	0.8	110	3.7553×10^7 ₁₃	0.8	120
2.7179×10^7 ₁₃	0.6		2.8165×10^7 ₁₃	0.6	
1.8119×10^7 ₁₃	0.4		1.8776×10^7 ₁₃	0.4	
Model 2 number of amplifier N=8			Model 2 number of amplifier N=8		
Case A			Case B		
g_{max}	$\Delta \%$	BW nm	g_{max}	$\Delta \%$	BW nm
5.0734×10^7 ₁₃	0.8	120	5.3468×10^7 ₁₃	0.8	120
3.8050×10^7 ₁₃	0.6		4.0101×10^7 ₁₃	0.6	
2.5367×10^7 ₁₃	0.4		2.6734×10^7 ₁₃	0.4	

From TABLE 3, we note that the gain of each unit of the amplifiers in case B is better than the gain in case A also, the bandwidth in case B is larger than in case A for model 1 but for model 2 the bandwidth in case A is the same as in case B but the gain increases in case B. The maximum gain increases with the relative refractive index difference increase. And bandwidth changes according to the change of the position of optical amplifiers. Also from table 3 the gain and bandwidth for model 2 is better than that of model 1, therefore by increasing the cascaded units we can improve the overall performance of the Raman amplifier.

V. CONCLUSIONS

By using N cascaded Raman amplifier units, N pumping signals are injected in a parallel processing at different pumping powers and wavelengths, we have obtained the following simulation results:

- 1- The overall gain of Raman amplifier is increased due to putting the pumping wavelengths equal to the offset wavelengths of the amplifier units.
- 2- We have obtained a bandwidth of about 110 nm and 120 nm at different value of the relative refractive index difference for 6 cascaded units of optical Raman amplifiers.
- 3- And also we have obtained a bandwidth of about 120 nm at different value of the relative refractive index difference for 8 cascaded units of optical Raman amplifiers.
- 4- The overall gain of the cascaded Raman amplifier increases if the number of optical amplifier units and/or the relative refractive index difference increases.
- 5- The bandwidth and/or the flatness of the gain depend on the position of the amplifier units (wavelength value of

the cascaded units) corresponding to each other's and on the number of amplifier units.

References

[1] M. N. Islam, "Raman Amplifiers for Telecommunications," IEEE J. Selected Topics in Quantum Electron., Vol. 8, No. 3, pp.548-559, 2002.

[2] M. D. Mermelstein, K. Brar, and C. Headly, "RIN Transfer Measurement and Modeling in Dual-Order Raman Fiber amplifiers," J. Lightwave Technol., Vol. 21, No. 6, p. 1518, 2003.

[3] J. Bromage, "Raman Amplification for Fiber Communications Systems," J. Lightwave Technol., Vol. 22, No. 1, pp. 79-93, 2004.

[4] C. Headley, G. P. Agrawal "Raman Amplification in Fiber Optical Communication Systems", Elsevier Inc. 2005.

[5] P. Xiao, O. Zeng, J. Huang, and J. Liu, "A New Optimal Algorithm for Multi-Pumping Sources of Distributed Fiber Raman Amplifier," IEEE Photonics Technol. Lett., Vol. 15, No.2, pp. 206-208, 2003.

[6] X. Liu and B. Lee, "A Fast Stable Method for Raman Amplifier Propagation Equation," Optics Express, Vol. 11, No. 18, pp. 2163-2176, 2003.

[7] N. Kikuchi, "Novel In-Service Wavelength-Based Upgrade Scheme for Fiber Raman Amplifier," IEEE Photonics Technol. Lett., Vol. 15, No. 1, pp. 27-29, 2003.

[8] Y. Cao and M. Raja, "Gain-Flattened Ultra-Wideband Fiber Amplifiers," Opt. Eng., Vol. 42, No. 12, pp. 4447-4451, 2003.

[9] M. S. Kao and J. Wu, "Signal Light Amplification by Stimulated Raman Scattering in an N-Channel WDM Optical Communication System", J. Lightwave Technol., Vol.7, No. 9, pp. 1290-1299, 1989.

[10] T. Nakashima, S. Seikai, N. Nakazawa, and Y. Negishi, "Theoretical Limit of Repeater Spacing in Optical Transmission Line Utilizing Raman Amplification," J. Lightwave Technol., Vol. LT-4, No. 8, pp. 1267-1272, 1986.

[11] Y. Aoki, "Properties of Fiber Raman Amplifiers and Their Applicability to Digital Optical Communication Systems," J. Lightwave Technol., Vol. 6 No. 7, pp. 1227-1239, 1988.

[12] W. Jiang and P. Ye., "Crosstalk in Raman Amplification for WDM Systems," J. Lightwave Technol., Vol. 7, No. 9, pp. 1407-1411, 1989.

[13] A. A. Mohammed, "All Broadband Raman Amplifiers for Long-Haul UW-WDM Optical Communication Systems," Bulletin of Faculty of Electronic Engineering, Menouf, 32951, Egypt, 2004.

[14] A. Yariv, Optical Electronics in Modern Communications, 5th ed., Oxford Univ. Press, 1997.

Electronics and communication engineering in 2007 from Arab Academy for Science and Technology & Maritime Transport, College of Engineering and Technology, Alexandria, Egypt. He is joined the PhD program in Mina university in 2011. Her areas of interest include optical communications, optical amplifiers.



Ashraf A.M. Khalaf: received his B.Sc. and M.Sc. degrees in electrical engineering from Minia university, Egypt, in 1989 and 1994 respectively. He received his Ph.D in electrical engineering from Graduate School of Natural Science and Technology, Kanazawa university, Japan in 2000. He works at electronics and communications engineering Department, Minia University. He is a member of IEEE since 12 years.



F. A. El-Geldawy: He is a professor in Electric Engineering Dept., faculty of engineering, Minia, Egypt.



Fathy M. Mustafa: received the B.Sc. degree in Electronics and communications department from the Faculty of Engineering, Fayoum University, Fayoum, Egypt, in 2003. He is currently working a research assistant in Electronics and communications department at Bani-suef University. He is earned the M.Sc degree in

Optimum Stealthy Aircraft Detection Using a Multistatic Radar

Hassan El-Kamchouchy, Khaled Saada, Alaa El-Din Sayed Hafez

Electrical Engineering Department, Faculty of Engineering, Alexandria University, Alexandria, Egypt

El-Kamchouchy@ieee.org, Khaledsaada@yahoo.com, Alaahafez@ieee.org

Abstract— Radar systems, based on Multistatic radar concept attracted a substantial attention in the recent years. The paper proposes system geometry for S-band Multistatic radar. This technique is used for detecting and tracking the small cross section area and stealthy aircrafts. The proposed geometrical structures are studied with different radars spacing to extend the detection coverage over the Monostatic radar used for air surveillance. The radar detection coverage is also studied with all possible stealthy aircraft paths to find the improvement achieved from using this type of radar. The simulation is done using Matlab program. The results show that the first system geometry with two transmitters and four receivers extends the detection coverage 80 Km for small aircraft and 62 Km for stealthy targets. The second system geometry with two transmitters and six receivers extends the detection coverage 85 Km for small targets and 69 Km for stealthy targets. The achieved SNR from these system geometries guarantee a high probability of detection for small and stealthy aircraft detection.

(Pt.9)Keyword— Multistatic radar, Stealthy Aircraft Detection

I. INTRODUCTION

Multistatic radar uses antennas at different locations for transmission and reception. This means that the transmitter and receiver are not co-located in the same place. There are different versions of Multistatic radar system does not specify how far the transmitting and receiving sites must be separated. In recent years, an extended growth of activities in the area of radar systems, based on the concept of the Multistatic radar is reported from many research centers and universities. Marc Brooker [1] presents the design and implementation of a signal level simulator supporting a wide variety of radar systems, focusing on Multistatic and netted radars. The simulator places few limits on the simulated system, and supports systems with arbitrary numbers of receivers, transmitters, and scatterers. Bezousek et. al. [2]

described the Multistatic arrangement system with non-cooperative transmitters and various aspects of signal processing and signal parameters. Benson [3] investigates modeling method to optimize the location of receivers in order to achieve maximum coverage of aircraft moving around Cape Town International Airport. Several researches deal with improving the detection coverage using Multistatic radar systems [4-6]. These researches didn't study the radar coverage with different system geometry and various radar spacing. The paper proposes system geometry for S-band Multistatic radar for detecting and tracking the small cross section area and stealthy aircrafts. The proposed geometrical structures are studied with different radars spacing to extend the detection coverage over the Monostatic radar used for air surveillance. The radar detection coverage is also studied with all possible stealthy aircraft paths to find the improvement achieved from using this type of radar. The first section of the paper introduces theoretical description of the Multistatic radar. The second section presents the simulation results and the findings from this paper. The last section displays the conclusion of the paper.

II. THEORETICAL BACKGROUND

A Multistatic radar system contains multiple spatially diverse Monostatic radar or bistatic radar components with a shared area of coverage. An important distinction system based on these individual radar geometries is the added requirement for some level of data fusion to take place between component parts. The spatial diversity afforded by Multistatic systems allows for different aspects of a target to be viewed simultaneously. The potential for information gain can give rise to a number of advantages over conventional systems. Multistatic radar is often referred to as 'Multisite' or 'netted' radar. Fig. 1. shows the idea of using all available sources of transmission for target localization and co-located receiver module, [7]. An obvious advantage of separating the receiver and the transmitter is that the receiver is passive and difficult to locate and which doesn't make it a target for e.g. Anti Radiation Missiles (ARM). Personnel are safe from ARM when located at the Rx. Separation also has effect on the effectiveness of Electronic Counter Measures (ECM) since the Tx and Rx are not co-located and therefore the Rx may be outside the main-lobe of the jammer or even outside the Line Of Sight (LOS). Since the receiver is not readily discovered it

Manuscript received February 12, 2013. This work was supported in part by the Electrical Engineering Department, Alexandria University, Alexandria, Egypt.

Hassan El-Kamchouchy, Professor of the Communications, Faculty of Engineering, Alexandria University, Alexandria, Egypt.

(Email: El-Kamchouchy@ieee.org; Tel:+20-03-5627902)

Khaled Samir Saada, Ph.D. student, Alexandria University, Alexandria, Egypt.

(Email: Kaledsaada@yahoo.com; Tel:+20-0122-4516005)

Alaa El-Din Sayed Hafez, Affiliate Instructor, Faculty of Engineering, Alexandria University, Alexandria, Egypt.

(Email: Alaahafez@ieee.org; Tel:+20-0100-1525961)

is suitable for covert operations. Several receivers can operate without disclose of their positions with the transmitter stand off by a large distance. Relations of Signal to Noise ratio (S/N) will be discussed. The range equation for a bistatic radar is derived in a manner completely analogous to that for a Monostatic radar. With this analog, the bistatic radar maximum-range equation can be written as [8-9],

$$(R_T R_R)_{\max} = \left(\frac{P_T G_T G_R \lambda^2 \sigma_i F_T^2 F_R^2}{(4\pi)^3 K T_s B_n (S/N)_{\min} L_T L_R} \right)^{\frac{1}{2}} \quad (1)$$

where R_T , R_R are the transmitter and receiver to target range respectively, P_T is the transmitted power, G_T , G_R are the transmit and receive antenna power gain respectively, λ is the transmitted signal wavelength, σ_i is the bistatic radar cross section, F_T , F_R are the transmit and receive propagation factor respectively, K is the Boltzmann constant, T_s is the receive system noise temperature, B_n is the noise bandwidth of the receiver, S/N is the signal to noise ratio and L_T , L_R are the transmit and receive system losses. The Multistatic from the radar equation is developed to evaluate Multistatic radar sensitivity properties. A fully coherent radar network is considered, which means that the radars comprising the whole network have a common and highly precise knowledge of time and space. The whole radar network is composed of m transmitters and n receivers. It is assumed that the whole network is well synchronized and works cooperatively such that each receiver is capable of receiving echoes due to any transmitters in the network. Under these assumptions, it is reasonable to calculate the overall radar sensitivity by summing up the partial signal to noise ratio, which is given by, [10].

$$(S/N)_{\text{netted}} = \sum_{i=1}^m \sum_{j=1}^n \frac{P_{T_i} G_{T_i} G_{R_j} \lambda_i^2 \sigma_{ij} F_{T_i}^2 F_{R_j}^2}{(4\pi)^3 K T_s B_n R_{T_i}^2 R_{R_j}^2 L_{T_i} L_{R_j}} \quad (2)$$

Considering the simplest case where the radar parameters for every transmitter-receiver combination are the same, the Multistatic radar equation can be simplified as,

$$(S/N)_{\text{netted}} = \frac{P_T G_T G_R \lambda^2 \sigma_i F_T^2 F_R^2}{(4\pi)^3 K T_s B_n L_T L_R} \sum_{i=1}^m \sum_{j=1}^n \frac{1}{R_{T_i}^2 R_{R_j}^2} \quad (3)$$

From this equation it is clear to see that the Multistatic radar geometry, i.e. the positions of target and radar in the network, will have great influence on the overall Multistatic radar sensitivity.

III. THE PROPOSED SYSTEM GEOMETRY

The proposed system geometries are demonstrated in Fig. 2. The first system geometry G1 consists of two transmitters and four receivers. The second system geometry G2 consists of two transmitters and six receivers. The spacing between radar

stations is constant for the system geometry. The coordinate system must be converted for each radar station according to the following equations,

$$R_{yref} = R_{ref} \cos(\theta_{ref})$$

$$R_{xref} = R_{ref} \sin(\theta_{ref})$$

$$R_{y2} = R_{yref}$$

$$R_{x2} = R_{xref} - a$$

$$R_{y3} = R_{yref} + 2a$$

$$R_{x3} = R_{xref}$$

$$R_{y4} = R_{yref} + 2a$$

$$R_{x4} = R_{xref} - a$$

$$R_{y5} = R_{yref} + a$$

$$R_{x5} = R_{xref} + a$$

$$R_{y6} = R_{yref} + a$$

$$R_{x6} = R_{xref} - a$$

$$R_{yx1} = R_{yref} + a$$

$$R_{xx1} = R_{xref}$$

$$R_{yx2} = R_{yref} + a$$

$$R_{xx2} = R_{xref} - a$$

IV. SIMULATION RESULTS

The system geometries are simulated under Matlab program environment to obtain the radar sensitivity under the proposed conditions, and demonstrate all possible radar spacing to achieve an optimum radar arrangement satisfying the optimum detection. The radar transmitter parameters are illustrated in table 1. Multistatic radar system geometry G1 and G2 are simulated with radar spacing from 5 Km to 70 Km for aircraft range from 50 Km to 140 Km. It is found that the optimum radar spacing for the system geometry G1 is 48 Km and 50 Km for G2. Fig. 3. shows the received S/N at different radar spacing and target ranges for system geometry G1 with small aircrafts ($\sigma = 0.1 \text{ m}^2$), and stealthy aircrafts ($\sigma = 0.025 \text{ m}^2$). A comparison between Multistatic radar system geometry G1 and Monostatic radar with small cross section is investigated in Fig. 4. Same comparative study is demonstrated in Fig. 5. for stealthy aircrafts. Fig. 6. shows the received S/N at different radar spacing and target ranges for system geometry G2 with small aircrafts ($\sigma = 0.1 \text{ m}^2$), and stealthy aircrafts ($\sigma = 0.025 \text{ m}^2$). Received S/N at different azimuth angles and target ranges for system geometry G2 is demonstrated in Fig. 7. The results are concluded in Fig. 8.

The system geometry G1 extends the detection coverage 80 Km for small aircraft and 62 Km for a stealthy target over the Monostatic radar. The second system geometry G2 improves the detection coverage for the small aircrafts by 85 Km and 69 Km for a stealthy aircrafts.

TABLE I
Radar Transmitter Parameters

Parameter	Value
P_T (Kwatt)	200
G_T, G_R (dB)	33
F (MHz)	2450
B_n (MHz)	1
F_T, F_R	1
L_T, L_R (dB)	5

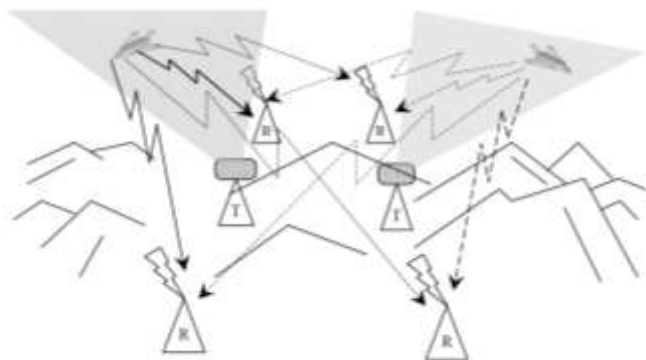
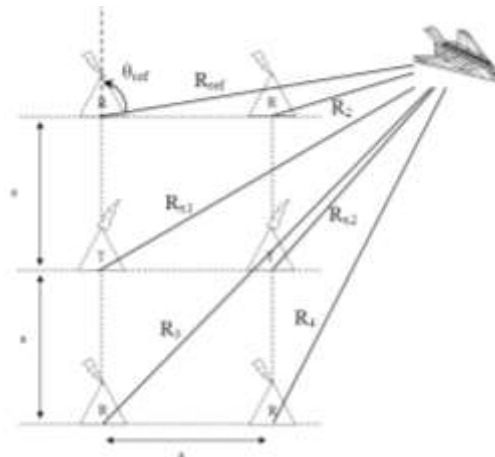


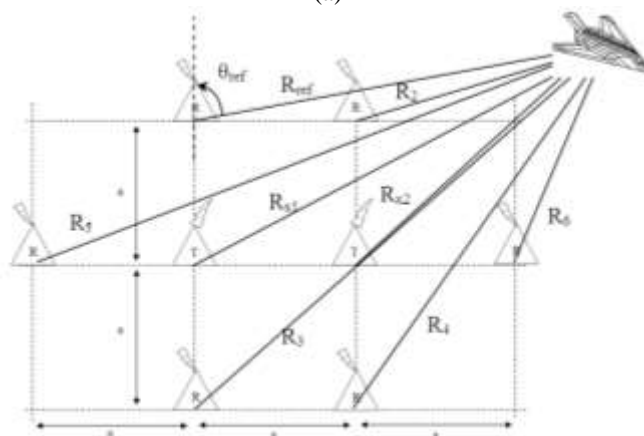
Fig. 1. The combined use of available sources in the process of producing the air picture

V. CONCLUSION

The paper proposes two Multistatic radar system geometries for S-band radar to improve the detection coverage of the small and stealthy aircrafts. The first system geometry G1 consists of 4 transmitters and two receivers while the second one consists of six transmitters and two receivers. The optimum radar spacing for G1 is 48 Km and 50 Km for system geometry G2. The simulation results show that system geometry G1 detection coverage extended 80 Km for small aircrafts over detected by Monostatic radar and 62 Km for stealthy aircrafts. System geometry G2 extends the detection coverage 85 Km with small aircrafts and 69 Km for stealthy aircrafts. The results show that the extended range from the first system geometry satisfies the need for the small and stealthy aircrafts detection with economic number of radar stations.



(a)



(b)

Fig. 2. Multistatic Radar System Geometry (a) System Geometry G1 and (b) System Geometry G2

REFERENCES

- [1] Marc Brooker, "The Design and Implementation of a Simulator for Multistatic Radar Systems," PHD Thesis, University of Cape Town, June, 2008.
- [2] Pavel Bezousek, Vladimir Schejbal, "Bistatic and Multistatic Radar Systems," Radioengineering, Vol. 17, No. 3, Sep. 2008.
- [3] Benson Chan, "Receiver Site Optimisation for Passive Coherent Location (PCL) Radar System," Graduation Project, University of Cape Town, Oct., 2008.
- [4] Vladimir S., Dušan Č., Zdeněk N., Jan P., Jiří K., Pavel B., Ondřej F., "Multipath Propagation of UWB Through-Wall Radar and EMC Phenomena," Radioengineering, Vol. 15, No. 4, Dec. 2006.
- [5] Pavel Bezoušek, Marek Pola, Jan Pidanič, "Detection of Multiple Targets by a Multistatic Radar," Number 4., Volume IV., Dec. 2009.
- [6] Steven Kay, "Waveform Design for Multistatic Radar Detection," Dept. of Electrical, Computer, and Biomedical Engineering, University of Rhode Island Kingston, RI 02881, 2007.
- [7] Terje Johnsen and Karl Erik Olsen, "Bi- and Multistatic Radar," Advanced Radar Signal and Data Processing Educational Notes RTO-EN-SET-086, Paper 4. Neuilly-sur-Seine, France: RTO. Available from: <http://www.rto.nato.int/abstracts.asp>, visited Oct. 2010
- [8] Merrill I. Skolnik, "Radar Handbook, Second Edition," McGraw-Hill, 1990
- [9] Bassem R. Mahafza, "Radar Systems Analysis and Design Using MATLAB," CRC Press, USA, 2000
- [10] Chris Baker, "Multistatic radar processing and systems," Advanced Radar Signal and Data Processing Educational Notes RTO-EN-SET-133, Paper 4. Neuilly-sur-Seine, France: RTO. Available from: <http://www.rto.nato.int/abstracts.asp>, visited Oct. 2010

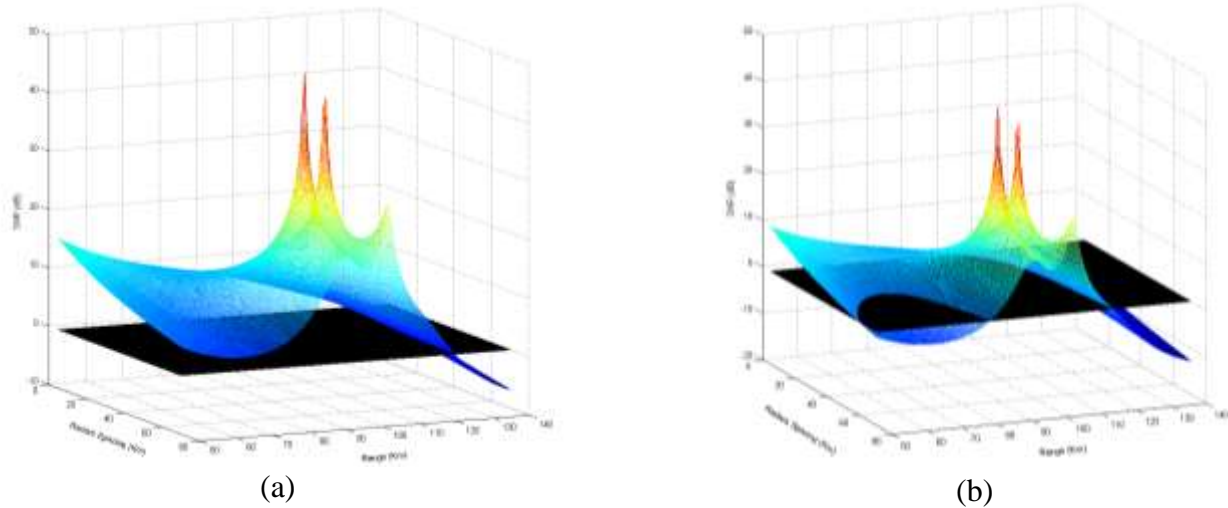


Fig. 3. Received S/N at different radar spacing and target ranges for system geometry G1 (a) Small Aircrafts $\sigma = 0.1 \text{ m}^2$, (b) Stealthy Aircrafts $\sigma = 0.025 \text{ m}^2$.

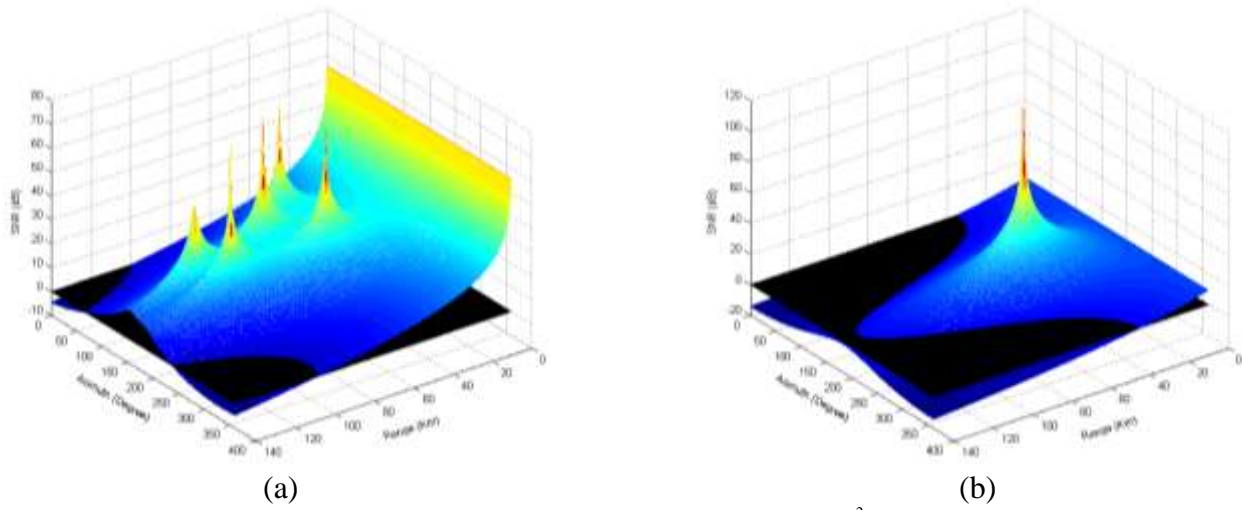


Fig. 4. Received S/N at different azimuth angles and target ranges with small aircrafts $\sigma = 0.1 \text{ m}^2$ (a) Multistatic radar G1, (b) Monostatic radar

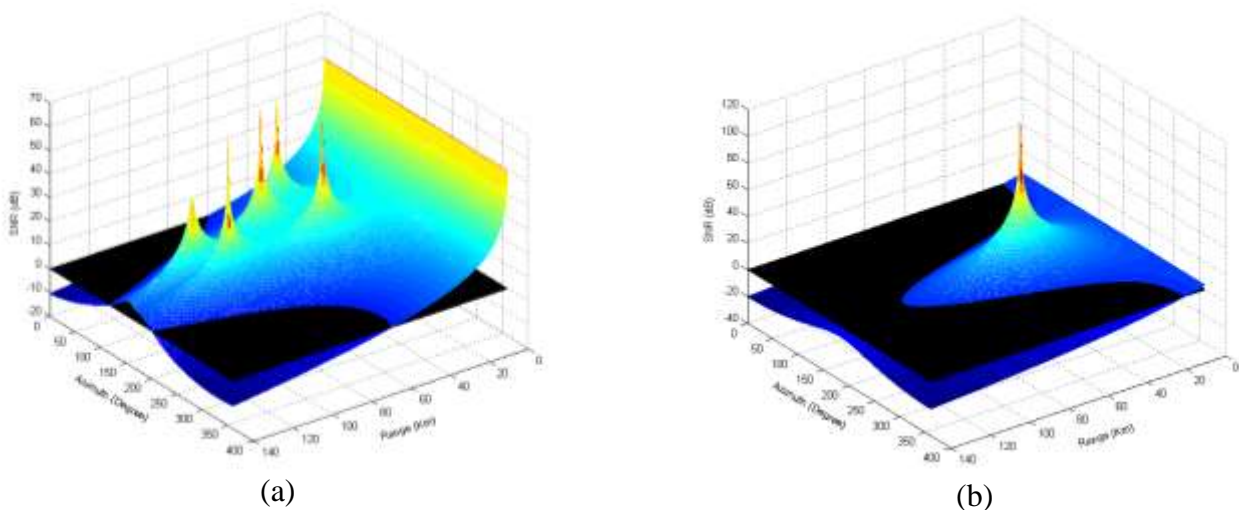


Fig. 5. Received S/N at different azimuth angles and target ranges with stealthy aircrafts $\sigma = 0.025 \text{ m}^2$ (a) Multistatic radar G1, (b) Monostatic radar

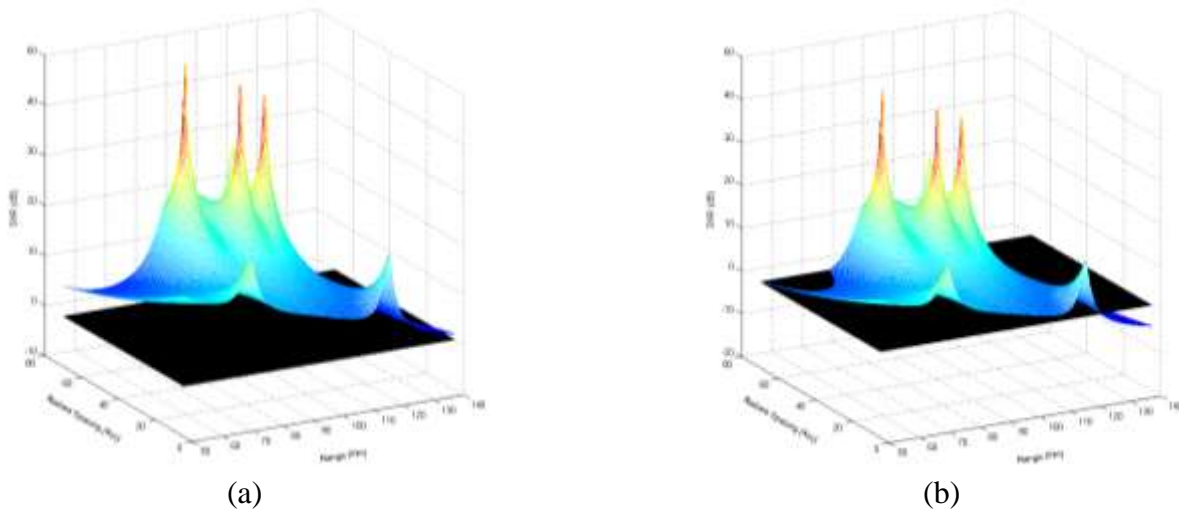


Fig. 6. Received S/N at different radar spacing and target range for system geometry G2 (a) Small Aircrafts $\sigma = 0.1 \text{ m}^2$, (b) Stealthy Aircrafts $\sigma = 0.025 \text{ m}^2$.

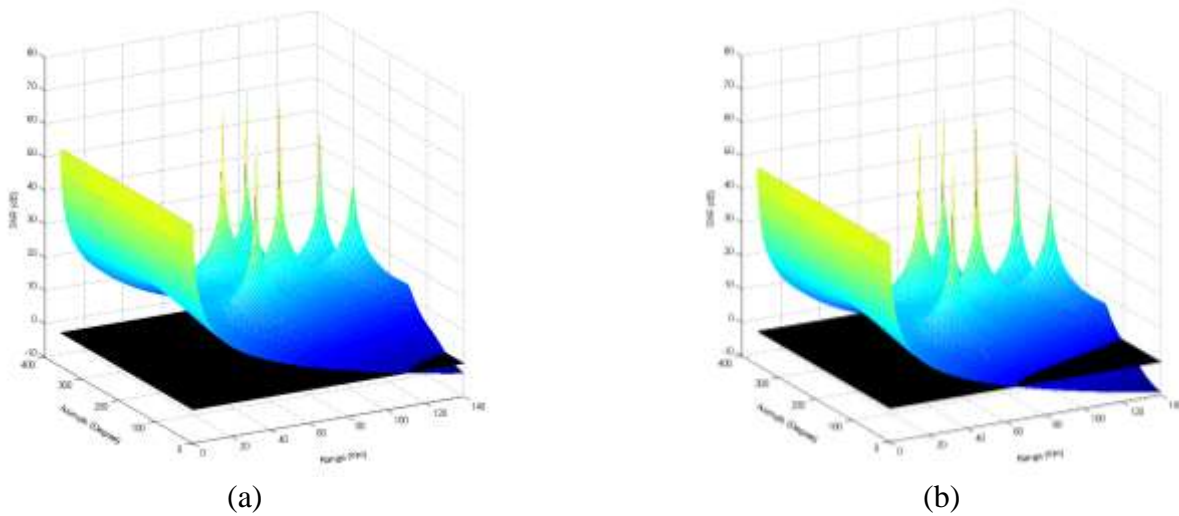


Fig. 7. Received S/N at different azimuth angles and target ranges G2 (a) Small Aircrafts $\sigma = 0.1 \text{ m}^2$, (b) Stealthy Aircrafts $\sigma = 0.025 \text{ m}^2$.

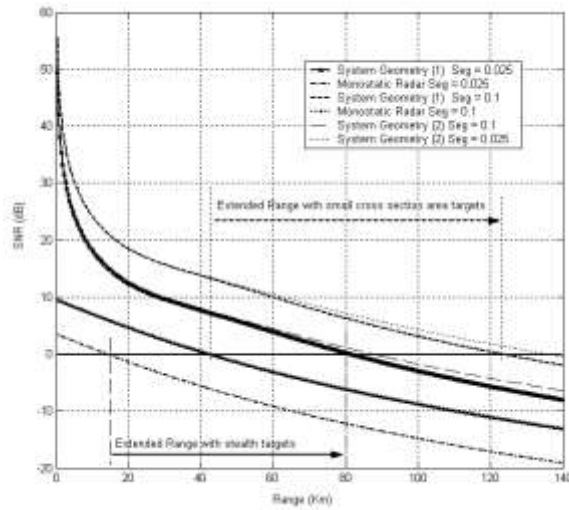


Fig. 8. Received S/N versus target range for Multistatic radar G1, G2, and Monostatic radar with target cross section $\sigma = 0.1 \text{ m}^2$ and $\sigma = 0.025 \text{ m}^2$.

Biographies



Hassan El-Kamchouchy is professor in Faculty of Engineering, Alexandria University, Alexandria, Egypt. He holds B.Sc. in Electronics and Communications from Faculty of Engineering, Alexandria University, He also holds M.Sc. and Ph.D. in Electrical Engineering from Faculty of Engineering, Alexandria University. He received many technical courses in Electronic system design and Implementation, work as System Engineer for more than 20 years, teach up to 30 undergraduate subjects, supervising more than 75 thesis, publish more than 150 papers in different international conferences and Journals



Khaled Samir Saada is a Post Graduate Student (Ph.D.), Alexandria University, Alexandria, Egypt. He holds B.Sc. in Electronics and Communications from Faculty of Engineering, Alexandria University, M.Sc. in Electrical Engineering from Faculty of Engineering, Alexandria University. He received many technical courses in electronic engineering design and Implementation.



Alaa El-Din Sayed Hafez is an affiliate instructor in Faculty of Engineering, Alexandria University, Alexandria, Egypt. He holds B.Sc. in Electronics and Communications from Faculty of Engineering, Alexandria University, M.Sc. in Electronics and Communication from Arab Academy for Science and Technology and Maritime Transport, Alexandria. He also holds M.Sc. and Ph.D. in Electrical Engineering from Faculty of Engineering, Alexandria University. He received many technical courses in Surveillance Radar design and Implementation, work as Radar System Engineer for more than 5 years, teach up to 20 undergraduate subjects, supervising more than 12 thesis, publish more than 40 papers in different international conferences and journals.

Dynamic Physical Impairment-Aware Routing and Wavelength Assignment in 10/40/100 Gbps Mixed Line Rate Optical Networks

Filippos BALASIS *, Xin WANG *, Sugang XU *, and Yoshiaki TANAKA * **

* Global Information and Telecommunication Institute, Waseda University, Japan

** Research Institute for Science and Engineering, Waseda University, Japan

fbalasis@akane.waseda.jp, xinwang@ruri.waseda.jp, xusugang@m.ieice.org, ytanaka@waseda.jp

Abstract—The growing global Internet traffic will inevitably lead to a serious upgrade of the current optical networks' capacity. Instead of upgrading the data rate of each wavelength in every fibre link across the entire optical WDM network infrastructure, it is more efficient and cost-effective to support different data rates within one fibre link (e.g., 10, 40 and 100 Gbps). This is called optical network with mixed line rates (MLR). Moving to higher than 10Gbps data rates that can be used within the same fibre requires the implementation of phase modulation schemes. Nevertheless, the co-existing OOK channels cause a critical physical impairment to the phase modulated channels, namely cross-phase modulation (XPM), that limits the network's performance. In order to mitigate this type of impairment a more sophisticated physical impairment aware routing and wavelength assignment scheme needs to be adopted. In this paper, the critical impairment for each data rate and the way it affects quality of transmission (QoT) is presented. Secondly, QoT aware RWA schemes for a MLR optical network are presented and evaluated in terms of performance through simulations.

Keywords—Mixed Line Rate, Optical Network, XPM, ASE, Physical Impairment, RWA

I. INTRODUCTION

The emergence and establishment of bandwidth intensive applications such as IPTV, cloud computing, has led to an explosive growth of the heterogeneous internet traffic. Many technologies have been proposed as candidates for the upgrade of the network's capacity and the greater utilisation of optical fibre's limited bandwidth. However, the concept of

Manuscript received July 10, 2013.

Filippos BALASIS is with the Global Information and Telecommunication Institute, Waseda University, Tokyo, 169-0051, Japan (Tel: +81 3 3203 9450; fax: +81 3 3203 9450; e-mail: fbalasis@akane.waseda.jp).

Xin WANG is with the Global Information and Telecommunication Institute, Waseda University, Tokyo, 169-0051, Japan (Tel: +81 3 3203 9450; fax: +81 3 3203 9450; e-mail: xinwang@ruri.waseda.jp).

Sugang XU is with the Global Information and Telecommunication Institute, Waseda University, Tokyo, 169-0051, Japan. (Tel: +81 3 3203 9450; fax: +81 3 3203 9450; e-mail: xusugang@m.ieice.org).

Yoshiaki TANAKA is with the Global Information and Telecommunication Institute, Waseda University, Tokyo, 169-0051 Japan. He is also with the Research Institute for Science and Engineering, Waseda University, Tokyo, 162-0044 Japan (Tel: +81 3 3209 5210; fax: +81 3 3209 5210; e-mail: ytanaka@waseda.jp).

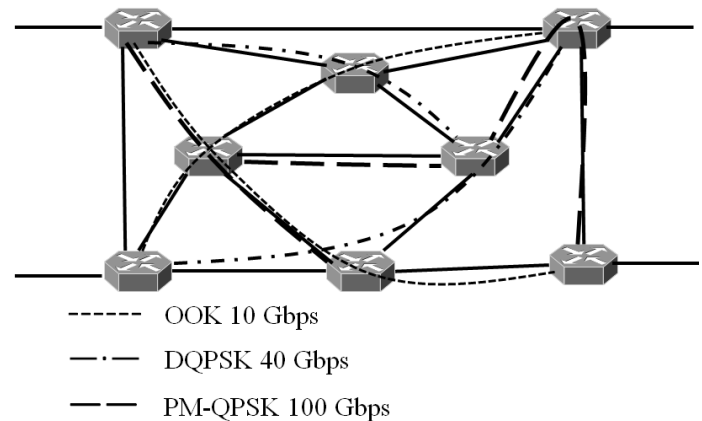


Fig. 1. A wavelength switched optical network with mixed line rates and multiple modulation formats.

MLR optical network has recently drawn the academic community's attention due to its cost and energy efficiency [1]-[3]. Other advantages of mixing different rates within the same fibre link are the more gradual and cost-effective upgrade of the capacity and the fact that it is possible to apply into the current WDM network infrastructure without many modifications [4]. Some early experiments from Nokia Siemens and Alcatel [5],[6] have shown the industry's interest as well.

Until recently, the highest data rate available in a wavelength channel was 10 Gbps achieved through on-off keying (OOK) modulation format within the standard ITU grid of 50 GHz. In order to migrate to higher data rates with the same spectral separation more advanced and spectral efficient phase modulation schemes are needed. The most promising candidates, in terms of noise resiliency, for 40 Gbps and 100 Gbps transmission have been DQPSK and PM-QPSK respectively and are the ones that are considered in our study. Fig. 1 depicts such an optical network with mixed line rate and multiple modulation formats. Nevertheless, the biggest obstacle for the realisation of a MLR optical network is XPM occurred to the xPSK channels by the adjacent 10 Gbps OOK channels. This non-linear impairment is caused by the Kerr effect [7]. The high optical intensity of the propagated OOK pulses generates oscillations in the refractive index of the

fibre's material. The changes of the refractive index produce a non-linear phase shift to the adjacent xPSK channels and thus increase the bit error rate at the receiver. In order to overcome this impairment that affects performance a more sophisticated physical impairment (PI) aware routing and wavelength assignment (RWA) scheme that ensures quality of transmission (QoT) is needed.

The challenge of developing a PI-aware for such non-linear impairment is not only the more complex calculation of the accumulated phase noise along the candidate path but also the calculation of the distortion caused to the already established lightpaths. To the knowledge of this paper's authors, with the exception of [8] and [9], there are not many proposals in the literature for XPM-aware provisioning of MLR optical networks. In [8], the authors consider a design of such a network in the static scenario only and they propose an algorithm that adapts the optical reach of 40Gbps channels whenever they co-propagate with 10Gbps ones. However, they apply a fixed parameter to modify the length of a fibre link regardless of the number of co-existing 10Gbps channels or their spectral separation with the 40Gbps ones and thus, they do not accurately estimate the XPM impairment. In [9], the authors consider a MLR optical network where each lightpath is set up dynamically and its QoT metrics are calculated based on analytical models. They also consider the worst case scenario for XPM impairment whenever a xPSK lightpath is established and the use of guard bands between xPSK and OOK channels. However, the overestimation of XPM impairment can cause unnecessary blocking of xPSK lightpath requests and the use of guard bands may lead to inefficient use of wavelength resources in order to secure QoT for xPSK connections.

In this paper, we study the case of dynamically set up lightpaths in a MLR optical network realised by transceivers that can be either tuned or not on a fixed data rate and modulation format. For that case, we present and compare two novel PI-aware RWA schemes that take into account the presence of XPM impairment and optimises performance and resource utilisation. The rest of this paper is organized as follows. In section II, we describe the types of impairment and their calculation method for OOK, DQPSK and PM-QPSK channels respectively. In section III, we present the concepts behind the proposed algorithms. In section IV, our methods are compared to the shortest path and minimum hop routing schemes. For the comparison, the case study via simulation and its results are shown. Finally, section V concludes this paper.

II. PHYSICAL IMPAIRMENTS IN OOK, DQPSK AND PM-QPSK WAVELENGTH CHANNELS

A. OOK

In optical transmission that uses OOK scheme amplified spontaneous emission noise (ASE) and chromatic dispersion (CD) are the most critical impairments. Since CD can be

managed through dispersion compensation fibres (DCF), our study focuses on ASE noise only. For future work however, we intend to include other types of impairment as well, such as polarization mode dispersion (PMD) and switching crosstalk. ASE noise is due to the spontaneously emitted photons by the fibre's material. This radiation cannot be distinguished by the optical amplifier and therefore is amplified along with the propagating optical pulse and added as noise to the signal [7]. If erbium-doped fibre amplifiers (EDFA) are considered then the ASE noise power at the output of the amplifier is calculated as Eq.(1) [7]:

$$P_{ASE} = 2n_{sp}hf_0(G-1)B_0 \quad (1)$$

where n_{sp} is the spontaneous emission factor, h the Planck constant, f_0 the frequency of the propagating signal, G the gain of the amplifier and B_0 the optical bandwidth of the receiver. In the case of distributed amplification across the fibre links, then after N_i spans in a fibre link i the total accumulated ASE noise power is Eq.(2) [7]:

$$P_{ASE,i} = 2n_{sp}hf_0N_i(G-1)B_0, N_i=L_i/l_s \quad (2)$$

where L_i is the length of the link i and l_s the length of the span. The optical SNR is calculated as Eq.(3) [7]:

$$SNR_o = P_{in}/P_{ASE} \quad (3)$$

where P_{in} is the average power of the optical signal that due to the distributed amplifying is considered constant. From the SNR_o it is possible to calculate the BER of the OOK signals by the following Eqs.(4) and (5) [7]:

$$BER_{OOK} \approx \frac{1}{2} \operatorname{erfc}(Q/\sqrt{2}) \approx \frac{\exp(-Q^2)}{Q\sqrt{2\pi}} \quad (4)$$

$$Q = \frac{SNR_o\sqrt{M}}{\sqrt{SNR_o+1+1}} \quad (5)$$

where $M=2B_0T$, $B_0=50\text{GHz}$ the optical bandwidth of the receiver and T the symbol duration (100ps for OOK channels).

B. DQPSK

The calculation of impairment for the DQPSK channels is more rigorous since, in addition to the XPM, ASE noise also causes a non-linear phase shift to the propagating signal. Moreover, the XPM impairment induced in fibre link i by an adjacent OOK channel j depends on its power level and spectral distance. The variance of non linear phase noise caused by XPM is shown as Eq.(6) – Eq.(8) [9]:

$$\sigma_{i,j}^2 = \frac{\varphi_{i,j}^2 \tau_{i,j}}{T_j} \left\{ 2c_1 - c_2 \exp\left(-\frac{T}{\tau_{i,j}}\right) \right\} \quad (6)$$

$$\varphi_{i,j} = \frac{2\gamma_i P_{i,j}}{a_i}, \quad \tau_{i,j} = \frac{|D_i \Delta \lambda_i|}{a_i} \quad (7)$$

$$c_1 = \exp\left(-\frac{T_j}{\tau_{i,j}}\right) + \frac{T_j}{\tau_{i,j}} - 1, c_2 = \cosh\left(\frac{T_j}{\tau_{i,j}}\right) - 1 \quad (8)$$

where α_i , D_i and γ_i are the attenuation, dispersion parameter, and nonlinear Kerr coefficient of fibre, respectively. T_j , $\Delta\lambda_j$ and $P_{i,j}$ are the bit-time of the interfering OOK channel, its spectral separation with respect to the DQPSK channel, and its average power at the input of the fibre, respectively.

The total variance of the non-linear phase noise in a link i and a route r can be calculated with Eq.(9), (10) [9] [10]:

$$\sigma_{\text{XPM}}^2 = \sum_{i \in r} \sigma_{\text{XPM},i}^2 \quad (9)$$

$$\sigma_{\text{XPM},i}^2 = \sum_{j=1}^n \mu_j \sigma_{i,j}^2 \quad (10)$$

where the parameter $\mu_j = 0, 1$ indicates whether the OOK channel j is active or not, and n is the number of the wavelength channels of the link with OOK modulation.

The phase shift variance caused by ASE noise is calculated as Eqs.(11) and (12) [10]:

$$\sigma_{\text{ASE}}^2 = 1/\rho, \quad (11)$$

$$\rho = n \cdot B_{\text{REF}} T \text{SNR}_0 \quad (12)$$

where ρ is the SNR per symbol, $n=2$, B_{REF} is the reference bandwidth in which OSNR is measured (12.5 GHz) and T is the symbol duration (50 ps for 40 Gbps DQPSK channels). Finally, the BER due to phase noise for a DQPSK connection is calculated as Eqs.(13) and (14) [9],[10]:

$$\text{BER} = \frac{3}{8} - \frac{\rho}{4} \exp(-\rho) \sum_{m=1}^{\infty} \left[I_{m-1}\left(\frac{\rho}{2}\right) + I_{m+1}\left(\frac{\rho}{2}\right) \right] \cdot \frac{\sin\left(\frac{m\pi}{4}\right)}{m} \exp(-m^2 \sigma_T^2 / 2) \quad (13)$$

$$\sigma_T^2 = \sigma_{\text{XPM}}^2 + \sigma_{\text{ASE}}^2 \quad (14)$$

where is $I_k(x)$ the k -order modified Bessel function of the first kind. The BER formula can be calculated with very good approximation within a finite number of terms.

C. PM-QPSK

In PM-QPSK modulation scheme, each wavelength channel carries two orthogonally polarised QPSK modulated bit streams. Therefore, in this case the QoT model is similar to that of DQPSK. However, there are some differences that need to be taken into account. First of all, since there are two polarisations of the signal, Eq.(13) will change into Eq.(15) [9]:

$$\rho = n' \cdot B_{\text{REF}} T \text{SNR}_0 \quad (15)$$

where $n'=1$ and $T'=40$ ps (because the symbol rate is equal to 25 Gbaud/sec).

Additionally, in PM-QPSK transmission, not differential but coherent detection technique is used instead in the receiver. The phase estimation algorithm takes into account K previously received symbols and this affects the method the XPM phase noise variance is calculated [9]. Particularly, Eq.(6) is modified as shown in Eq.(16) [9]:

$$\sigma_{i,j}^2 = \frac{\varphi_{i,j}^2 \tau_{i,j}}{T_j} \left\{ \frac{K+1}{K} c_1 - \frac{c_2}{K^2} \sum_{n=1}^K n \exp\left(-\frac{nT}{\tau_{i,j}}\right) \right\} \quad (16)$$

where K is the number of past symbols. $K=6$ is assumed for optimal phase detection [10]. Finally, the BER for QPSK modulation is calculated as Eq.(17) [9], [10]:

$$\text{BER} = \frac{3}{8} - \frac{1}{2} \frac{\sqrt{\rho}}{\pi} \exp(-\rho) \sum_{m=1}^{\infty} \left[I_{m-1}\left(\frac{\rho}{2}\right) + I_{m+1}\left(\frac{\rho}{2}\right) \right] \cdot \frac{\sin\left(\frac{m\pi}{4}\right)}{m} \exp(-m^2 \sigma_T^2 / 2) \quad (17)$$

III. QOT-AWARE PROVISIONING OF THE LIGHTPATHS

A. Type of Transponders and Wavelength Selection Strategy

As shown in Eqs.(6)-(8), the XPM induced phase shift depends mainly on the spectral distance and power levels of the adjacent OOK channels. Due to the complexity of defining the optimal power level, especially in a dynamic scenario, power management is left for future work. Instead, this paper is mainly focusing on provisioning the lightpaths in such way so that the xPSK channels have the maximum as possible spectral separation from the OOK channels. This requires a specific placement of the channels in the fibre's spectrum and a particular wavelength selection scheme as well. In addition to the wavelength selection strategy that will prevent the xPSK channels to entangle with the OOK channels in the fibre's spectrum, another factor that should be taken into account when planning MLR optical networks is the type of the used transponders. The transponders can be either fixed, namely, tuned on a specific wavelength and bit rate, or fully tunable where the wavelength, the bit rate and the modulation format can be configured dynamically on request. A tunable optical transponder has the obvious advantage of greater flexibility and efficiency in the usage of wavelength resources and thus, for the same traffic demands, a network with tunable transponders is expected to perform better than a network with fixed ones. In Fig. 2 the architecture of an optical add-drop multiplexer (OADM) node is shown where the optical transponders are assumed to be tunable.

Although multirate transponders have become recently available, the range of the variable bit rate is still limited and is achieved through the same modulation scheme. An optical transceiver with adaptive modulation format is needed in

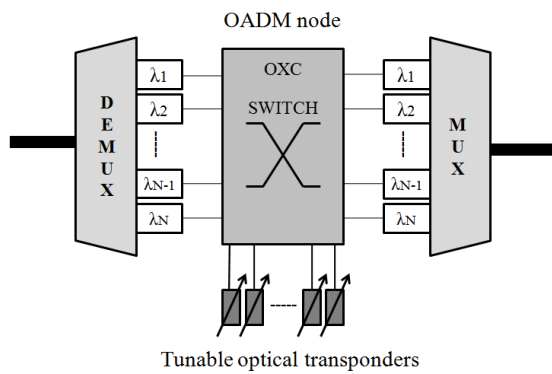


Fig. 2. A node with an optical add-drop multiplexer (OADM) and tunable optical transponders.

order to scale from 10Gbps up to 100Gbps because OOK modulation is still preferred for lower data rates due to its longer optical reach and lower energy consumption [3],[11]. Currently, there are no transponders commercially available that employ different modulation formats and when they get released it is almost certain that the implementation cost will be high. Furthermore, in the case of a MLR optical network the probability of xPSK channels intermingling with OOK ones is higher and hence some wavelength channels need to be inactive in order to guarantee QoT for 40G and 100G transmission. In other words, the complexity of the QoT model increases. On the other hand, fixed rate transponders, are more affordable and more realistic in terms of implementation. In addition to their cost effectiveness, the problem of optimising the provisioning of the lightpaths is simplified. For the sake of a more complete research scope, both scenarios of a MLR network with tunable and fixed rate transponders are examined separately. Moreover, in the case where fixed rate transponders are considered, various combinations of data rates are examined.

Either way, a wavelength selection strategy that considers the XPM physical impairment can be proven quite beneficial to network's performance. In the case of a MLR network with fully tunable transponders, the first-fit (FF) for xPSK lightpaths and last-fit (LF) for OOK ones becomes the obvious optimal choice. This is so as to maximise the spectral separation among these two types of lightpaths. Furthermore, when fixed rate transponders are only available, in addition to the FF-LF strategy, a specific tuning of the transceivers is required. Particularly, the optimal placement of the wavelength channels in the fibre's spectrum is shown in Fig. 3, where the channels of the same data rate (or modulation scheme) are grouped in line. Whether there can be a fixed number of inactive wavelengths between the xPSK and the OOK channels or not, is left to the operators' judgement which will be based on real world measurements. In this paper however, no guard-band is considered for the purpose of maximising spectral efficiency (e.g., the possibility of an xPSK connection next to an OOK one satisfying the BER threshold due to link's short distance). Besides the wavelength

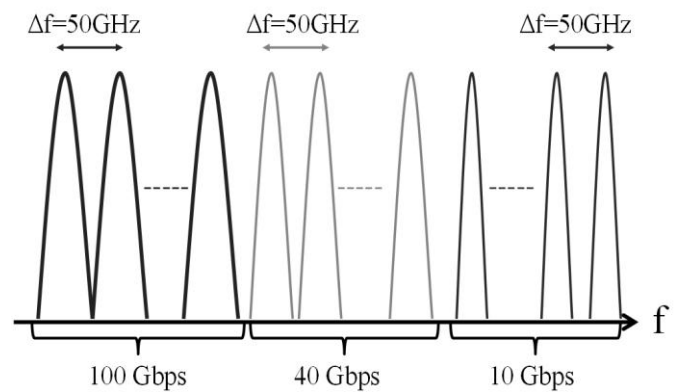


Fig. 3. Tuning of the fixed rate optical transponders in the fibre's spectrum according to their data rate.

selection strategy and the tuning of the transceivers, as it is presented in the following part of this section, for the case of xPSK lightpaths, knowing in advance which wavelength is going to be assigned is required for the choice of the optimal path. This is why in our proposed method, when a connection request arrives, the FF wavelength is assigned first and then the route with the minimum XPM impairment is calculated.

B. QoT Estimation Model

In a MLR optical network, the provisioning of the lightpaths requires different treatment for OOK and xPSK requests respectively. For the 10 Gbps connections, the path with the shortest length or minimum number of hops remains the optimal choice, since ASE noise is the main impairment. Nevertheless, this cannot be applied to the xPSK lightpaths since besides ASE noise, XPM is a nonlinear impairment that depends on the number and spectral distance of the already existing 10Gbps lightpaths and must also be taken into account. What is more, when searching an optimal route for an OOK lightpath, it should be investigated whether its set up can lead to a serious XPM impairment to the already established xPSK lightpaths. Therefore, an efficient RWA scheme should be able to adapt on the data rate of an incoming connection request. Next, the routing methods for xPSK and OOK lightpaths are separately described and then the PI-aware schemes are presented in steps.

DQPSK and PM-QPSK Lightpaths

Regarding the xPSK lightpaths (40Gbps and 100Gbps connections), a physical impairment-aware routing and wavelength assignment algorithm is proposed to calculate the path that offers the minimum BER for a source-destination pair. To achieve this, to every link, a weight is assigned that equals to the phase noise variance of that link. Since the phase variances per link can be added linearly, as shown in Eqs.(9) and (14), it is possible, by finding the "shortest" path in terms of weights, to ensure that the least OOK congested links will be selected and that this path will offer low BER. At this point, it should be noted that, besides the XPM noise variance, the ASE induced noise variance can also be added

linearly per link. If the distributed amplification through EDFA modules is considered, then for a link i the ASE phase noise variance is calculated as shown in Eq.(18):

$$\sigma_{ASE,i}^2 = \frac{1}{\rho} = 1/(n \cdot B_{REF} \cdot TSNR_o) = P_{ASE,i}/n \cdot B_{REF} \cdot T \cdot P_{in} \quad (18)$$

where $P_{ASE,i}$ is the ASE noise in link i . And as it is shown in Eq.(3) the ASE noise can be added linearly in every route. Therefore, we can define as weight W_i for every link i its total phase noise variance, Eq.(19):

$$W_i = \sigma_{XPM,i}^2 + \sigma_{ASE,i}^2 \quad (19)$$

The benefit of this method compared to other XPM-aware RWA schemes is that it is less XPM-biased and more accurate in the estimation of QoT. To be more specific, if the avoidance of links with established OOK lightpaths is the only criterion in the lightpath provisioning, then this may lead to a miscalculation of the optimal path since the ASE induced phase noise of a much longer route can outweigh the XPM impairment of other candidate paths.

Furthermore, assuming distributed amplification across the network, we can consider the power of the optical signal to be stable. Therefore, the only parameter that changes in Eq.(6)-(8) is the one of spectral separation which has a unit of 50 GHz (ITU grid) [4]-[6]. When fixed rate transponders are used in the network the number and type of wavelengths (OOK or xPSK) supported in every link are known in advance. Therefore, it is possible for a specific xPSK wavelength, to pre-compute the XPM phase noise variance caused by every OOK wavelength independently (e.g. applying in Eq.(6) OOK wavelength $j, j+1, j+2...$). Then, by knowing which OOK wavelengths are currently being used in a link, the weight of that link is calculated by Eq.(10). This simplifies the procedure of finding the optimal path for an xPSK connection as well as the calculation of the distortion caused by a number of OOK lightpaths. Assuming that in a fibre link i there are m and n wavelengths carrying xPSK and OOK signals respectively and arranged as in Fig. 3, it is possible to express the above concept with the following formula Eq.(20):

$$W_i^T = A_i M^T + C_{ASE,i}^T \quad (20)$$

where W_i is the $1 \times m$ row vector containing the weights of all xPSK wavelengths for link i , A_i is the $m \times n$ matrix that contains the phase noise variances for every combined pair between a xPSK and an OOK channel in link i , (e.g. element $a_{k,l}$ ($1 \leq k \leq m, 1 \leq l \leq n$) is equal to the variance of the non-linear phase noise induced by OOK channel l to xPSK channel k , Eq.(9)), M is the row vector containing the μ parameter from Eq.(10) for every OOK wavelength in the link and $C_{ASE,i}$ the row vector that contains all ASE induced phase noise variances for every xPSK wavelength in link i . The elements

of matrix A_i and vector $C_{ASE,i}$ can be pre-computed and considered constants while the elements of vector M , that show which OOK wavelengths are currently being used in the link, are the only variables that change in time.

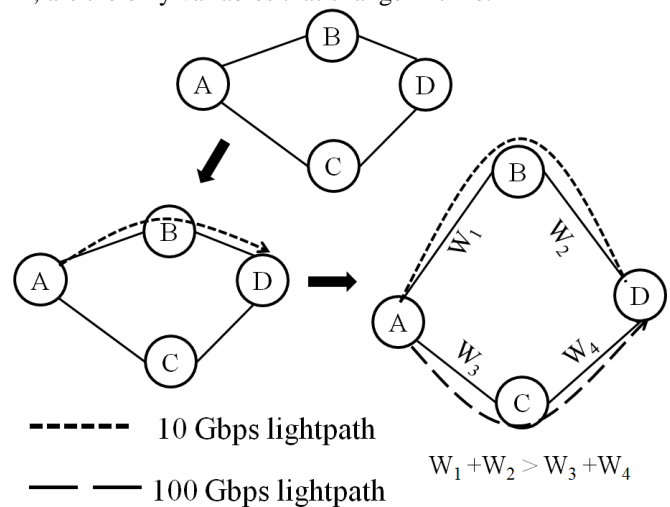


Fig. 4. When an xPSK lightpath is about to be set up, weights are applied to each link of the network's topology and their value depends on the number and spectral adjacency of the established OOK lightpaths.

When fully tunable transponders are considered, the complexity for the calculation of the phase noise variance increases along with the possible combinations of wavelengths in the available spectrum. Nevertheless, the same logic can be applied to reduce online calculation time. Assuming that there are n supported wavelengths in a fibre link, the number of possible XPM noise variances caused by one OOK lightpath is $n-1$. Again, by using Eq.(6) we can define the XPM noise variance caused by an OOK lightpath that is j wavelengths away as $\sigma_j^2, 1 \leq j \leq n-1$. Hence, by pre-computing all possible values of σ_j^2 the total XPM noise variance in link i for a xPSK lightpath that uses wavelength k is, Eq.(21) :

$$\sigma_{XPM,i}^2 = \sum_{l=1, l \neq k}^n m_l \cdot \sigma_{|k-l|}^2 \quad (21)$$

where index $m_l = \{0,1\}$ is 1 when wavelength l is used by an OOK lightpath.

A simple example of the proposed scheme can be seen in Fig. 4. When a request for a 10Gbps connection arrives between nodes A and D, the optimal path is the one with the shortest length $A \rightarrow B \rightarrow D$. Once it is established and a new 100Gbps request arrives between the same nodes, weights will be applied to the topology's links in order to find the optimal route as described above. The presence of the already established 10Gbps lightpath will result to larger weights for the route $A \rightarrow B \rightarrow D$ and therefore $A \rightarrow C \rightarrow D$ route is opted.

OOK Lightpaths

Regarding the 10Gbps lightpaths that make use of OOK scheme two methods can be applied: i) When a 10Gbps connection request arrives, the wavelength is assigned first

according to FF-LF strategy and then the shortest path is established. ii) A route is found through the k-shortest fixed length path algorithm and then the wavelength is assigned. The first method sets as a priority the protection of xPSK lightpaths and the objective is to assign a wavelength to the OOK lightpath that is as distant as possible from the wavelengths of xPSK lightpaths. However, assigning the wavelength first might not lead to the shortest length or minimum hop route to the destination node. The second method on the other hand is more conventional and more beneficial to the QoT of OOK lightpaths but the risk of setting an OOK lightpath closer to a xPSK one is higher.

As a result, two schemes can be derived from the above analysis and their distinction lies on the way they handle the 10Gbps lightpaths: i) Minimum weight path for xPSK lightpaths and first wavelength then shortest length path for OOK lightpaths (MW-FW); ii) Minimum weight path for xPSK lightpaths and first shortest length path then wavelength assignment for OOK lightpaths (MW-FP). Both of the algorithms are presented in steps as follows:

MW-FW Algorithm steps

Step 1: When a new connection request arrives, select a wavelength according to the First-Fit/Last-Fit strategy described above. If no available wavelength is found then block the request;

Step 2: If a wavelength is available then select it as the candidate wavelength, and find the optimal route for this wavelength:

- 1) For xPSK requests a modified Dijkstra algorithm aforementioned is employed by setting a weight to each link, i.e., with the value of the phase noise variance of that link.
- 2) For OOK requests standard Dijkstra algorithm for shortest path calculation is employed.

The links where the candidate wavelength is already occupied, are considered to have infinite weight/length. If no route to destination is found, then go back to Step 1 to select another candidate wavelength;

Step 3: If a route to destination is found then calculate the BER. If it is below threshold:

- 1) For xPSK requests establish the lightpath.
- 2) For OOK establish only if it does not violate the QoT of already existing xPSK lightpaths.

If the BER is not satisfied or there is violation to the existing lightpaths then go to Step 1 to select another candidate wavelength;

Step 4: If a new OOK lightpath is established or released update the XPM variances and BER of the affected xPSK lightpaths.

MW-FP Algorithm steps

Step 1: When a new connection request arrives:

If it is a xPSK lightpath request go to **Step 2** else go to **Step 3**;

Step 2: Search for an available wavelength according to First-Fit strategy. If no wavelength is found block the request else use the modified Dijkstra where the weight of each link equals the phase noise variance of that link; The links where the candidate wavelength is already occupied, are considered to have infinite weight/length. If no route to destination is found, then select the next available wavelength and repeat **Step 2** else go to **Step 4**;

Step 3: In the shortest length path to the destination search for an available wavelength with Last-Fit strategy. If no wavelength is found proceed to the next path in the list of the k-shortest length paths and repeat the procedure. If no free wavelength is found for all k-shortest paths block the request, else go to **Step 4**;

Step 4: If a route to destination is found then calculate the BER:

- 1) For xPSK if it is below threshold establish the lightpath, else go to **Step 2**;
- 2) For OOK if it is below threshold and does not violate the QoT of already existing xPSK lightpaths establish the lightpath, else go to **Step 3**;

Step 5: If a new OOK lightpath is established or released update the XPM variances and BER of the affected xPSK lightpaths.

IV. SIMULATION AND RESULTS

A. Optical Transponder Considerations

Depending on whether fixed wavelength-rate or fully tunable transponders are implemented in the network, there is a difference in checking availability for a wavelength or transponder when a connection request arrives. In the case of fixed transponders, in order to set a lightpath with a specific wavelength and data rate, both concerned transponders in the source and destination nodes should be available, i.e. in idle state. Therefore, when a RWA algorithm is running, a candidate wavelength is considered available if the following conditions are satisfied: i) the wavelength continuity constraint along the route is not violated; ii) the transponders that are tuned on that specific wavelength in source-destination nodes are not currently used by other lightpaths. Hence, a connection request in a fixed transponder network might be blocked because no transponder of that rate is available or there is no "matching" pair of transponders in terms of wavelength and data rate between source and destination nodes. In the case of fully tunable transponders however, the latter limitations do not exist. Between any two transponders in two different nodes, it is possible to establish a lightpath at any data rate or wavelength as long as there is no violation of wavelength continuity constraint or QoT threshold. Thus, when a RWA scheme is searching for an available

Parameter	Value	Parameter	Value
B_o	50 GHz	Dispersion parameter	17ps/nm/km
P_{in}	1 mW	Span length	60 km
ASE factor n_{sp}	1.5	Nonlinear Kerr coefficient	$2.2(W \cdot m)^{-1}$
Amplifier gain G	10 dB	Fiber attenuation	0.2db/km
Channel spacing	50GHz		
BER threshold	10^{-9}		

wavelength it will start examining from one end of the spectrum (first in order for an xPSK lightpath and last in order for OOK one) and will stop when it finds a wavelength that satisfies the conditions for the lightpath establishment or reaches the other end of the spectrum and blocks the connection request..

B. Simulation Conditions

To evaluate the proposed methods we compare them with the shortest path and minimum hop routing schemes. All of them will use the same FF-LF wavelength selection strategy and the QoT metrics presented in section II to define whether the incoming request will be blocked or not. The simulations use NSF network's topology with 14 nodes and 21 bidirectional links as depicted in Fig. 5. Every fibre link supports 40 wavelengths. In the current study the length of the network's links is downsized by a factor of 10, instead of thousand kilometres per link, hundreds are considered in the simulations. As mentioned in Section III-A both scenarios of a MLR network with fixed rate as well as tunable transponders are examined separately. For a network that uses fixed rate transponders four different combinations are investigated: i) 20 OOK 10Gbps — 20 DQPSK 40Gbps wavelength channels in every link (Fig. 6) ii) 20 OOK 10Gbps — 20 PM-QPSK 100Gbps wavelengths (Fig. 7) iii) 20 OOK 10 Gbps — 10 DQPSK 40Gbps — 10 PM-QPSK 100Gbps wavelengths (Fig. 8) and iv) 14 OOK 10 Gbps — 13 DQPSK 40Gbps — 13 PM-QPSK 100Gbps wavelengths (Fig. 9). In any case, the transponders are assumed to be tuned as explained in Section II-A (Fig. 3). Moreover, the results for the MLR network with tunable transponders (scenario v) are shown in Fig. 10. For all scenarios the number of transponders in every node is assumed to be 40. The lightpath requests arrive in Poisson process and are uniformly distributed among all source-destination pairs and the available data rates. That means in the scenarios i) and ii) the probabilities of a 10Gbps lightpath request and a 40/100 Gbps request, P_{10G} , P_{40G} and P_{100G} respectively, are the same and equal to 0.5. Similarly, in the scenario iii) it is $P_{40G}=P_{100G}=0.25$ and $P_{10G}=0.5$ and in scenario iv) it is $P_{40G}=P_{100G}=P_{10G} \approx 0.33$. The probability condition of requests of scenario iv) are also applied to the scenario v) where tunable transponders are assumed. The holding time of the lightpaths is exponentially distributed. Other parameters of the simulations are shown in Table 1.

TABLE I
PARAMETER CONFIGURATION EMPLOYED IN SIMULATIONS

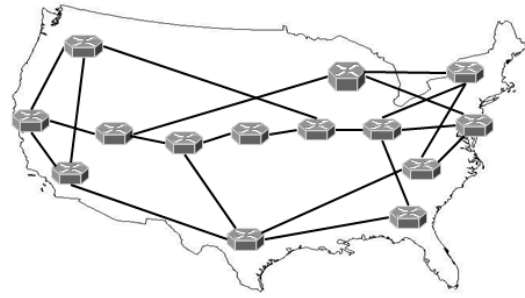


Fig. 5. NSF network topology used in the simulations.

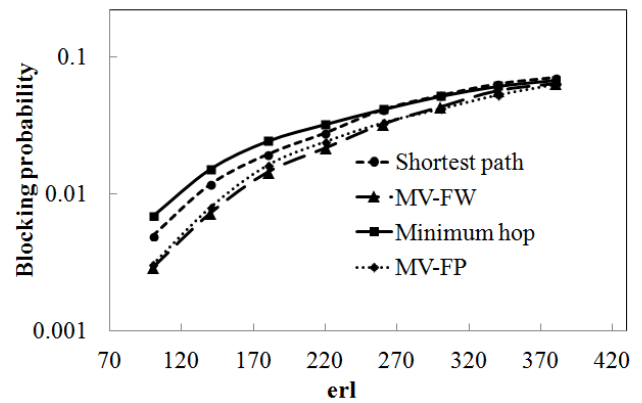


Fig. 6. Blocking Probability in the 10-40 Gbps scenario i).

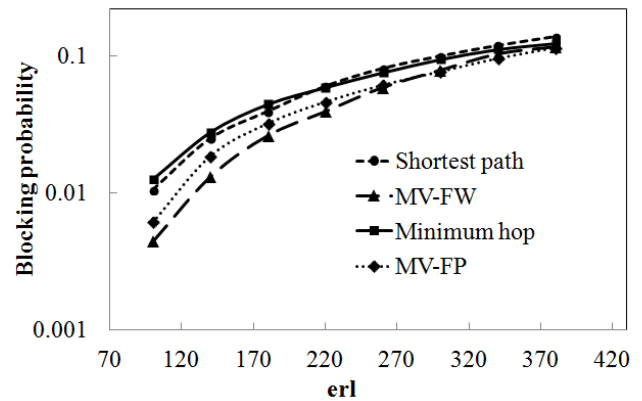


Fig. 7. Blocking probability in the 10-100 Gbps scenario ii).

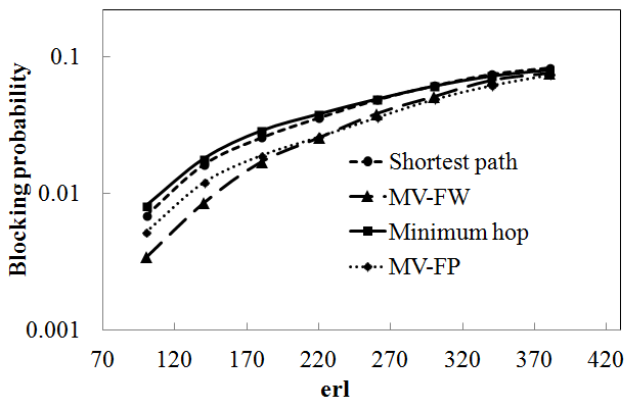


Fig. 8. Blocking probability in the 10-40-100 Gbps scenario iii).

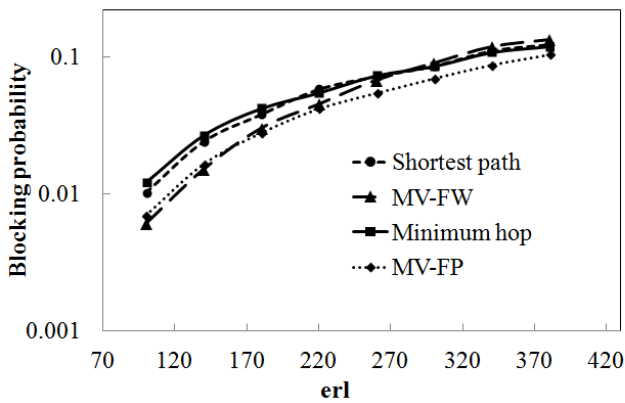


Fig. 9. Blocking probability in the 10-40-100 Gbps scenario iv).

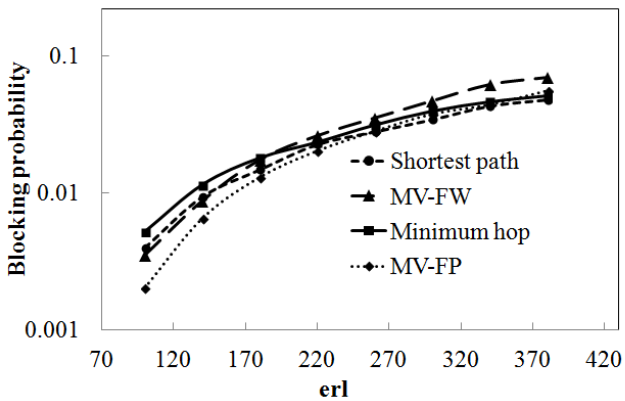


Fig. 10. Blocking probability in the 10-40-100 Gbps scenario v) with tunable transponders.

C. Simulation Results

The blocking probability performances are plotted in Figs. 6 - 10. The figures show that when networks with fixed rate transponders are considered the proposed methods offers superior performance, especially under moderate traffic load.

When the traffic load increases the advantage of the proposed scheme over the compared methods diminishes. This is probably due to the fact that along as the traffic is not large, our proposed schemes assign the lightpaths by efficiently utilizing the network's available wavelengths. While under heavy traffic load, the links are heavily congested and thus XPM noise and wavelength unavailability become unavoidable. The highest blocking probability is observed in Fig. 7. That is expected since 100 Gbps lightpaths are more vulnerable to XPM and ASE noise than the 40 Gbps lightpaths in scenario i). This can be seen by their BER formulas (Eq.(13) and (17)). Moreover, the results in Figs. 6 and 8 are similar because the wavelength channels placed in the first 10 places of the spectrum (10 number of 40Gbps channels in scenario i) and 10 number of 100Gbps channels in scenario iii) are fairly protected from the OOK channels (placed 21-40) since they are separated by at least 10 wavelengths. Therefore, the main reason of blocking for these wavelengths (places 1-10) in both scenarios is ASE noise and wavelength unavailability. In total, the proposed schemes are proven to be more beneficial in terms of performance in scenarios i)–iii). In scenario iv) (as shown in Fig. 9) the benefits are minor and this can be due to the fact that OOK wavelengths are only 33% of the available resources and thus, the network resembles one that has only xPSK wavelengths and no XPM noise. In the last scenario (as shown in Fig. 10) where any wavelength supports any data rate the conventional shortest length path and minimum hop routing schemes seem to scale better than MV-FW scheme. This is could be interpreted by the fact that a network with fully tunable transponders provides greater flexibility in finding an available wavelength for a specific route and subsequently the blocking probability is lower than the previous scenarios.

Finally, it is also shown that the MV-FP scheme is the most reliable in terms of performance. This can be attributed to having a "first shortest route then last-fit wavelength" for 10 Gbps lightpaths combined with a good impairment aware strategy for 40-100Gbps lightpaths which leads to a more efficient provisioning of the connections.

V. CONCLUSION

In this paper, two dynamic PI-Aware RWA schemes for MLR optical networks were presented and compared. A modified Dijkstra algorithm was introduced for 40-100 Gbps lightpaths that mitigates the XPM impairment by adjacent OOK channels and outperforms conventional shortest path and minimum hop routing schemes. It is shown that, in the case of a MLR optical network, QoT based provisioning of the lightpaths can have a strong impact on the network's performance. For future work, the proposed schemes can be extended to include more types of impairment as well as different scenarios of operation such as dynamic power management and implementation of 3R regeneration.

REFERENCES

- [1] A. Nag, M. Tornatore, and B. Mukherjee, "Optical network design with mixed line rates and multiple modulation formats," *J. Lightwave Technology*, vol.28, no.4, pp.466-475, Feb. 2010.
- [2] M. Batayneh, D. A. Schupke, M. Hoffmann, A. Kirstaedter, and B. Mukherjee, "Optical network design for a multiline-rate carrier-grade ethernet under transmission-range constraints," *J. Lightwave Technology*, vol.26, no. 1, pp.121-130, Jan. 2008.
- [3] P. Chowdhury, M. Tornatore, A. Nag, E. Ip, T. Wang and B. Mukherjee, "On the design of energy-efficient mixed-line-rate (MLR) optical networks," *J. Lightwave Technology*, vol.30, no.1, pp.130-139, Jan. 2012.
- [4] T. Wuth, M.W. Chbat and V.F. Kamalov, "Multi-rate (10G/40G/100G) transport over deployed optical networks," *Optical Fiber Communication / National Fiber Optic Engineers Conf. 2008*, (OFC 2008/NFOEC 2008), San Diego, USA, no.NTuB3, Feb. 2008.
- [5] J.-P. Faure, B. Lavigne, C. Bresson, O. Bertran-Pardo, A. C. Colomer, and R. Canto, "40G and 100G deployment on 10G infrastructure: market overview and trends, coherent versus conventional technology," *Optical Fiber Communication / National Fiber Optic Engineers Conf. 2010* (OFC 2010/NFOEC 2010), San Diego, USA, no.OThE3, March 2010.
- [6] T. J. Xia, et al, "Multi-rate (111-Gb/s, 2x43-Gb/s, and 8x10.7-Gb/s) transmission at 50- GHz channel spacing over 1040-km field-deployed fiber," *34th European Conf. Optical Communication*, Brussels, Belgium, no.Th.2.E.2, Sept. 2008.
- [7] G. Agrawal, *Fiber-Optic Communication Systems*, 4th Ed., John Wiley & Sons, Hoboken, New Jersey, USA, 2010.
- [8] K. Christodouloupolos, K. Manousakis and Emmanouel Varvarigos, "Reach adapting algorithms for mixed line rate WDM transport networks," *J. Lightwave Technology*, vol.29, no.21, pp.3350-3363, Nov. 2011.
- [9] N. Sambo, M. Secondini, F. Cugini, G. Bottari, P. Iovanna, "Modeling and distributed provisioning in 10-40-100-Gb/s multirate wavelength switched optical networks," *J. Lightwave Technology*, vol.29, no.9, pp.1248-1257, May 2011.
- [10] A. Bononi and M. Bertolini, "Cross-phase modulation induced by OOK channels on higher-rate DQPSK and coherent QPSK channels," *J. Lightwave Technology*, vol.27, no.18, pp.3974-3983, Sept. 2009.
- [11] F. Idzikowski, "Power consumption of network elements in IP over WDM networks," *Telecommun. Netw. Group (TKN)*, TU Berlin, Berlin, Germany, TKN Tech. Rep. TKN-09-006, July 2009.



Filippos Balasis (B.E 2010) received his B.E. in electrical engineering and computer engineering from National Technical University of Athens, Greece, in 2010. Currently, he is a Master student in Global Information and Telecommunication Studies, Waseda University, Tokyo, Japan. His study emphasizes on physical impairment aware RWA schemes in translucent WDM optical networks. After fulfilling his military service he worked as an engineer in OTE,

Greece's largest telecommunications provider, and he was part of the team responsible for the management and expansion of the company's access network. Mr. Balasis is a student member of IEICE.



Xin Wang (B.S. 2002-M.S. 2006) received the B.S. in computer science and engineering from Dalian University of Technology, Dalian, P.R.China, in 2002 and M.S. degree in computer science from Paris-sud 11 University, Paris, France, in 2006. Currently, he is a Ph.D student in Global Information and Telecommunication Studies, Waseda University, Tokyo, Japan. His research interests focus on planning and control issue in wavelength switched optical networks.

He received the IEICE ICM English Session Award and IEICE Young Researcher's Award in 2012. Mr. Wang is a student member of IEICE.

Sugang Xu (B.E. 1994-M.E. 1997-Ph.D. 2002) received his B.E. and M.E. degrees in computer engineering from Beijing Polytechnic University, Beijing,



China, in 1994 and 1997, respectively, and Ph.D. degree in information and communication engineering at the University of Tokyo, Tokyo, Japan, in 2002. He joined the Global Information and Telecommunication Institute (GITI), Waseda University in 2002, as a research associate. Since 2005, he joined National Institute of Information and Communications Technology (NICT), Japan, as an expert researcher. He is also a visiting researcher in GITI. His research interests include algorithms, network architectures, photonic network control, optical grid network systems, parallel and distributed processing. Dr. Xu is a member of IEEE and IEICE.



Yoshiaki Tanaka (B.E. 1974-M.E. 1976-Ph.D. 1979) received the B.E., M.E., and D.E. degrees in electrical engineering from the University of Tokyo, Tokyo, Japan, in 1974, 1976, and 1979, respectively. He became a staff at the Department of Electrical Engineering, the University of Tokyo, in 1979, and has been engaged in teaching and researching in the fields of telecommunication networks, switching systems, and network security. He was a guest professor at the Department of Communication Systems, Lund Institute of Technology, Sweden, from 1986 to 1987. He was also a visiting researcher at the Institute for Posts and Telecommunications Policy, from 1988 to 1991, and at the Institute for Monetary and Economic Studies, Bank of Japan, from 1994 to 1996. He is presently a professor at Global Information and Telecommunication Institute, Waseda University, and a visiting professor at National Institute of Informatics. He received the IEEE Outstanding Student Award in 1977, the Niwa Memorial Prize in 1980, the IEICE Achievements Award in 1980, the Okawa Publication Prize in 1994, the TAF Telecom System Technology Award in 1995 and in 2006, the IEICE Information Network Research Award in 1996, in 2001, in 2004, and in 2006, the IEICE Communications Society Activity Testimonial in 1997 and in 1998, the IEICE Switching System Research Award in 2001, the IEICE Best Paper Award in 2005, the IEICE Network System Research Award in 2006 and in 2008, the IEICE Communications Society Activity Award in 2008, the Commendation by Minister for Internal Affairs and Communications in 2009, the APNOMS Best Paper Award in 2009, and in 2012, and the IEICE Distinguished Achievement and Contributions Award in 2013. Professor Tanaka is a Fellow of IEICE.

Intelligent Packaging and Intelligent Medicine Box for Medication Management towards the Internet-of-Things

Zhibo Pang*, Junzhe Tian**, Qiang Chen**

*Corporate Research, ABB AB, Västerås, Sweden

** ICT School, Royal Institute of Technology (KTH), Stockholm, Sweden

pang.zhibo@se.abb.com, {junzhe, qiangch}@kth.se

Abstract—The medication noncompliance problem has caused serious threat to public health as well as huge financial waste would wide. The emerging pervasive healthcare enabled by the Internet-of-Things offers promising solutions. In addition, an in-home healthcare station (IHHS) is needed to meet the rapidly increasing demands for daily monitoring and on-site diagnosis and prognosis. In this paper, a pervasive and preventive medication management solution is proposed based on intelligent and interactive packaging (I2Pack) and intelligent medicine box (iMedBox). The intelligent pharmaceutical packaging is sealed by the Controlled Delamination Material (CDM) and controlled by wireless communication. Various vital parameters can also be collected by wearable biomedical sensors through the wireless link. On-site diagnosis and prognosis of these vital parameters are supported by the high performance architecture. Additionally, friendly user interface is emphasized to ease the operation for the elderly, disabled, and patients. A prototyping system of the I2Pack and iMedBox is implemented and verified by field trials.

Index Terms—Medication Management; Internet-of-Things (IoT); In-Home Healthcare Station (IHHS); Wireless Sensor Network (WSN); Controlled Delamination Material (CDM); Radio Frequency Identification (RFID);

I. INTRODUCTION

PERVASIVE healthcare has been recognized to be the next generation form of healthcare, and distributed, patient-centric and self-managed care is emphasized as an alternative to the traditional hospitalized, staff-centric and professional-managed care [1]. Pervasive healthcare based on the emerging technologies of the Internet-of-Things (IoT), as so-called Health-IoT, is highlighted as one of the killer applications of the IoT [18, 21]. Many projects and initiatives

have been devoted in this promising area. Unfortunately, the concern to prescription medication noncompliance, a basic type of self-managed care, is insufficient in the existing research [2]. A frequently cited fact is: medication noncompliance costs the United States healthcare system up to \$100 billion per year, and it is the cause of approximately 11% of US annual hospitalizations [3]. It has been proven that, for the 4 most drug-spending chronic conditions (diabetes, hypertension, hypercholesterolemia, and congestive heart failure), hospitalization rates are significantly lower for patients with higher medication compliance [4]. More startling figures are listed in a report from the National Council on Patient Information and Education (NCPIE) in 2007 [5]: only about 50% of American patients take their medicines as prescribed, resulting in approximately \$177 billion direct and indirect costs to the U.S. economy annually.

To address the medication noncompliance problem, one solution from traditional packaging industry is the One Dose Packaging [6] which packetizes the tablets or capsules of one dosage into one small box of bag. It just makes medication more convenient for patients, but neither improves the compliance nor prevents from noncompliance. Noncompliance detecting and recording capability is offered by the Smart Medical Refrigerator in [7], the microchip powered tablet package in [8] and the Smart Dose Reminder in [9]. But these are mainly afterward checking measure instead of preventive measure, and the operations of these solutions are so complicated that they are only usable for trained caregivers instead of the elderly, disabled, and patients.

At the same time, the increasing demands of daily monitoring prompt the Health-IoT solution to integrate more sensing and data processing capacities especially for on-site diagnosis and prognosis. For example, tri-axis accelerometer, electrocardiogram (ECG), blood pressure, blood oxygen saturation (SpO₂), respiration oxygen saturation, blood sugar concentration, body temperature can be monitored on 24/7 basis [10-14]. So a powerful in-home terminal is needed not only to address the medication noncompliance but also to be used as a generic in-home healthcare station (IHHS) in everyone's home.

In this paper, extending our previous works in [16-21], an in-home medication management and healthcare system is

Manuscript received July 29, 2013. This work was supported in part by the VINN Excellence Center of iPack at the Royal Institute of Technology.

Zhibo Pang is with ABB AB, Corporate Research, Forskargränd 7, 72178, Västerås, Västmanland, Sweden (phone: +46-21 325104; fax: +46-21 323212; e-mail: pang.zhibo@se.abb.com).

Junzhe Tian and Qiang Chen are with Royal Institute of Technology, Department of Electronic Systems, Isafjordsgatan 39, 16440, Kista, Sweden. (e-mail: {junzhe, qiangch}@kth.se).

proposed based on intelligent and interactive packaging (I2Pack) and intelligent medicine box (iMedBox). Preventive medication management is enabled by the intelligent pharmaceutical packaging which is sealed by Controlled Delamination Material (CDM) and controlled by wireless communication. Various vital parameters can also be collected by wearable biomedical sensors through the wireless link. On-site diagnosis and prognosis of these vital signals are supported by the powerful architecture. Additionally, friendly user interface is emphasized to ease the operations especially for the elderly, disabled and patients. A prototyping system is implemented and verified by field trials.

The rest of this paper is organized as follows. The vision of Health-IoT and related concepts are introduced in section II. The system functionality and architecture are given in section III. Implementation and experimental results of the I2Pack and iMedBox are presented in section IV and V respectively. Section V concludes the paper and discusses open issues.

II. THE VISION

A. The Health-IoT

The in-home healthcare (IHH) service enabled by the IoT technology (the so-called Health-IoT) is promising for both traditional healthcare industry and the ICT industry. The Health-IoT service is ubiquitous and personalized and will speed up the transformation of healthcare from career-centric to patient-centric. Typically, a Health-IoT solution includes the following functions:

Tracking and monitoring. Powered by the ubiquitous identification, sensing, and communication capacity, all the objects (people, equipment, medicine, etc.) can be tracked and monitored by wearable WSN devices on a 24/7 basis.

Remote service. Healthcare and assist living services e.g. emergency detection and first aid, stroke habitation and training, dietary and medication management, telemedicine and remote diagnosis, health social networking etc. can be delivered remotely through the internet and field devices.

Information management. Enabled by the global connectivity of the IoT, all the healthcare information (logistics, diagnosis, therapy, recovery, medication, management, finance, and even daily activity) can be collected, managed, and utilized throughout the entire value chain.

Cross-organization integration. The hospital information systems (HISs) are extended to patient' home, and can be integrated into larger scale healthcare system that may cover a community, city or even state.

B. Application Scenario

A typical application scenario of the Health-IoT system is illustrated in Figure 1. The center of the system is a powerful intelligent medicine box (iMedBox), which works not only as a traditional in-home medicine container (such as a drawer of cabinet, a thermostat or an icebox), but also as a "medication inspector", and an "on-site examiner" in daily monitoring. On

one side, it is linked to public area (e.g. the hospital, the medicine supply chain and the emergency help center) through wireless internet. On the other side, it controls a suit of intelligent pharmaceutical packages (iPackage) and a suit of wearable biomedical sensor tags (iTag) through radio frequency identification (RFID) links and wireless biomedical sensor network (WBSN) respectively. More information is available in our previous work [16-21].

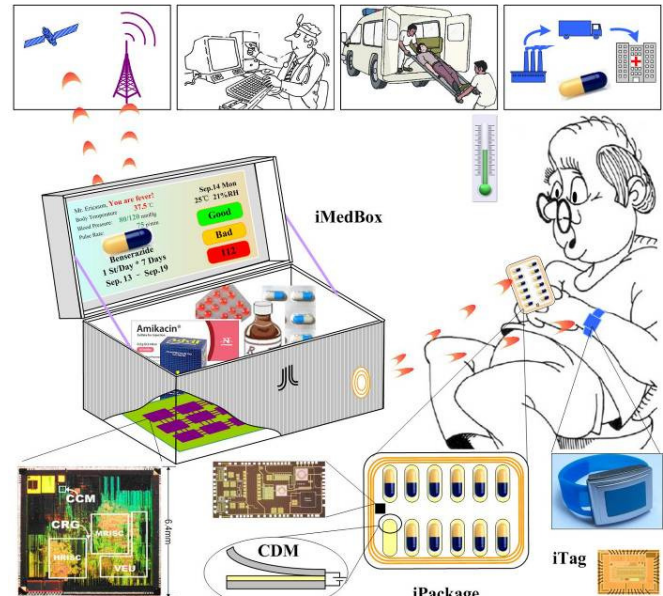


Figure 1 Application Scenario

C. Intelligent and Interactive Packaging

"Ubiquitous" is the distinct feature of IoT technologies. Ideally, it should be able to reach every item of the objects. The Health-IoT system should be able to track every package of medicine, record the medication activity of every tablet of capsule, and present all prescription information related to the patient. To realize this feature, a suitable format of a smart device is demanded. It should be able to carry the capacities and benefits of IoT with affordable cost and in a natural manner. According to the vision of iPack VINN Excellence Center [22], the Intelligent and Interactive Packaging (I2Pack) is a suitable format of smart device for this purpose.

As shown in Figure 2 [22], the I2Pack is the next generation of packaging which can interact with customers by integrating RFID, sensing, energy harvesting, communication, display, acting and other functions onto traditional packaging. When paper-based actuators and display are integrated, the packaging can not only be aware of the presence of customers, but also be able to inform the customer what's on.

The vision of I2Pack may make big transformations to the business world. The information carried by the packaging will transform from static to dynamic, the flow of information will transform from single-directional (product-to-consumer only) to dual-directional (both product-to-consumer and consumer-to-product), and the role of packaging will transform

from “passive” (only controlled by consumer) to “active” (self-controlled or remotely controlled). So the I2Pack can be assigned more responsibilities in addition to the containing and protecting of goods. The role of packing becomes “communication medium” between suppliers and consumers. It is expected to be a seller on-site, an information presenter, an information collector, and even an executor of particular operations. For example, in the retailing application scenario, the I2Pack with a touch sensor knows who has touched it, and if integrated with a price tag, it can inform the customer “today’s special offer”. In the Food-IoT application scenario, it can inform customer the quality and freshness of the food automatically. In the Health-IoT application scenario, an intelligent pharmaceutical packaging glued can be electrically opened through finger touch. [22]

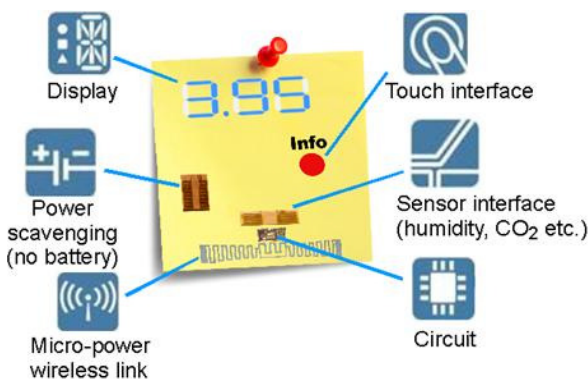


Figure 2 The vision of the intelligent and interactive packaging [22]

Intelligent pharmaceutical packaging is one of the typical implementations of the vision of I2Pack (see section III). It has offered a technical solution to achieve the so-called preventive medication management.

D. Intelligent and Preventive Medication Management

Comparing to the existing solutions, preventive medication management has been suggested to be more effective to address medication noncompliance problem [5]. Preventive medication management requires real-time reminding, recording, preventing of the medication activity, on-site diagnosis and prognosis of vital parameters, and emergency supporting to the users. In particular, it includes the following functionalities.

Medicine Inventory: The iMedBox can register, record, query and statistic all medicine utilities automatically by reading the RFID tags on them.

Medication Reminding: The iMedBox can download and parse the prescription automatically and remind the patient to take the medicine on time e.g. by flashing on the screen, playing music via the speakers, flashing the lights, etc.

Noncompliance Recording: All of the patient’s medication activities (e.g. opening the box, taking a dose, forgetting to take a dose, destroying some medicines by mistake, throwing some medicines away, etc.) are detected and recorded.

Noncompliance Preventing: Without an “OPEN” command from the iMedBox according to the prescription, the

user/patient cannot by hand open the iPackage which is sealed tightly by the CDM films. Thus early or excessive medication can be completely prevented.

III. SYSTEM ARCHITECTURE

A. System Architecture Diagram

As shown in Figure 3, multiple wireless links are integrated in the iMedBox. User friendly user interfaces are provided including a LCD displayer, a touch screen, a camera, speakers, a microphone, shining LED lamps, and vibrators.

Wireless internet link: includes WiFi and/or GPRS/3G communication stacks, system security, data base access, web server for data shearing.

Global Positioning System (GPS) link: is useful to deliver emergency supporting to the right location at the first moment.

WBSN link: includes stacks for star-topology networking and data collection.

RFID link: includes medicine inventory management, CDM controlling and medication compliance detection.

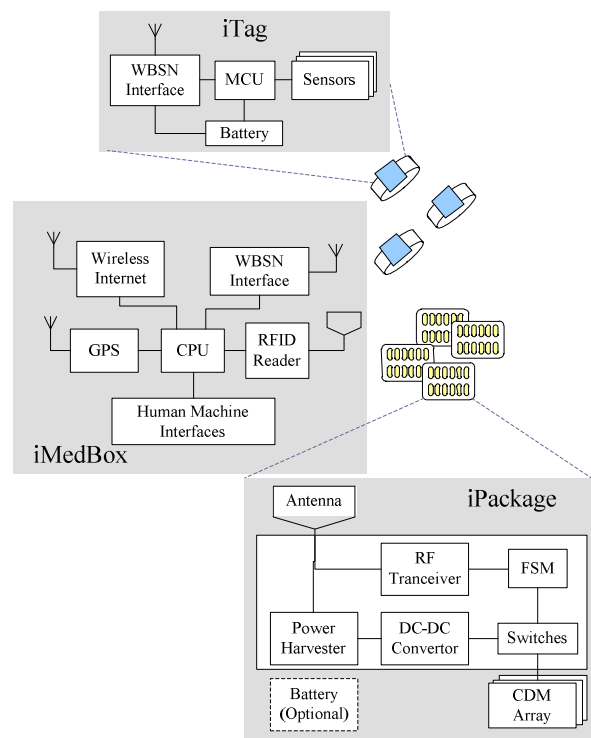


Figure 3 System Architecture

In the iPackage, a significant difference comparing to traditional RFID-enabled packages is, an array of CDM films and corresponding control circuits are added. The CDM film is a 3-layer foil composed of an aluminum bottom layer, an aluminum top layer and an adhesive middle layer made of electrochemical epoxy. When the voltage subjected between the bottom layer and top layer is higher than a particular threshold called Delamination Voltage (V_d), the electrochemical reaction is triggered in the middle layer. If the voltage maintains longer than a particular time called Delamination Time (T_d), the epoxy

layer is destroyed and thus the top layer bottom layer are separated. V_d and T_d are both distinct parameters determined by the formula and processing when the material is manufactured [15].

The distinct characteristics of the CDM are used to perform noncompliance preventing function of the intelligent pharmaceutical packaging. The iPackage which is sealed with a CDM film can be opened by the iMedBox by sending an OPEN command to the microchip in the iPackage. And it cannot be opened by the patient without the OPEN command since the adhesive glue of CDM is too tight to human's hands. For each tablet or capsule, there is one dedicated piece of CDM which is controlled separately. In other words, each tablet or capsule can be controlled by the iMedBox. So the compliance of prescription is achieved at tablet level.

The energy needed to open the CDM can be transmitted by wirelessly by near field magnetic resonance, so the intelligent pharmaceutical is still battery-less. Or as an alternative, a printed battery could be manufactured along with the package to make a self-powered packaging solution. This has been proven by experimental results in the next sections. Both the battery-less and battery-power solutions will have similar out-looking to the traditional ones

The iTag has a typical architecture of WBSN. It comprises a WBSN interface, a low power MCU, a suit of biomedical sensors and a battery. The battery-powered WBSN device has significant advantages in communication distance and sensing capacity comparing to the battery-less and self-powered ones.

B. On-site Diagnosis Framework

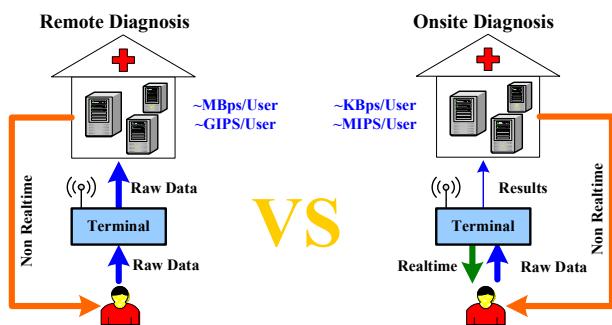


Figure 4 On-site diagnosis vs. remote diagnosis

There are mainly two kinds of frameworks in pervasive healthcare systems (Figure 4). In Remote Diagnosis Framework, the raw data collected by on-site terminal is transmitted directly to the server and a non-real-time and long term feedback is given to the user according to analysis results. Contrary, in On-site Diagnosis Framework, preprocessing is performed in the on-site terminal and only results (instead of raw data) are transmitted to the server. In this way, both the traffic load between terminal and server and the computation load in the server are reduced significantly. This makes the latter solution more effective and efficient, because the data transmission and processing in Remote Diagnosis Framework would overwhelm the communication system and resources in server when it is widely adopted. Furthermore, the on-site terminal could give

users feedback at first time and first place, which is very important for some urgent situations such as acute myocardial infarction.

So we adopt the On-site Diagnosis Framework to design the proposed system. In iMedBox, a suit of basic diagnosis and prognosis examinations can be performed in the software. Feasible algorithms are becoming available during the efforts in many research activities, e.g. human movement classification and detection based on tri-axial acceleration, ECG signal compression based on discrete wavelet transformation, heart premature detection based on ECG signal classification [11-14].

IV. IMPLEMENTATION OF THE INTELLIGENT PACKAGING

A. Prototype of the CDM

To analyze and evaluate the CDM material for iPackage, we made a dedicated demonstration board including a near-field resonance coil, a resonance driver chip, an MCU, two button batteries, a DC-DC converter, a power switch and a piece of CDM film (Figure 5). In this step, the main power source is the button batteries and the near-field resonance coil is just for control commands. The DC-DC converter multiplies 3V battery voltage to 30V to the CDM if an OPEN command is received from the coil. More information is available in our previous work [17].

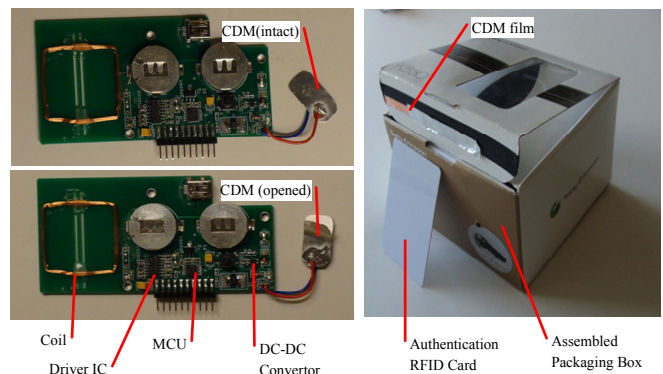


Figure 5 Prototypes of CDM (left) and assembled intelligent package (right)

B. Setup of experiments for CDM characterization

The main task of CDM characterization is to evaluate the energy and power needed to open a unit area of CDM film, where the Delamination Voltage (V_d), Delamination Maximum Current (I_d), Delamination Time (T_d), Delamination Power (P_d) and Energy expense (E_d) are measured and calculated.

As mentioned in the previous study [15], CDM will quickly open if it is added a voltage in 10-50V range, and if some environment conditions affect CDM electrochemical characteristics. The following tests are performed at a temperature round 22°-25° and a relative humidity of 30%-37%, within the safety range of 36V for human. To formalize the test results, the size of test CDM pieces is set to 1cm² because the size of film is almost unrelated with opening time [15]. During the whole delamination period, current through the CDM film is measured by a 180 Ohm serial resistor.

C. Delamination Behavior

To monitor the delamination behavior of CDM, we apply a 30V DC power source to a 1cm² CDM film. As shown in Figure 10, in the beginning, the current reaches its maximum value 0.95 mA/cm² (I_d) in a few seconds. When holding power source voltage for about ten seconds, the current drops down significantly. After 90 seconds, the current is reduced by over 90%, and the diminution turns to slow. At this moment, the CDM film is so weak that just a slight tough can make it peel off. But as we can see in the last 60 seconds, without any external force, the current through the material is very small which is infinitely close to zero but never equal to zero.

In order to standardize the delamination behavior, a static shear force is added to one surface of the CDM film by hanging a mall weight. When the adhesive strength cannot afford the weight, the CDM film is disbanded immediately. The current at that moment is called Turnoff Current which signifies the material is delaminated. And T_d is defined as the interval from power supply is applied on the surface till the current reaches the Turnoff Current in a current curve.

D. Impact of Power Source Duty Cycle

Four duty cycles of a 100 KHz and 30V power source are applied to a 1cm² CDM film respectively. When duty cycle of power source increases from 20% to 100%, the T_d decreases disproportionately (Figure 6).

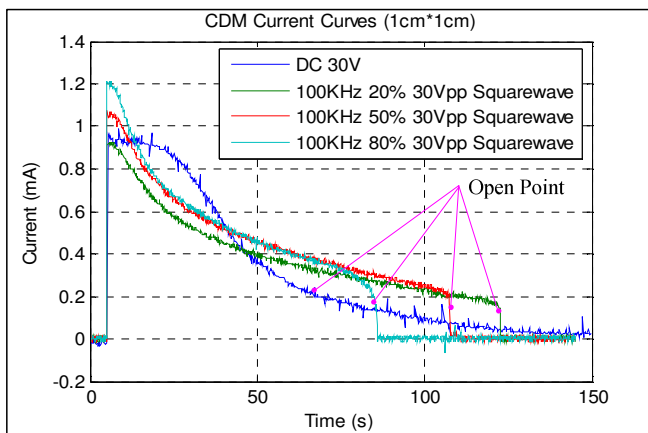


Figure 6 Impact of Power Source Duty Cycle

E. Impact of Power Source Voltage

The current through the material under different power source voltages from 5V DC up to 30V DC are plotted in Figure 6. When the power supply is lower than 5V, the CDM will not open within 2 minutes without any large external shear force. When the voltage increases from 5V to 30V, the T_d decreases significantly and disproportionately.

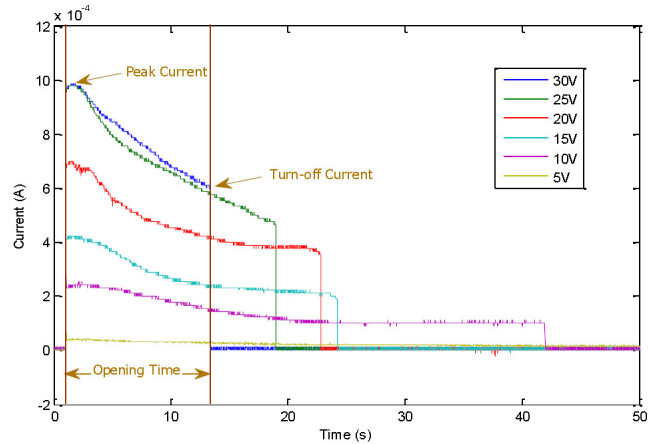


Figure 7 Impact of Power Source Voltage

F. Impact of Material Process Variety

For CDM pieces at different position from the same reel, the difference of T_d is negligidible. But the difference between pieces from different reels is larger according to measurement results of 4 pieces from 4 different reels in Figure 7. The main reason is that the difference in the material process and quality from reel to reel is larger than that from region to region in one reel.

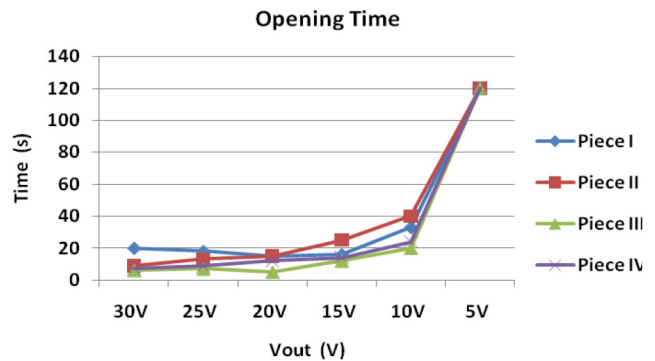


Figure 8 Impact of Material Process Variety

G. Summary of the CDM Characterization

From the results described above, we can make the following conclusions:

- 1) I_d is at the order of 1mA/cm²
- 2) V_d is at the order of 30V
- 3) T_d is at the order of 100s
- 4) P_d is at the order of 30mW/cm² (=1mA/cm²*30V)
- 5) E_d is at the order of 3J/cm² (=30mW/cm²*100s)

This implies that a printed thin-film battery with 3.3mAh capacitance is sufficient to open up to 12 tablets sealed with 1cm² CDM film for each. This is a typical application case in practical tablet packages. But one important factor should be taken into considerations: most of printed batteries have a large internal resistance which will decrease the peak current and prolong the T_d . So, it is feasible to use the CDM material to realize the proposed intelligent package.

H. Battery-less Intelligent Pharmaceutical Packaging

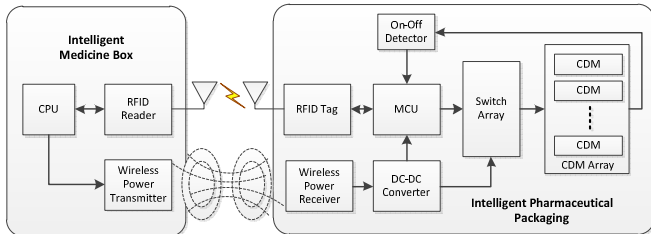


Figure 9 Battery-less intelligent pharmaceutical packaging based on wireless power transmission

Currently the prototype is power by two icon batteries which is not environment friendly. A battery-less solution is more suitable for the intelligent pharmaceutical packaging. As shown in Figure 9, a battery less intelligent pharmaceutical packaging is proposed based on the wireless power transmission technology (WPT). The WPT is already in mass-production in consumer electronic products, e.g. Nokia Lumia 920 mobile phone, with affordable cost and sufficient maturity. According to the results of CDM characterization, today’s wireless power transmission technology is sufficient to provide this energy. For example, the single chip wireless power receiver IDTP9020 from Integrated Device Technology, Inc. can output up to 5W@5V conforming to the Wireless Power Consortium (WPC) “Qi” specification. It is sufficient to drive a CDM array in the pharmaceutical packaging.

V. IMPLEMENTATION OF INTELLIGENT MEDICINE BOX

A. iMedBox Prototype

As shown in Figure 10, the 3rd generation of the iMedBox prototyping system is implemented based on Samsung Galaxy Tab10.1 tablet PC. The processor is Tegra 2 dual-core ARM Cortex-A9 at the speed of 1GHz and manufactured by NVIDIA. It has 16GB internal flash memory and could be extended by MicroSD card up to 32GB. It also has internal 2.0MP front-camera, Wi-Fi/Bluetooth/3G access module, 6860mAh battery, and USB connection. To support different port types of WSN, a connection bridge based on FTDI Vinculum II programmable USB Host/Slave controller is also implemented. The connection bridge support UART, SPI Master, SPI Slave, and USB Host/Slave connection.

The tablet is embedded in the lid of the medicine box. And the connection bridge together with plug-in modules is placed in the bottom of the box. In the prototype, the connection bridge is implemented with four adapter nodes. Each adapter node is implemented with a VNC2 from Future Technology Devices International Limited development module (Vinculum II), and can provide one USB host port, one USB slave port, one SPI master port, one SPI slave port, and one high speed UART port. Four nodes are connected with SPI port as a chain. The first node is connected to the tablet via USB port with the table in slave mode. The Android Open Accessory Protocol of Android OS ensures the Vinculum II can be recognized and accessed by the tablet without extra driver.

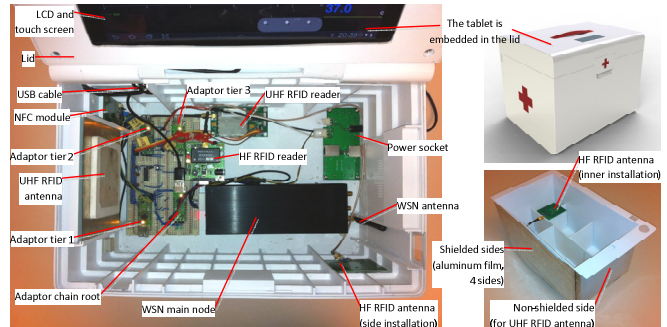


Figure 10 Hardware of the 3rd generation of iMedBox prototype

With the Vinculum II chips, the USB port of the tablet is remapped to four UART ports. One of the ports is connected to a main node receiving wireless sensor signals. One is connected to a RFID reader which monitors the status of the tags on the medicine package. The prototyping system also has a built-in NFC reader. Take the advantage of the peer to peer communication capability of NFC, the NFC reader can be another interface for the iMedBox to communicate with biomedical devices and authentication cards. One extra UART is left for future extension.

B. Software and User Interface

The tablet is running Android 3.1 Honeycomb open source mobile operating system released by Google under Apache license. It is also capable to upgrade the system to Android 4.0 Ice Cream Sandwich or higher.

The demonstration software is called *iMedBox – Pervasive Healthcare Station*. The software contains seven modules: core activity, screen subsystem, database, USB controller, net controller, alarm service and setting & configure subsystem. The basic unit of the user interface of this iMedBox application is tab. Users can add or remove tabs to customize the user interface, and switch between each tab by swapping on the screen. The screen subsystem support for displaying tab pages of two basic types: the Chart Tab and Table Tab. The Chart Tab content is rendered by a third party engine called AChartEngine. The Table Tab is rendered by the build-in List View element. Both the Chart tab and the Table Tab are designed to be customized easily for a specified application. One customized tab is called medicine tab.

There are two predefined tabs, a Chart Tab called “Signal View” (Figure 11a) for real-time monitoring of biomedical signals (e.g. ECG, body temperature, blood pressure, etc.), and a Table Tab called “Medication View” (Figure 11b) for medication management application.

The Signal View shows the waveforms of signals e.g. ECG. The chart can live update with the input ECG data packets. It can also show some extra summarized results like the heart beat rate and body temperature. The Medication View shows the medicine taken schedule for the user, contains the history and the following plan. User can enable the alarming service of this tab. Then if the next time is up to take a dose of medicine, the tablet will wake up automatically, play a piece of alarm music,

and show the medicine information for user to take.

When the alarm is triggered, the connected RFID reader starts to detect the status of a specified tag. The tag ID has mapped to the medicine which needs to be taken at the moment. When the user picks up the right medicine, the alarm will stop automatically and the alarm for the next medicine is set, but the screen keeps showing a warning message. When the user finishes taking the medicine and puts the bottle back, the warning message will go away. Each successful medication procedure will be marked with a happy face.

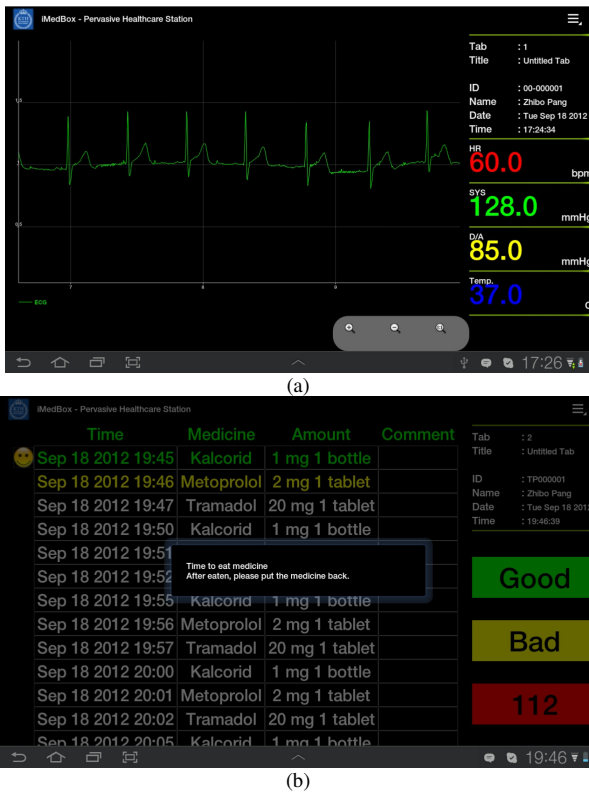


Figure 11 User interfaces of the iMedBox software for (a) Signal View, and (b) Medication View.

Additionally, there is one reserved tab called “Home Tab” which is a welcome page showing some general information like current time, a tab list, an icon for switching to chatting application (e.g. Skype), and a note area for displaying customized messages.

C. Medication Database

The primary entities (tables) of the Medication Database (MDB) and relations among them are shown in Figure 12a where all prescription and medication information is well organized. Correctly handling of the DoseList table in MDB is the core of the database system. Firstly, when a new prescription is issued in hospital, corresponding records are added in by dispatching one prescription into multiple dose lists. Secondly, when user opens the iMedBox, a timely dose list that should be taken today is retrieved. Thirdly, medications records will be updated to the MDB no matter if the doses are taken correctly or not. Example procedure and codes in Structured Query

Language (SQL) are shown in Figure 12b.

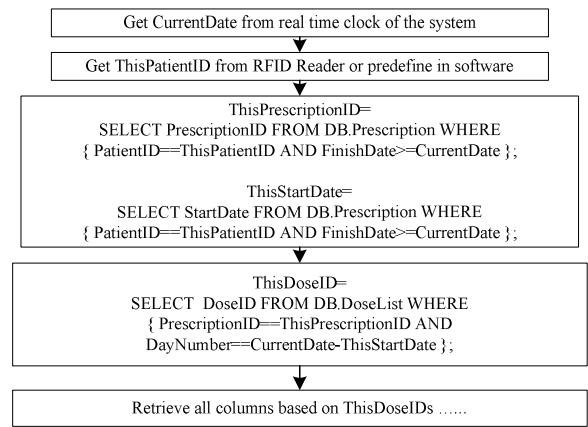
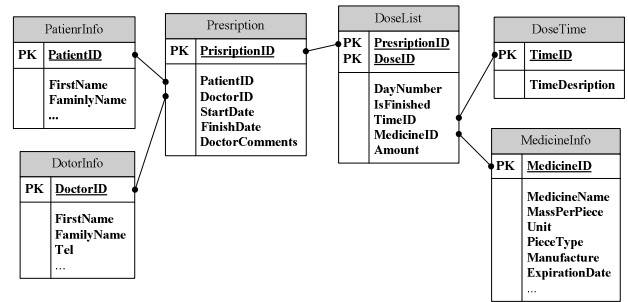


Figure 12 The Medication Database (a) tables and keys, and (b) procedure of query

D. Service Backend

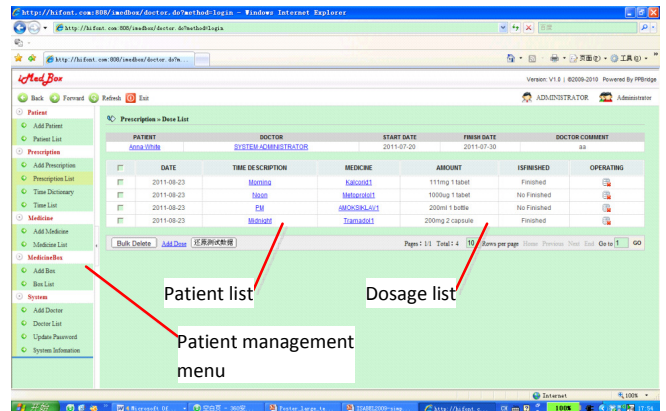


Figure 13 Web interface for doctors to manage the medication information

A demonstrative backend system has been implemented. A web-based server as well as databases are implemented by Java and deployed on an Apache Tomcat web server. Professional management interfaces are implemented as web page (Figure 13), such as prescription management, case history management, and remote diagnosis. The iMedBox can connect to the backend system via either 3G modem or WiFi.

E. Demonstration and field trials

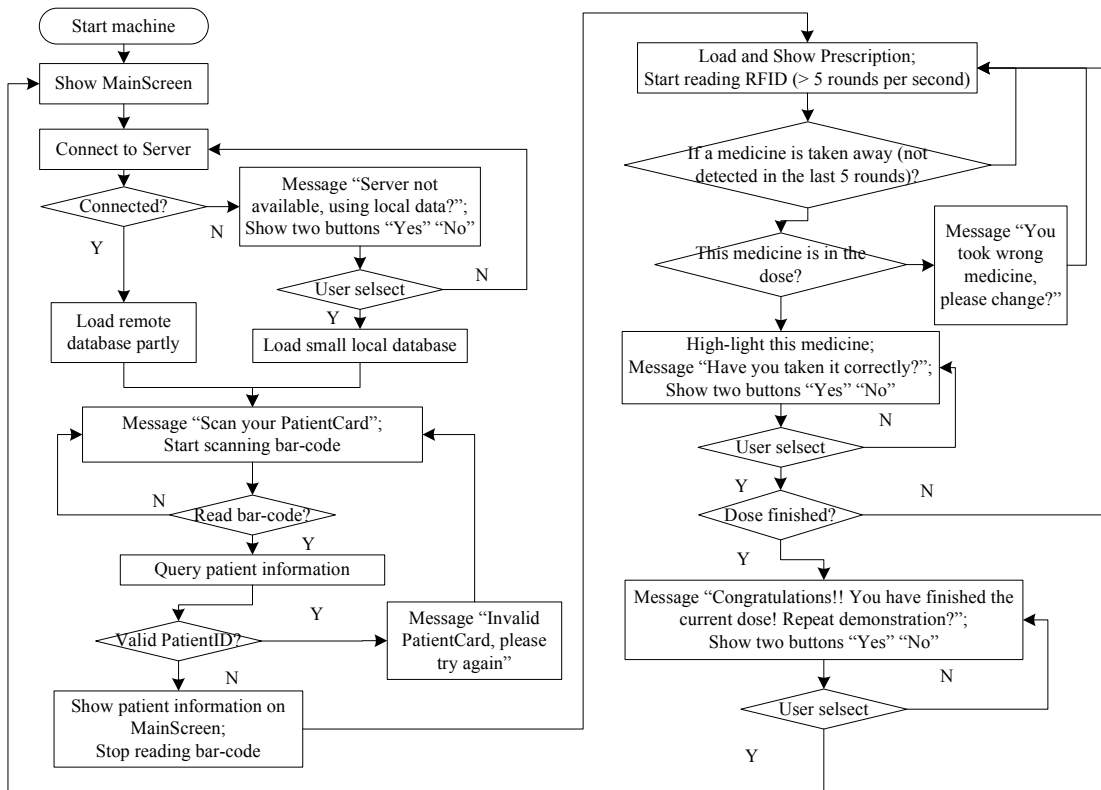


Figure 14 Flow chart of the demonstration

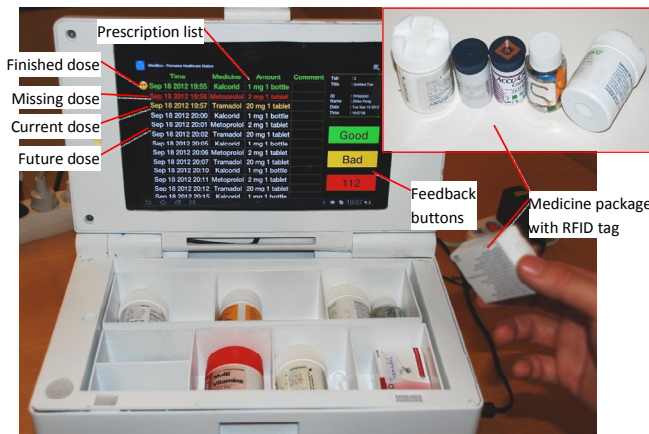


Figure 15 Demonstration of the iMedBox for medication management application

Field trials for the medication management services have been carried out with Blekinge Center of Competence (BCC), County Council of Blekinge, Sweden [18]. The scenario is shown in Figure 14 and the flow chart in Figure 15. The iMedBox prototype were demonstrated to patients, relatives that take care of patients, elder people, and healthcare personal. Three different groups have been chosen:

(1) A sheltered housing “Vidablicks” in the city of Ronneby. We demonstrated to a group of nurses that have meeting every second months to share their experiences in the field of dementia care.

(2) Healthcare staffs at Valjeviken’s rehabilitation center. We met the healthcare staffs including medicine doctors, nurses,

undersköterskor, arbetsterapeuter, sjukgymnaster and kuratorer to get the detailed information about the benefits and consequences of using iMedBox.

(3) Staff and caretakers at an elderly living in Karlskrona “Fregatten”. We discussed the acceptances of different kind of assisting equipment to remind medicine time or to make it easier to take the right amount.

The concepts and ideas proposed in this paper have been confirmed by positive feedback. All audience agree that the medication reminding and recording functions can significantly improve the compliance especially for elderly, and even more necessary for the elderly with light dementia symptoms. It is necessary to integrate it to the hospital’s prescription system to reduce the workload.

At the same time, the comments from the audience have indicated directions of improvement in the future. For example,

(1) To add pictures of the drugs and drug packages on the screen.

(2) The iMedBox should be secured with a locking system, making it accessible only by specified user rather than unsuitable person such as the patient with dementia symptom.

(3) To simplify the user interface further and make the texts and colors clearer.

VI. CONCLUSION

In this paper, a pervasive and preventive medication management solution addressing the medication noncompliance problem is proposed. A prototype system is implemented which confirms the feasibility of the presented intelligent

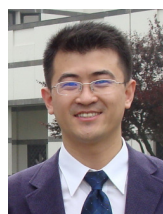
pharmaceutical packaging and intelligent medicine box.

As future work, on-site algorithms will be implemented as well as data collection through WBSN devices. Integrating the CDM film with wireless power transmission and RFID tag onto one flexible substrate is another task. User interfaces and experience will be further improved too.

REFERENCES

- [1] Koop C.E. et al. "Future delivery of health care: Cybercare", *IEEE Engineering in Medicine and Biology Magazine*, Vol27, Iss6, Nov-Dec 2008 P29 – 38
- [2] Carsten Orwat, Andreas Graefe, Timm Faulwasser, "Towards pervasive computing in health care – A literature review", *BMC Medical Informatics and Decision Making*, Jun 2008
- [3] The Task Force for Compliance, "Noncompliance with medications: an economic tragedy with important implications for health care reform", *Baltimore, Md*, 1994:1-39.
- [4] Sokol MC, McGuigan KA, Verbrugge RR, Epstein RS., "Impact of medication adherence on hospitalization risk and healthcare cost." *Med Care*. 2005 Jun;43(6):521-30.
- [5] NCPIE, "Enhancing Prescription Medicine Adherence: A National Action Plan", <http://www.talkaboutrx.org/> Aug.2007
- [6] MTS Medication Technologies, <http://www.mts-mt.com/>
- [7] Paul Kuwik et al., "The Smart Medical Refrigerator", *IEEE POTENTIALS*, Vol24, Iss1, Feb-Mar 2005 P42 - 45
- [8] Cypak AB, <http://www.cypak.com/index.php?p=home>
- [9] Ronald Sekura, Gwen Gampel Paulson, "Using A Patient-Based Information Technology Approach For Solving Prescription Medication Non-Compliance", *Presentation at Information Technology Association of America*
- [10] Carroll R., Clossen R., Schnell M., Simons D., "Continua: An Interoperable Personal Healthcare Ecosystem", *Pervasive Computing*, IEEE, Vol6, Iss4, Oct.-Dec. 2007 P90 – 94
- [11] Fei Hu, Yang Xiao, Qi Hao, "Congestion-aware, loss-resilient bio-monitoring sensor networking for mobile health applications", *IEEE Journal on Selected Areas in Communications*, Vol27, Iss4, May 2009
- [12] Jae Min Kang, Taiwoo Yoo, Hee Chan Kim, "A Wrist-Worn Integrated Health Monitoring Instrument with a Tele-Reporting Device for Telemedicine and Telecare", *IEEE Trans. On Instrumentation And Measurement*, Vol55, No5, Oct 2006
- [13] Al Khatib I. et al., "A multiprocessor system-on-chip for real-time biomedical monitoring and analysis: architectural design space exploration", *ACM/IEEE Design Automation Conference (DAC2006)*
- [14] Dan Istrate et al. "Information Extraction From Sound for Medical Telemonitoring", *IEEE Trans. On Information Technology In Biomedicine*, Vol. 10, No. 2, Apr 2006
- [15] Carl-Ola D., Petronella N., Lars S., "Controlled Delamination of Adhesives within Packaging and Distribution", www.storaenso.com/products/packaging/Documents/cdm_technical.pdf
- [16] Zhibo Pang, Qiang Chen, Lirong Zheng, "A Pervasive and Preventive Healthcare Solution for Medication Noncompliance and Daily Monitoring", *2nd Inte. Symp. on Applied Sciences in Biomedical and Communication Technologies (ISABEL 2009)*, pp1-6, Nov. 2009,
- [17] Jie Gao, Zhibo Pang, Qiang Chen, Lirong Zheng, "Interactive Packaging Solutions Based on RFID Technology and Controlled Delamination Material", *IEEE Int'l Conf. on RFID*, pp158-165, Apr 2010,
- [18] Zhibo Pang, Lirong Zheng, Junzhe Tian, Sharon Kao-Walter, Elena Dubrova, Qiang Chen. "Design of a Terminal Solution for Integration of In-home Healthcare Devices and Services towards the Internet-of-Things", *Enterprise Information Systems*, DOI:10.1080/17517575.2013.776118, April 2013.
- [19] Zhibo Pang, Qiang Chen; Junzhe Tian, Lirong Zheng, Elena Dubrova. "Ecosystem Analysis in the Design of Open Platform-based In-Home Healthcare Terminals towards the Internet-of-Things". *International Conference on Advanced Communications Technology (ICACTION)*. Jan 2013, Pyeongchang, Korea.

- [20] Zhibo Pang, Qiang Chen; Lirong Zheng, Elena Dubrova. "An In-home Medication Management Solution Based on Intelligent Packaging and Ubiquitous Sensing". *International Conference on Advanced Communications Technology (ICACTION)*. Jan 2013, Pyeongchang, Korea.
- [21] Zhibo Pang, "Technologies and Architectures of the Internet-of-Things (IoT) for Health and Well-being", PhD Thesis, Royal Institute of Technology (KTH), Stockholm, Sweden, 2013.
- [22] iPack VINN Excellence Center, (2010). A General Presentation on Ubiquitous Intelligence in Paper and Packaging. [on-line] <http://www.kth.se/ipack> [accessed Dec 1, 2012]



Zhibo Pang received B.Eng. degree in Electronic Engineering from Zhejiang University, Hangzhou, China, in 2002, MBA in Innovation and Growth from University of Turku, Turku, Finland, in 2012, and PhD in Electronic and Computer Systems from the Royal Institute of Technology (KTH), Stockholm, Sweden, in 2013.

He is a research scientist at ABB Corporate Research, Västerås, Sweden. Before joined ABB, he worked as technical manager in semiconductor industry, designing baseband and application processors and turn-key solutions for mobile smart devices. He has 15 patents and over 30 peer-reviewed papers in international journals and conferences. He was awarded the National Great Invention Award by the Ministry of Information Industry of China in 2005, won the First Place Prize of the RFID Nordic EXPO in 2008 and Outstanding Paper Awards in ICACT2013. His current research interests include the Internet-of-Things, wireless sensor network, industrial communication, real time embedded system, enterprise information systems, automation networks, and multicore system-on-chip and network-on-chip. He also works on the business-technology joint research such as business model design, value chain formulation, strategy, and entrepreneurship & intrapreneurship.



Junzhe Tian received B.Eng. degree in Communication Engineering from Beijing University of Posts and Telecommunications (BUPT), Beijing, China, in 2010, M.Sc. degree in System-on-Chip Design from Royal Institute of Technology (KTH), Stockholm, Sweden, in 2013. After graduate, he became a Software developer at Excosoft AB Stockholm, Sweden. Currently he is working on design and implementation of Graphical Editing Framework (GEF) and Document

Type Definition (DTD) in publishing industry.



Qiang Chen received the Ph.D. degree in electronics from Linköping University, Linköping, Sweden, in 1993.

He was with Ericsson Microelectronics, Stockholm, Sweden, from 1994 to 2002 and became an Ericsson Expert in 2001. He joined Infineon Technology Sweden, Stockholm, in 2003 as a Principal. He has been at Royal Institute of Technology, Stockholm, as a Senior Research Fellow and Project Leader with the Department of Electronic Systems since 2008. He is a Senior Research Scientist with the Department of Electronic Systems and iPack VINN Excellence Center, School of Information and Communication Technology, Royal Institute of Technology. He has published more than 40 international reviewed scientific papers. His current research interests include electronic devices and circuits, wireless sensor network and sensor technology, and printed electronics.

Introducing Dual Regularization Parameters into Regularized Channel Inversion (RCI)-Based Vector Perturbation for Modulo Loss Reduction

Yafei Hou, Satoshi Tsukamoto, Kazuto Yano, Masahiro Uno, Kiyoshi Kobayashi

ATR Wave Engineering Laboratories, Kyoto, Japan

2-2-2, Hikaridai, Seika-cho, Souraku-gun, Kyoto, 619-0288, Japan

{yfhou, tsukamoto, kzyano, uno, kobayashi}@atr.jp

Abstract—This paper proposes a method to reduce the symbol error caused by modulo operator for regularized channel inversion (RCI)-based vector perturbation (RCI-VP). The proposed method introduces dual regularization parameters of RCI precoding matrix. First regularization parameter α_1 is set so as to maximize the signal to interference plus noise ratio (SINR) value of each stream to find the optimal perturbation vector. The second regularization parameter α_2 is set so as to minimize the total MSE between the transmitted perturbation vector and received perturbation vector to reduce the symbol error caused by modulo operator. The simulated results confirm that the proposed method can improve the performance of RCI-VP over *i.i.d.* MIMO channel and frequency-selective fading MIMO channel.

Keywords—Vector perturbation, SINR maximization, Modulo loss, Regularization parameter, Minimum mean square error

I. INTRODUCTION

THE technique of multiuser multiple-input multiple-output (MU-MIMO) can be utilized to improve downlink transmission rate of each user in picocell or femtocell systems. For a downlink MU-MIMO system, many spatial division multiple access (SDMA) techniques can be selected to improve the MU-MIMO channel capacity [1]. Among them, linear precoding combined with vector perturbation (VP) [2] is an algorithm to achieve MU-MIMO capacity bound using dirty paper coding (DPC) [3].

VP algorithm includes regularized channel inversion (RCI)-based VP (RCI-VP) [4] and zero-forcing (ZF)-based VP (ZF-VP). RCI-VP utilizes a parameter α for RCI precoding matrix and it is equivalent to ZF-VP if α equals zero. RCI-VP generally outperforms ZF-VP if the α value is appropriately selected. Therefore, finding an efficient regularization parameter α for RCI precoding matrix is a research topic for performance improvement.

The general objective function for finding an optimal α is to maximize the signal to interference plus noise ratio (SINR)

of each stream. However, this optimal value is still an open issue and is only searched with a numerical method [2], [5]. Another objective function for optimizing α is to minimize the total mean square error (MSE) of the transmitted data and received data. To reach the aim, several methods have been proposed such as processing VP with continuous-valued perturbation vector [6] or minimizing the bit-error ratio (BER) of generalized RCI-VP system as the optimization criterion [7]. Several schemes improve the RCI-VP performance by shaping the transmitted symbols with different lattice transformation techniques [8]. Reference [9] showed that finding an optimal α to maximize the SINR value of each stream is equivalent to finding the optimum perturbation vector that minimizes the total MSE of the transmitted data and received data. But the method requires a transformed precoding matrix which needs some high-complexity matrix decomposition processes for searching the optimal perturbation vector.

In this paper, we first show that, using precoding matrix with optimized α based on SINR, the total MSE between the transmitted perturbation vector and received perturbation vector is not generally minimized. In such cases, the modulo operator at receiver sides deteriorates BER performance. In order to improve the performance of RCI-VP, we propose a method using dual regularization parameters of RCI precoding matrix. First, we find the optimal regularization parameter α_1 to maximize the SINR value of each stream by simulation for different modulation to realize the optimal perturbation vector search. Then we find the optimal regularization parameter α_2 to minimize the total MSE between the transmitted perturbation vector and received perturbation vector to reduce the symbol error generated from a modulo operator. The simulated results show that the proposed method can improve the performance of RCI-VP especially for QPSK modulation over *i.i.d.* MIMO channel and frequency-selective fading MIMO channel.

This paper is organized as follows. The RCI-VP algorithm and QR-decomposition M-algorithm encoder (QRDM-E) [10] are briefly described in Section II. Then the conventional RCI-VP with optimized α based on SINR and the proposed method are introduced in Section III. The performance of the proposed method over flat-fading and frequency-selective fading channels is shown in Section IV. Finally Section V gives conclusions.

Manuscript received August 1st, 2013. This work was supported by the Ministry of Internal Affairs and Communications under a grant entitled "Research and development on nonlinear multiuser MIMO technologies." This paper has been partially presented at the 15th international conference on advanced communications technology (ICACT 2013).

The authors are with the ATR Wave Engineering Laboratories, 2-2-2, Hikaridai, Seika-cho, Souraku-gun, Kyoto, 619-0288, Japan. Corresponding author to provide phone: 81-774-95-1574; fax: 81-774-95-1508; e-mail: yfhou@atr.jp

Notation: We use upper (lower) boldface letters to denote matrices (column vectors), sometimes with subscripts to emphasize their sizes. $(\cdot)^*$, $(\cdot)^T$, $(\cdot)^H$ will denote complex conjugate, transpose, conjugate transpose. $\mathbf{E}\{\cdot\}$ and $\text{Tr}\{\cdot\}$ are the expectation operator and matrix trace operator.

II. RCI-BASED VECTOR PERTURBATION (RCI-VP) AND QRDM-ENCODING

A. RCI-based vector perturbation (RCI-VP) algorithm for MU-MIMO

A general model of downlink MU-MIMO system includes a BS with N_t transmitting antennas and K users, each with N_r receiving antennas. We assume that $N_t = KN_r$. The corresponding vector equation is

$$\mathbf{y} = \mathbf{H}\mathbf{u} + \mathbf{n} \quad (1)$$

where $\mathbf{y} = [y_1, \dots, y_{N_t}]^T$, $\mathbf{u} = [u_1, \dots, u_{N_t}]^T$, and $\mathbf{n} = [n_1, \dots, n_{N_t}]^T$. The $N_t \times N_t$ matrix \mathbf{H} has complex element $h_{i,j}$ of MIMO channel with $\mathbf{E}\{|h_{i,j}|^2\} = 1$. We assume the power constraint $E\{|\mathbf{u}|^2\} = 1$ and σ^2 is the signal to noise ratio (SNR) at the receiving antenna named as SNR per stream. Therefore the noise variance matrix $E\{\mathbf{n}\mathbf{n}^H\}$ is represented as $\frac{1}{N_t\sigma^2}\mathbf{I}_{N_t}$ and \mathbf{I}_{N_t} is $N_t \times N_t$ identity matrix.

The linear RCI MU-MIMO structure is shown in Fig. 1 (a). Suppose that BS has the perfect CSI \mathbf{H} , the RCI spatial filter is represented as

$$\mathbf{W} = \mathbf{H}^H(\mathbf{H}\mathbf{H}^H + \frac{\alpha}{\sigma^2}\mathbf{I}_{N_t})^{-1}. \quad (2)$$

The transmitted data \mathbf{x} is processed as

$$\mathbf{s} = \mathbf{W}\mathbf{x} = \mathbf{H}^H(\mathbf{H}\mathbf{H}^H + \frac{\alpha}{\sigma^2}\mathbf{I}_{N_t})^{-1}\mathbf{x}. \quad (3)$$

After normalized the symbol \mathbf{s} as

$$\mathbf{u} = \sqrt{\frac{1}{\gamma}}\mathbf{s} \quad (4)$$

with $\gamma = \|\mathbf{s}\|^2 = \|\mathbf{W}\mathbf{x}\|^2$, the transmit symbol \mathbf{u} is transmitted over MU-MIMO channel \mathbf{H} to all users. Therefore, the received symbol \mathbf{y} is represented as

$$\mathbf{y} = \sqrt{\frac{1}{\gamma}}\mathbf{H}\mathbf{H}^H(\mathbf{H}\mathbf{H}^H + \frac{\alpha}{\sigma^2}\mathbf{I}_{N_t})^{-1}\mathbf{x} + \mathbf{n}. \quad (5)$$

After multiplied by $\sqrt{\gamma}$, the received symbol $\sqrt{\gamma}\mathbf{y}$ is demodulated as $\hat{\mathbf{x}}$. The regularization parameter α is used to minimize the total MSE between the transmitted symbols \mathbf{x} and received symbols $\hat{\mathbf{x}}$.

However, if \mathbf{H} is a high correlated channel matrix, the normalized parameter γ becomes large therefore the SNR becomes small. To mitigate its effect, vector perturbation (VP) perturbs the transmitted symbol \mathbf{x} with a perturbation vector to reduce the normalized parameter γ [2]. We use Fig. 1(b) to show its structure. Let us set $\hat{\mathbf{x}} = \mathbf{x} + \tau\boldsymbol{\ell}$ where τ is chosen as $2(|c|_{max} + d_{min}/2)$. Here $|c|_{max}$ is the absolute value of constellation point with the largest amplitude and d_{min} is the

spacing between two adjacent constellation points. $\boldsymbol{\ell}$ is an N_t -dimensional complex perturbation vector $a + ib$, where a and b are integers. The normalized parameter γ is computed as

$$\gamma = \|\mathbf{H}^H(\mathbf{H}\mathbf{H}^H + \frac{\alpha}{\sigma^2}\mathbf{I}_{N_t})^{-1}(\mathbf{x} + \tau\boldsymbol{\ell})\|^2 = \|\mathbf{W}(\mathbf{x} + \tau\boldsymbol{\ell})\|^2. \quad (6)$$

The core design of VP is to find the optimum choice $\boldsymbol{\ell}_0$ which minimizes the γ to γ_0 , that is

$$\boldsymbol{\ell}_0 = \arg \min_{\boldsymbol{\ell}'} \left\| \mathbf{H}^H(\mathbf{H}\mathbf{H}^H + \frac{\alpha}{\sigma^2}\mathbf{I}_{N_t})^{-1}(\mathbf{x} + \tau\boldsymbol{\ell}') \right\|^2 \quad (7)$$

with

$$\gamma_0 = \left\| \mathbf{H}^H(\mathbf{H}\mathbf{H}^H + \frac{\alpha}{\sigma^2}\mathbf{I}_{N_t})^{-1}(\mathbf{x} + \tau\boldsymbol{\ell}_0) \right\|^2. \quad (8)$$

If BS uses the precoding matrix \mathbf{W} with regularization parameter α to pre-cancel the interference among streams, the transmitted signal after perturbation vector search as Eq. (4) is

$$\mathbf{u} = \frac{1}{\sqrt{\gamma_0}}\mathbf{H}^H(\mathbf{H}\mathbf{H}^H + \frac{\alpha}{\sigma^2}\mathbf{I}_{N_t})^{-1}(\mathbf{x} + \tau\boldsymbol{\ell}_0). \quad (9)$$

In such case, the purpose of RCI-VP is, in essence, the optimization to get the smallest γ to improve SNR at the receiver side.

The symbol \mathbf{u} is transmitted over MU-MIMO channel \mathbf{H} to all users. After multiplied by $\sqrt{\gamma_0}$, the received symbol can be represented as

$$\hat{\mathbf{y}} = \mathbf{H}\mathbf{H}^H(\mathbf{H}\mathbf{H}^H + \frac{\alpha}{\sigma^2}\mathbf{I}_{N_t})^{-1}(\mathbf{x} + \tau\boldsymbol{\ell}_0) + \sqrt{\gamma_0}\mathbf{n}. \quad (10)$$

To remove the effect of the integer multiple of τ for i th stream, the receiver utilizes the modulo function as

$$\hat{x}_i = \text{mod}_{\tau}(\hat{y}_i) = \hat{y}_i - \left\lfloor \frac{\hat{y}_i + \tau/2}{\tau} \right\rfloor \tau \quad (11)$$

where the function $\lfloor \cdot \rfloor$ gives the largest integer less than or equal to its argument. With the modulo function, the receiver can demodulate its own data.

B. QR-decomposition M-algorithm encoder

The perturbation vector search of Eq. (7) is a $2N_t$ -dimensional integer-lattice least-squares problem which can be resolved using the sphere decoder [11]. However, the computational complexity (CC) of the sphere decoder is large and limits the application of VP. An efficient sphere decoder algorithm can be realized using the QR-decomposition M-algorithm encoder (QRDM-E) [10] which can balance the trade-off between the CC and the diversity order of VP.

QRDM-E limits the integer value a and b of $\boldsymbol{\ell}$ selected from the symmetric integer set \mathcal{A} as $\mathcal{A} = \{-T, -T + 1, \dots, -1, 0, 1, \dots, T - 1, T\}$, which reduces the search complexity with a smaller value T . On the other hand, QRDM-E factorizes the matrix \mathbf{W} of Eq. (7) into the product of a unitary

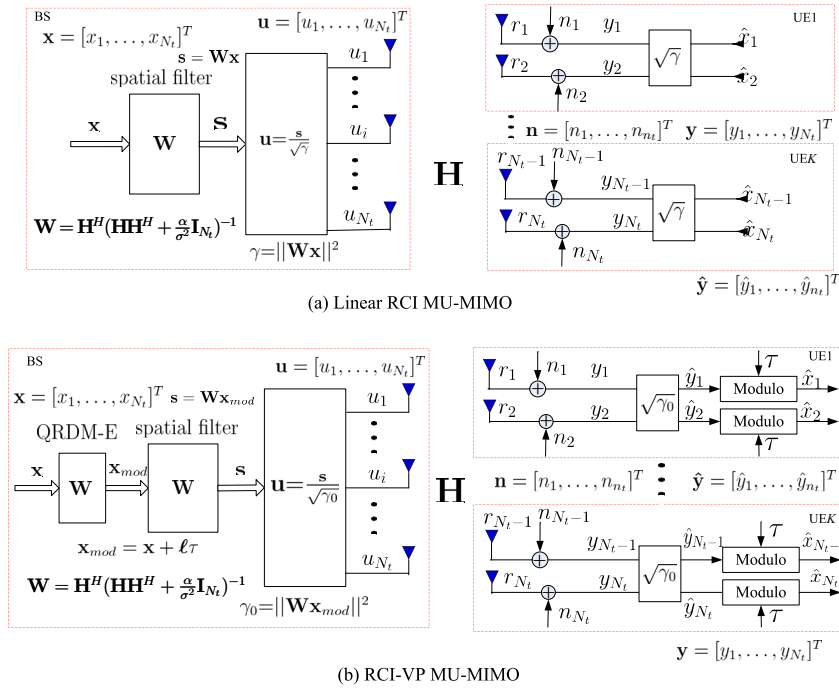


Fig. 1. The structures of linear MMSE MU-MIMO and nonlinear RCI-VP MU-MIMO.

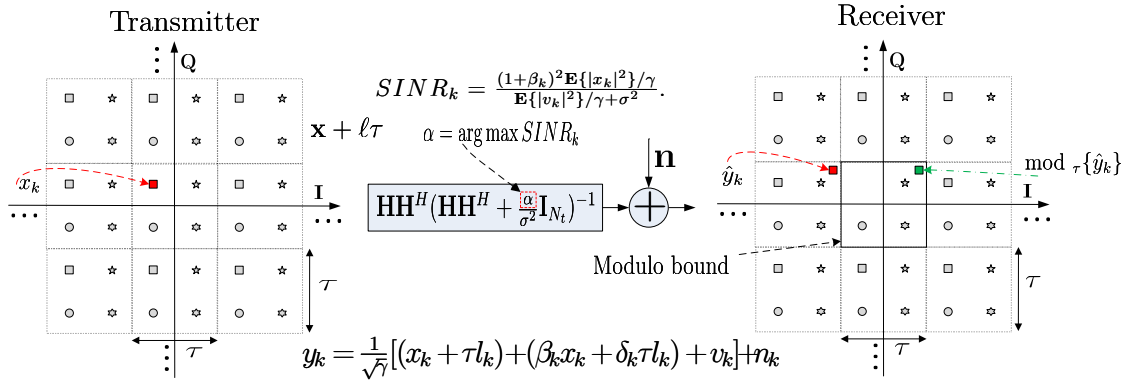


Fig. 2. The symbol mismatch caused by modulo operator on received symbol with optimization of SINR for each stream.

matrix \mathbf{Q} and an upper triangular matrix \mathbf{R} . Thus, the search problem in Eq. (7) is simplified to

$$\ell_0 = \arg \min_{\ell' \in \mathcal{A}^{N_t}} \|\mathbf{QR}(\mathbf{x} + \tau \ell')\|^2 = \arg \min_{\ell' \in \mathcal{A}^{N_t}} \|\mathbf{R}(\mathbf{x} + \tau \ell')\|^2. \quad (12)$$

The search process of Eq. (12) is realized using an M-algorithm for each stream in a successive way. The best M branches that have the least accumulative metrics to find $\ell_0(k+1)\tau$ for the $(k+1)$ th stream are retained for the next stage to find $\ell_0(k)\tau$ for the k th stream. We omit the illustration for QRDM-E process and reader can find the clear explanation in [10].

III. THE PROPOSAL OF RCI-VP ALGORITHM WITH DUAL REGULARIZATION PARAMETERS

A. Regularization parameter α for optimization of SINR for each stream

The regularization parameter α can be optimized to balance the inter-stream interference and noise power to maximize the SINR. The optimal value α is generally obtained by a numerical method as pointed out in References [2], [5]. It is also shown in [2] and [5] that the optimal α for maximizing SINR is generally smaller than N_t . We briefly review this

process. To get the optimal α , the received signal is written as

$$\begin{aligned} \mathbf{y} &= \frac{1}{\sqrt{\gamma_0}} \frac{\mathbf{H}\mathbf{H}^H}{\mathbf{H}\mathbf{H}^H + \frac{\alpha}{\sigma^2} \mathbf{I}_{N_t}} (\mathbf{x} + \tau \boldsymbol{\ell}_0) + \mathbf{n} \\ &= \frac{1}{\sqrt{\gamma_0}} \left[\mathbf{I}_{N_t} (\mathbf{x} + \tau \boldsymbol{\ell}_0) + \mathcal{F}(\mathbf{x} + \tau \boldsymbol{\ell}_0) \right] + \mathbf{n}, \end{aligned} \quad (13)$$

where $\mathcal{F} = \{(\mathbf{I}_{N_t} + \frac{\alpha}{\sigma^2} (\mathbf{H}\mathbf{H}^H)^{-1})^{-1} - \mathbf{I}_{N_t}\}$. The received signal for the k th stream is

$$y_k = \frac{1}{\sqrt{\gamma_0}} [(x_k + \tau \ell_0(k)) + \langle \mathcal{F}(\mathbf{x} + \tau \boldsymbol{\ell}_0) \rangle_k] + n_k \quad (14)$$

where the notation $\langle \mathbf{C} \rangle_k$ represents the k th row of matrix \mathbf{C} . It is clear that $\langle \mathcal{F}(\mathbf{x} + \tau \boldsymbol{\ell}_0) \rangle_k$ is potentially correlated with x_k and $\ell_0(k)$. This correlation can be model as

$$y_k = \frac{1}{\sqrt{\gamma_0}} [(x_k + \tau \ell_0(k)) + (\beta_k x_k + \delta_k \tau \ell_0(k)) + v_k] + n_k \quad (15)$$

where v_k is co-channel interference (CCI) and uncorrelated with x_k and $\ell_0(k)$. Here β_k and δ_k represent the correlation coefficients of the term $\langle \mathcal{F}(\mathbf{x} + \tau \boldsymbol{\ell}_0) \rangle_k$ with x_k and $\ell_0(k)$. As shown in Reference [5], the SINR of the k th stream $SINR_k$ is

$$SINR_k = \frac{(1 + \beta_k)^2 \mathbf{E}\{|x_k|^2\} / \gamma}{\mathbf{E}\{|v_k|^2\} / \gamma_0 + (N_t \sigma^2)^{-1}}. \quad (16)$$

The regularization parameter α controls the value of γ_0 , the correlation β_k and the variance of v_k . Increasing α generally decreases γ_0 , then potentially increasing the $SINR_k$, but increases the variance of v_k , then potentially decreasing the $SINR_k$. Therefore the overall impact on the performance of RCI-VP is difficult to determine analytically. Therefore, it is generally obtained by a numerical method.

However, the optimization of maximizing SINR does not consider the effect of modulo operator which will increase the symbol error caused by the modulo process. Let us use Fig. 2 to show the process of symbol error on transmitting symbol x_k . After optimization of maximizing SINR, the RCI-VP utilizes the regularization parameter α to the transmit data. The receiver receives the symbol \hat{y}_k which statistically has the maximum SINR. As shown in Fig. 2, the received symbol \hat{y}_k is out of modulo bound and causes symbol error after the modulo operation.

B. Regularization parameter α for optimization of total MSE between the transmitted perturbed vector and received perturbed vector

To minimize the symbol error caused by modulo operator, α is to be optimized so as to minimize the total MSE between the transmitted perturbed vector $(\mathbf{x} + \boldsymbol{\ell}_0 \tau)$ and its received perturbed vector $\hat{\mathbf{x}}_r$ at the receiver side. After perturbation vector search, the transmit data \mathbf{x} is perturbed as $\hat{\mathbf{x}} = \mathbf{x} + \tau \boldsymbol{\ell}_0$. Here $\tau \boldsymbol{\ell}_0$ can obtain the smallest γ_0 as shown in Eq. (8). To

realize such optimization, we consider a precoding matrix \mathbf{P} . The received symbol $\hat{\mathbf{x}}$ is represented as

$$\hat{\mathbf{x}}_r = \frac{1}{\sqrt{\gamma_P}} \mathbf{H} \mathbf{P} \hat{\mathbf{x}} + \mathbf{n} \quad (17)$$

where γ_P equals $\mathbf{E}\{\|\mathbf{P}\hat{\mathbf{x}}\|^2\}$.

The optimization can be represented as

$$\begin{aligned} \{\mathbf{P}_{opt}, \gamma_{opt}\} &= \arg \min_{\mathbf{P}, \gamma_P} \mathbf{E}\{\|\hat{\mathbf{x}}_r - \hat{\mathbf{x}}\|^2\} \\ S.t. : \quad \mathbf{E}\{\|\mathbf{P}\hat{\mathbf{x}}\|^2\} &= \gamma_P \end{aligned} \quad (18)$$

The analytic solution for this optimization is represented as

$$\begin{aligned} \mathbf{P}_{opt} &= \mathbf{H}^H (\mathbf{H}\mathbf{H} + \xi \mathbf{I}_{N_t})^{-1} \\ \gamma_{opt} &= \|\mathbf{P}_{opt} \hat{\mathbf{x}}\|^2 \end{aligned} \quad (19)$$

where the regularization parameter $\xi = \text{Tr}\{\frac{1}{\sigma^2} \mathbf{I}_{N_t}\} = \frac{N_t}{\sigma^2}$ [12]. The solution also shows that if the previous optimal regularization parameter α_1 for maximizing the SINR obtained by numerical method is identical to the regularization parameter $\xi \sigma^2$, the total MSE between the $\hat{\mathbf{x}}$ and $\hat{\mathbf{x}}_r$ is also minimized. However, as shown in References [2] and [5], the optimal α for maximizing the SINR is generally smaller than N_t and cannot realize both optimization targets.

C. Proposed method with dual regularization parameters

The proposed method, which is combined by both optimization targets of the regularization parameters, is realized as following steps.

- (1) We use numerical method to find an efficient regularization parameter α_1 which can achieve best BER performance for each different modulation based on simulated results.
- (2) For perturbation vector search, the optimum choice $\boldsymbol{\ell}$ which minimizes γ is searched using precoding matrix with regularization parameter α_1 as

$$\boldsymbol{\ell} = \arg \min_{\boldsymbol{\ell}' \in \mathcal{A}^{N_t}} \left\| \frac{\mathbf{H}^H (\mathbf{x} + \tau \boldsymbol{\ell}')}{\mathbf{H}\mathbf{H}^H + \frac{\alpha_1}{\sigma^2} \mathbf{I}_{N_t}} \right\|^2. \quad (20)$$

- (3) The precoding matrix \mathbf{W} is set as $\mathbf{W} = \mathbf{P}_{opt} = \mathbf{H}^H (\mathbf{H}\mathbf{H}^H + \frac{\alpha_2}{\sigma^2} \mathbf{I}_{N_t})^{-1}$ with the minimum-mean square error (MMSE) weight to realize the total MSE optimization. Therefore, after obtaining the optimum choice $\tau \boldsymbol{\ell}$, BS sets the transmit symbol as

$$\mathbf{u} = \frac{1}{\sqrt{\gamma'}} \mathbf{W} (\mathbf{x} + \tau \boldsymbol{\ell}) = \mathbf{H}^H (\mathbf{H}\mathbf{H}^H + \frac{\alpha_2}{\sigma^2} \mathbf{I}_{N_t})^{-1} (\mathbf{x} + \tau \boldsymbol{\ell}) \quad (21)$$

where $\gamma' = \|(\mathbf{H}^H (\mathbf{H}\mathbf{H}^H + \frac{\alpha_2}{\sigma^2} \mathbf{I}_{N_t})^{-1}) (\mathbf{x} + \tau \boldsymbol{\ell})\|^2$.

IV. PERFORMANCE EVALUATION OF PROPOSED METHOD OVER THE FLAT-FADING AND CORRELATED FREQUENCY-SELECTIVE FADING MIMO CHANNEL

A. Finding α_1 by numerical method

We utilize a numerical method to find efficient value of α_1 . As shown in References [2] and [5], the optimal α_1 is usually smaller than N_t . We simulate the BER performance of VP

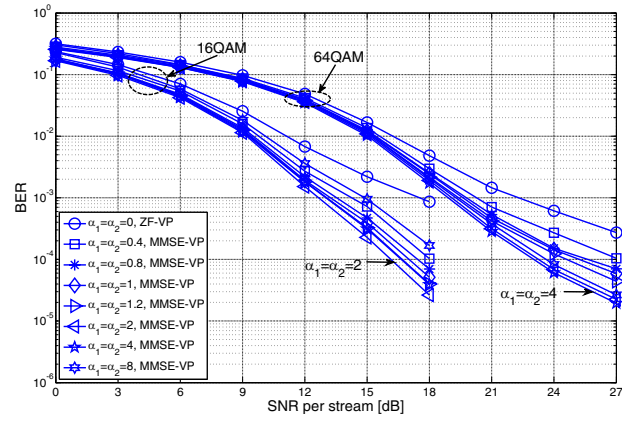
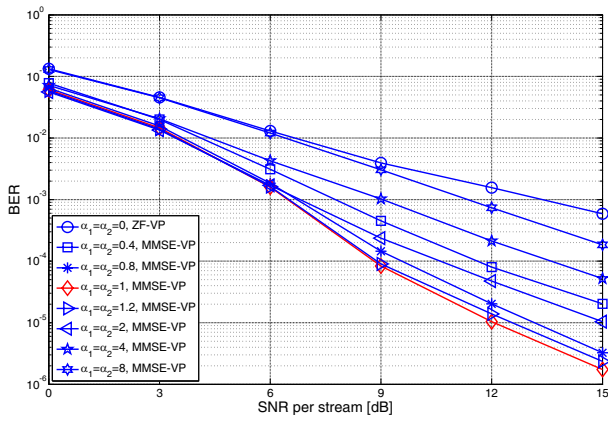


Fig. 3. The simulated BER performance of RCI-VP algorithm when $\alpha_1 = \alpha_2$ (left: QPSK modulation; right: 16QAM, 64QAM modulations)

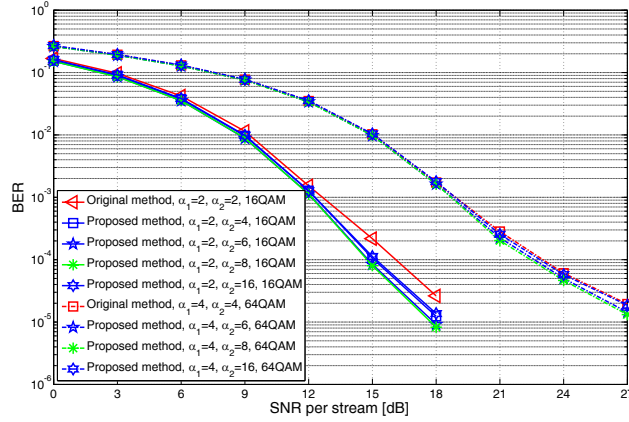
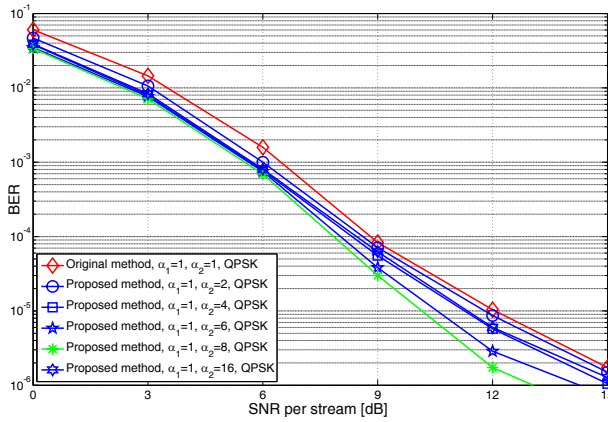


Fig. 4. The simulated BER performance RCI-VP algorithm with different value of α_2 (left: QPSK modulation; right: 16QAM, 64QAM modulations)

algorithm with different value of α_1 and α_2 over *i.i.d.* MIMO channel. We assume $N_t = 8$ and $(T, M) = (3, 7)$ for QRDM-E algorithm. The simulated BER results are shown in Fig. 3 for QPSK, 16QAM and 64QAM modulations. According to the simulated results, $\alpha_1 = 1, 2, 4$ gives the best performance for QPSK, 16QAM and 64QAM over (8×8) *i.i.d.* channel, respectively.

B. BER performance evaluation of proposed method over flat-fading MIMO Channel

Fig. 4 shows the simulated results of the proposed method over *i.i.d.* MIMO channel with different modulations. We also assume $N_t = 8$ and $(T, M) = (3, 7)$ for QRDM-E algorithm. To show the impact of α_2 , we choose different values to compare the BER performance. The simulated results show that the proposed method can improve the performance of RCI-VP for all modulations especially for QPSK modulation. The reason dues to that, for modulation with a large number of constellation points, the effect of modulo function has little impact on the interior constellation points than that of boundary constellation points even if the MSE of between the transmitted perturbed vector and received perturbed vector is slightly increased.

C. Spectrum efficiency (SE) evaluation of proposed method over flat and frequency-selective fading MIMO Channels

We compare the spectrum efficiency (SE) of the proposed method using dual regularization parameters with the original method using one regularization parameter based on SINR optimization. The simulation specifications are given in Table I. We use *i.i.d.* channel, one indoor correlated channel model (A1 LOS) and one suburban macro cell channel model (C1 NLOS) as shown in Table II to evaluate SE of the proposed method and the original method. We also assume that the transmitter and the receiver have the perfect knowledge of CSI.

We first compare the proposed method using dual regularization parameters with the original method using one regularization parameter over *i.i.d.* channel and the simulated results are given in Fig. 5. The values of α_1 and α_2 are set based on the previous simulated results. As shown in the figure, the proposed method can achieve better SE performance than that of original method especially for QPSK modulation.

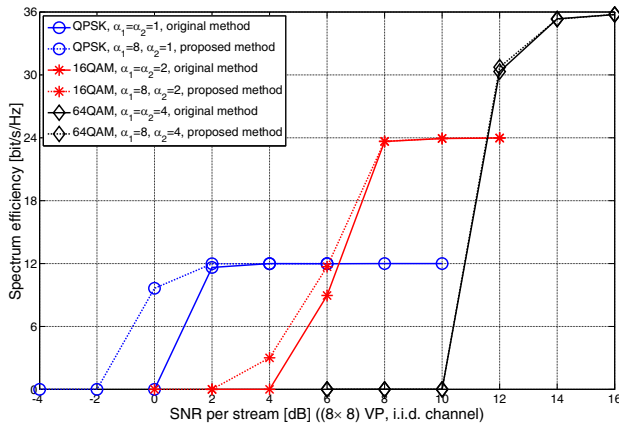
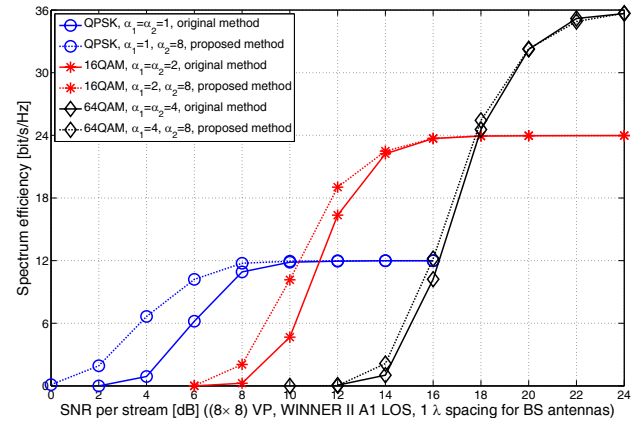
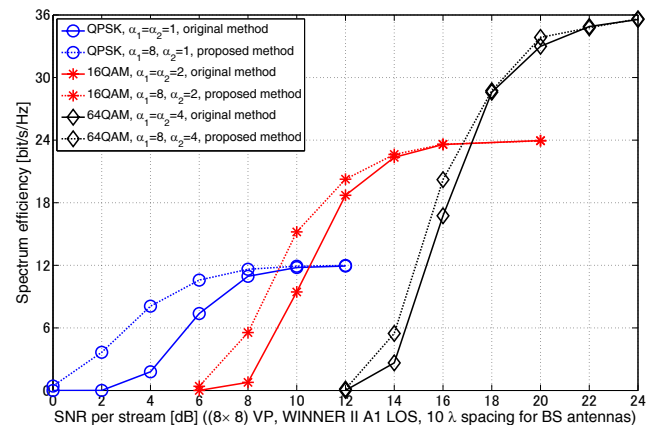
The simulated results over A1 LOS channel with 1λ and 10λ spacing for BS antennas are shown in Fig. 6 and Fig. 7. The values of α_1 and α_2 are also set based on the previous simulated results over *i.i.d.* MIMO channel. As shown in both figures, the simulated results confirm that using different

TABLE I. SIMULATION SPECIFICATIONS

Sampling rate	30.72 Msamples/s
FFT size	2048
Length of cyclic prefix	4.7 μ s
Number of subcarriers	1200
Number of antennas	8 (BS) 2 (UE)
Number of users (N)	4
Direction of UEs	-67.5, -22.5, 22.5 and 67.5 (Deg.)
Modulation scheme	QPSK, 16QAM, 64QAM
Channel coding	Turbo code
Coding rate	3/4
Frame size	3597 bits +3 parity bits (QPSK) 3597 bits +3 parity bits (16QAM) 5397 bits +3 parity bits (64QAM)
Interleaver	Random interleaver
Decoding algorithm	soft-output Viterbi algorithm
Number of decoding iterations	6
Array configuration	Equally spaced linear array
Antenna spacing	1 λ and 10 λ of DL carrier frequency (BS) 0.5 λ of DL carrier frequency (UE)
Carrier frequency	3.36 GHz (DL)
Spatial filtering	MMSE
Estimation of average received SNR	Perfect
Perturbated vector search	QRDM-E [10], (T, M) = (3, 7)

TABLE II. CHANNEL PARAMETERS FOR A1 LOS AND C1 NLOS [13]

Channel model	A1 LOS	C1 NLOS
Average delay spread [ns]	40	234
Average AoA/AoD [Deg.]	44/45	8/45
Average K-factor [dB]	5-6	-


 Fig. 5. The spectrum efficiency performance comparison of RCI-VP algorithm with and without dual regularization parameters over *i.i.d.* MIMO channel.

 Fig. 6. The spectrum efficiency performance comparison of RCI-VP algorithm with and without dual regularization parameters over A1 LOS MIMO channel (1 λ spacing for BS antennas).

 Fig. 7. The spectrum efficiency performance comparison of RCI-VP algorithm with and without dual regularization parameters over A1 LOS MIMO channel (10 λ spacing for BS antennas).

values of α_1 and α_2 can increase the SE of the RCI-VP system than that using the method based on the original SINR optimization especially for the modulation with a small number of constellation points such as QPSK modulation.

The simulated results over C1 NLOS channel with 1 λ and 10 λ spacing for the BS antennas are shown in Fig. 8 and Fig. 9. As shown in both figures, the simulated results confirm that using dual regularization parameters increases the SE of RCI-VP system than that using the method based on original SINR optimization especially for QPSK modulation. However, compared with Fig. 8, the SE improvement in Fig. 9 using dual regularization parameters is small because the channel is a low correlated one even if the BS antenna spacing is 1 λ .

Based on the simulated results over flat and frequency-selective fading channels, using dual regularization parameters for RCI-VP system can reduce the symbol error caused by a modulo operator compared with the system using one regularization parameter based on the criteria of SINR maximum. The proposed method will provide better SE improvement

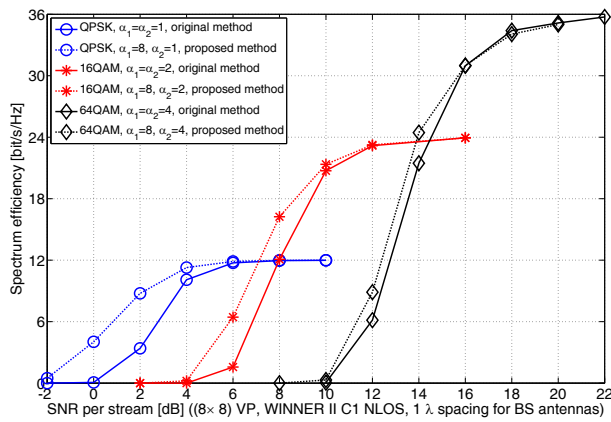


Fig. 8. The spectrum efficiency performance comparison of RCI-VP algorithm with and without dual regularization parameters over C1 NLOS MIMO channel (1 λ spacing for BS antennas).

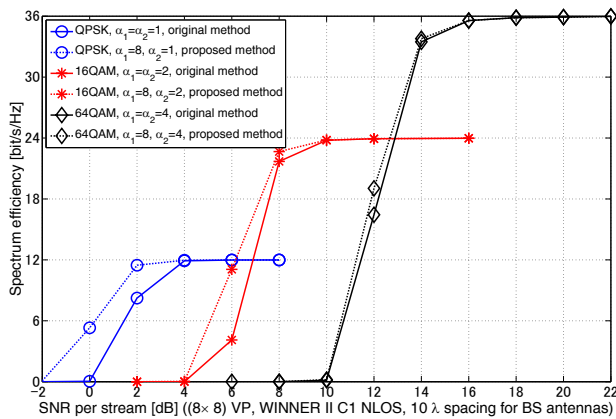


Fig. 9. The spectrum efficiency performance comparison of RCI-VP algorithm with and without dual regularization parameters over C1 NLOS MIMO channel (10 λ spacing for BS antennas).

especially over a low SNR range using the modulation with small number of constellation points.

V. CONCLUSIONS

We have proposed a method to reduce the symbol error caused by a modulo operator for RCI-VP using dual regularization parameters of RCI precoding matrix. The proposed method utilizes the RCI precoding matrix with regularization parameter α_1 which can maximize the SINR of each stream to find the optimal perturbation vector. For the RCI precoding matrix to pre-cancel the interference among the streams, the RCI-VP uses the RCI precoding matrix with regularization parameter α_2 which can minimize the total MSE between the transmitted perturbation vector and received perturbation vector. The simulated results confirm that the proposed method can improve the performance of RCI-VP especially for QPSK modulation over *i.i.d.* MIMO channel and frequency-selective fading MIMO channel.

ACKNOWLEDGMENT

The authors appreciate that Dr. Masayuki Ariyoshi has suggested many good advices and comments on this paper.

REFERENCES

- [1] D. Gesbert, M. Kountouris, R. Heath, C. B. Chae, and T. Salzer, "Shifting the MIMO paradigm," *IEEE Signal Processing Magazine*, vol. 24, no. 5, pp. 36–46, Sept. 2007.
- [2] B. M. Hochwald, C. B. Peel, and A. L. Swindlehurst, "A vector-perturbation technique for near-capacity multi-antenna multiuser communication-part II: perturbation," *IEEE Transactions on Communications*, vol. 53, no. 3, pp. 537–544, Mar. 2005.
- [3] U. Erez, and St. Brink., "A close-to-capacity dirty paper coding scheme," *IEEE Trans. on Information Theory*, vol.51, no.10, pp. 3417–3432, Oct. 2005.
- [4] C. B. Peel, B. M. Hochwald, and A. L. Swindlehurst, "A vector-perturbation technique for near-capacity multi-antenna multiuser communication-part I: channel inversion and regularization," *IEEE Transactions on Communications*, vol. 53, no. 1, pp. 195–202, Jan. 2005.
- [5] C. Yuen, B. M. Hochwald, "How to gain 1.5 dB in vector precoding," in Proc. *2006 IEEE Globecom*, Nov. 2006.
- [6] W. S. Chua, C. Yuen and F. Chin, "A continuous vector-perturbation for multi-antenna multi-user communication," in Proc. *2007 IEEE VTC-Spring*, pp. 1806-1810, Apr. 2007.
- [7] W. Yao, S. Shen and L. Hanzo, "Generalized MBER-based vector precoding design for multiuser transmission," *IEEE Transactions on Vehicular Technology*, vol. 60, no. 2, pp. 739–745, Feb. 2011.
- [8] F. Liu, L. Jiang and C. Chen, "Low complexity MMSE vector precoding using lattice reduction for MIMO systems," in Proc. *2007 IEEE ICC*, pp. 2598–2603, Jun. 2007.
- [9] C. Y. Kim, J. Chun, "Optimum vector perturbation minimizing total MSE in multiuser MIMO downlink," in Proc. *2006 IEEE ICC*, Jun. 2006.
- [10] M. Mohaisen, H. Bing, and K.H. Chang, "Fixed-complexity vector perturbation with block diagonalization for MU-MIMO systems," in Proc. *2009 IEEE 9th Malaysia International Conference on Communications (MICC 2009)*, pp. 238–243, 15-17 Dec. 2009.
- [11] B. Hassibi and H. Vikalo, "On sphere decoding algorithm. I. expected complexity," *IEEE Transactions on Signal Processing*, vol. 53, no. 8, pp. 2806–2818, Aug. 2005.
- [12] M. Joham, W. Utschick, and JA. Nossek, "Linear transmit processing in MIMO communications systems," *IEEE Transactions on signal Processing*, vol. 53, no. 8, pp. 2700–2712, Aug. 2005.
- [13] WINNER II D1.1.2, "WINNER II channel models," <http://www.ist-winner.org/deliverables.html>, Sep. 2007.



Yafei Hou received his B.S. degree in Electronic Engineering from Anhui University of Technology and Science, China, in 1999 and M.S. degree in Computer Science from Wuhan University, China, in 2002, respectively. He received the Ph.D. degrees from Fudan University, China and Kochi University of Technology (KUT), Japan, as an international student of cooperation between KUT and Fudan University in 2007. From August 2007 to September 2010, He was a post-doctoral research fellow at the Research Center for Information and Communication

Systems, Ryukoku University, Japan. Since Oct. 2010, He has been a research scientist at ATR Wave Engineering Laboratories, Japan. His main areas of interest are communication systems, wireless networks, ad-hoc networks and signal processing. He is the member of IEICE and IEEE.



Satoshi Tsukamoto received his B. E. degree in electronics engineering from Tokyo Denki University (TDU) in 1991 and BLA degree from the Open University of Japan (OUJ) in 2005. From 1997 to 2005, he worked in Cybernetics Technology Co., Ltd., Tokyo, Japan, and involved in many projects for developments of experimental systems and system prototypes for wireless communications. Since November 2005, He has been a senior researcher at Wave Engineering Laboratories of ATR, Japan. He is a committee member of commission C, Japan

National Committee of URSI, and is also a member of IEICE and IEEE.



Kazuto Yano received a B.E. degree in electrical and electronic engineering, M.S. and Ph.D. degrees in communications and computer engineering from Kyoto University in 2000, 2002, and 2005, respectively. He was a research fellow of the Japan Society for the Promotion Science (JSPS) from 2004 to 2006. In 2006, he joined the Advanced Telecommunications Research Institute International (ATR). Currently, he is a senior research scientist of the Wave Engineering Laboratories, ATR. His research interests include space-time signal processing for

interference suppression, MIMO transmission, and PHY/MAC cross-layer design of cognitive radio for ISM bands. He received the IEEE VTS Japan 2001 Researcher's Encouragement Award, the IEICE Young Researcher's Award in 2007, the Ericsson Young Scientist Award 2007 and the IEICE 2007 Active Research Award in Radio Communication Systems. He also received 2010 Young Investigator Award in Software Radio from IEICE Technical Committee on Software Radio. He is a member of IEICE and IEEE.



Masahiro Uno received the B.E. and M.E. degrees in electronics engineering from Sophia University, Tokyo, Japan, in 1988 and 1990. He joined Sony Corporation, Tokyo, Japan, in 1990, where he was involved in the research and development of wireless communication systems. From Oct. 2010 to Mar. 2013, he has been with Advanced Telecommunication Research Institute, International (ATR) in Kyoto, Japan as the header of Wireless Communication Systems Department, Wave Engineering Laboratories. From Apr. 2013, he is in Device Solution Business

Group, Sony Corporation. His research interests are digital and analog signal processing technologies for wireless communication systems. He is a member of IEICE and IEEE.



Kiyoshi Kobayashi received the B.E., M.E. and Ph.D. degrees from Tokyo University of Science, Japan, in 1987, 1989 and 2004, respectively. He joined NTT Radio Communication Systems Laboratories in 1989. Currently, he is the director of ATR Wave Engineering Laboratories at Advanced Telecommunications Research Institute International, where he is engaged in research on advanced technologies for wireless communications. He is a member of IEEE, AIAA and IEICE.

Volume 2 Issue 6, Nov 2013, ISSN: 2288-0003

**ICACT-TACT
JOURNAL**



**Global IT
Research Institute**

1713 Obelisk, 216 Seohyunno, Bundang-gu, Sungnam Kyunggi-do, Republic of Korea 463-824
Business Licence Number : 220-82-07506, Contact: secretariat@icact.org Tel: +82-70-4146-4991